

## ABSTRACT

Title of dissertation: DESIGN, DEVELOPMENT, AND  
EVALUATION OF A DISCRETELY  
ACTUATED STEERABLE CANNULA

Elif Ayvali, Doctor of Philosophy, 2014

Dissertation directed by: Professor Jaydev P. Desai  
Department of Mechanical Engineering

Needle-based procedures require the guidance of the needle to a target region to deliver therapy or to remove tissue samples for diagnosis. During needle insertion, needle deflection occurs due to needle-tissue interaction which deviates the needle from its insertion direction. Manipulating the needle at the base provides limited control over the needle trajectory after the insertion. Furthermore, some sites are inaccessible using straight-line trajectories due to delicate structures that need to be avoided. The goal of this research is to develop a discretely actuated steerable cannula to enable active trajectory corrections and achieve accurate targeting in needle-based procedures.

The cannula is composed of straight segments connected by shape memory alloy (SMA) actuators and has multiple degrees-of-freedom. To control the motion of the cannula two approaches have been explored. One approach is to measure the cannula configuration directly from the imaging modality and to use this information as a feedback to control the joint motion. The second approach is a model-based

controller where the strain of the SMA actuator is controlled by controlling the temperature of the SMA actuator. The constitutive model relates the stress, strain and the temperature of the SMA actuator. The uniaxial constitutive model of the SMA that describes the tensile behavior was extended to one-dimensional pure-bending case to model the phase transformation of the arc-shaped SMA wire. An experimental characterization procedure was devised to obtain the parameters of the SMA that are used in the constitutive model. Experimental results demonstrate that temperature feedback can be effectively used to control the strain of the SMA actuator and image feedback can be reliably used to control the joint motion.

Using tools from differential geometry and the configuration control approach, motion planning algorithms were developed to create pre-operative plans that steer the cannula to a desired surgical site (nodule or suspicious tissue). Ultrasound-based tracking algorithms were developed to automate the needle insertion procedure using 2D ultrasound guidance. The effectiveness of the proposed in-plane and out-of-plane tracking methods were demonstrated through experiments inside tissue phantom made of gelatin and *ex-vivo* experiments. An optical coherence tomography probe was integrated into the cannula and *in-situ* microscale imaging was performed. The results demonstrate the use of the cannula as a delivery mechanism for diagnostic applications.

The tools that were developed in this dissertation form the foundations of developing a complete steerable-cannula system. It is anticipated that the cannula could be used as a delivery mechanism in image-guided needle-based interventions to introduce therapeutic and diagnostic tools to a target region.

DESIGN, DEVELOPMENT AND EVALUATION OF A  
DISCRETELY ACTUATED STEERABLE CANNULA

by

Elif Ayvali

Dissertation submitted to the Faculty of the Graduate School of the  
University of Maryland, College Park in partial fulfillment  
of the requirements for the degree of  
Doctor of Philosophy  
2014

Advisory Committee:

Professor Jaydev P. Desai, Chair/Advisor

Professor Inderjit Chopra, Dean's Representative

Professor Amr Baz

Professor Nikhil Chopra

Professor Jin-Oh Hahn

© Copyright by  
Elif Ayvali  
2014

1. Portions reprinted, with permission, from: Elif Ayvali, Mingyen Ho, and Jaydev P. Desai, “A Novel Discretely Actuated Steerable Probe for Percutaneous Procedures”, In *12th International Symposium on Experimental Robotics (ISER 2010)*, New Delhi, India, December 18-21, 2010.
2. Portions reprinted, with permission, from: Elif Ayvali, Chia-Pin Liang, Mingyen Ho, Yu Chen, and Jaydev P. Desai, “Towards a discretely actuated steerable cannula for diagnostic and therapeutic procedures”, *The International Journal of Robotics Research*, April 2012 vol. 31 no. 5588-603.
3. Portions reprinted, with permission, from: Elif Ayvali and Jaydev P. Desai, “Towards a discretely actuated steerable cannula”, In *IEEE International Conference on Robotics and Automation (ICRA 2012)*, Saint Paul, MN, May 14-18, 2012.
4. Portions reprinted, with permission, from: Elif Ayvali and Jaydev P. Desai, “Motion planning for the discretely actuated steerable cannula”, In *IEEE International Conference on Biomedical Robotics and Biomechatronics (BIO ROB 2012)*, Rome, Italy, June 24-27, 2012.
5. Portions reprinted, with permission, from: Elif Ayvali and Jaydev P. Desai, “PWM-Based Temperature Tracking For Feedback Control Of A SMA Actuator”, *Journal of Intelligent Material Systems and Structures*, April 2014 vol. 25 no. 6 720-730, 2014.
6. Portions reprinted, with permission, from: Elif Ayvali and Jaydev P. Desai, “Accurate in-plane and out-of-plane ultrasound-based tracking of the discretely actuated steerable cannula”, *IEEE International Conference on Robotics and Automation (ICRA 2014)*, Hong Kong, China, May 31-June 7, 2014.
7. Portions reprinted, with permission, from: Elif Ayvali and Jaydev P. Desai, “Pulse-width modulation-based vision feedback control method for the discretely actuated steerable cannula”, *ASME Dynamic Systems and Control Conference (DSCC 2014)*(Accepted for publication).



## Acknowledgments

I would like to express my gratitude to everyone who supported me throughout my Ph.D. and made this dissertation possible. First and foremost, I would like to thank my advisor, Dr. Jaydev P. Desai, for giving me the opportunity to work in the Robotics, Automation, and Medical Systems (RAMS) Laboratory. His guidance, insights and constant feedback have been invaluable for my Ph.D research. Dr. Desai has always been available and supportive, for that I am deeply grateful. He has been a mentor for my career goals and has been a source of encouragement and motivation. I am also thankful to him and his wife, Anisha, for the occasional dinner parties and for making us feel welcomed.

Next, I would like to thank my committee members, Dr. Inderjit Chopra, Dr. Amr Baz, Dr. Nikhil Chopra, Dr. Teng Li and Dr. Jin-Oh Hahn, for agreeing to serve on my dissertation committee and taking the time to review my dissertation. They provided valuable suggestions which have been both constructive and insightful. I would also like to thank our collaborators, Dr. Yu Chen and Chia-Pin Liang, from the Biophotonics Lab at Fischell Department of Bioengineering. Dr. Yu Chen has spared time to help us with the optical coherence tomography experiments and gave valuable suggestions. I would also like to acknowledge the financial support from the National Institutes of Health (NIH), National Science Foundation (NSF) and 2011 UMCP-UMB seed grant for the research presented herein.

My colleagues at the RAMS Lab have enriched my graduate school experience. I would like to thank Kevin Lister for making my initial time in the laboratory very

comfortable and joyful. My discussions and brainstorming with Mingyen Ho on shape memory alloys have been comforting since working with shape memory alloys can sometimes be frustrating and maddening. In my first year, Yang Bo and U-Xuan Tan assisted me when I had problems with hardware or programming. Late night conversations in the lab with Rajarshi Roy, who is a night owl like me, have always been a pleasure. I especially like to thank Hardik Pandya and Wenxue Zhao whom I wish had joined the lab earlier. Their humor and support helped me to see lighter side of things when things got overwhelming. Many thanks to my fellow labmates Chad Kessens, Zhan Gao, Shing Shin Cheng, Yeongjin Kim, Jun Sheng, Hyuntae Kim and Carolyn Adkins for making my time at the RAMS Lab enjoyable.

I am grateful for the assistance of the staff at the Department of Mechanical Engineering. Mr. Amarildo Damata kept me on track during my graduate studies. Special thanks to Ms. Penny Komsat for processing the purchase requests quickly, Mr. Melvin Fields and Mr. Daniel Wysling for their prompt responses in software and hardware related issues, Mr. Steve Wicker and Ms. Lita Brown for helping with payroll, benefits, tax return and travel reimbursement. Finally, I would like to thank Howard Grossenbacher for his assistance in machining most of the prototypes.

I owe my deepest gratitude to my parents Emine Ayvali and Yuksel Ayvali. Thank you for sharing my dreams, being my rock when I need the most and supporting me through every decision I make.

To my beloved parents, this dissertation is dedicated.

# Table of Contents

List of Figures	vii
List of Abbreviations	xii
1 INTRODUCTION	1
1.1 Motivation . . . . .	1
1.2 Related Work . . . . .	5
1.2.1 Robot-assisted Needle Insertion . . . . .	5
1.2.2 Modeling Needle Tissue Interaction . . . . .	6
1.2.3 Tissue Manipulation . . . . .	8
1.2.4 Steerable Needle Design . . . . .	8
1.3 Discretely Actuated Steerable Cannula . . . . .	11
1.4 Dissertation Overview . . . . .	13
1.5 Dissertation Contributions . . . . .	14
2 SHAPE MEMORY ALLOYS	16
2.1 Fundamentals of SMA . . . . .	16
2.2 Annealing of Arc-shaped SMA . . . . .	21
2.3 Constitutive Model of SMA . . . . .	25
2.4 Characterization of Arc-shaped SMA Actuator . . . . .	28
2.4.1 Experimental Setup . . . . .	30
2.4.2 Characterization of Annealed Flexinol <sup>®</sup> . . . . .	32
2.4.2.1 Finding Transformation Temperatures . . . . .	32
2.4.2.2 Finding Stress Influence Coefficient . . . . .	35
2.4.2.3 Testing Under Variable Loading . . . . .	36
2.4.2.4 Finding the Relationship between Bending Angle and Strain . . . . .	37
2.4.3 Characterization of Drawn Nitinol . . . . .	38
2.4.3.1 Transformation Temperatures . . . . .	40
2.4.3.2 SMA Parameters Related to Stress . . . . .	41
2.4.3.3 Geometric Relations . . . . .	44
2.5 Summary and Discussions . . . . .	45

3	PWM-BASED CONTROL OF SMA	50
3.1	Motivation and Related Work . . . . .	50
3.2	Implementation of PWM-based Controllers . . . . .	53
3.3	PWM-based Nonlinear PID (NPID) Controller . . . . .	54
3.3.1	Thermal Modeling . . . . .	56
3.3.2	Implementation Of PWM-based NPID Controller . . . . .	61
3.4	Summary and Discussions . . . . .	65
4	DISCRETELY ACTUATED STEERABLE CANNULA	68
4.1	Prototype I: Steerable Probe with SMA Actuators . . . . .	68
4.1.1	Design of Prototype I . . . . .	69
4.1.2	Evaluation of Prototype I . . . . .	70
4.2	Prototype II: Integration of Imaging Window . . . . .	73
4.2.1	Design of Prototype II . . . . .	74
4.2.2	PWM-based Image Feedback Controller . . . . .	74
4.2.3	Testing of the PWM-based Image Feedback Inside Gelatin . . . . .	77
4.2.4	Strain-Temperature Relationship . . . . .	78
4.2.5	Testing of Maximum Force . . . . .	79
4.2.6	Application in Diagnosis . . . . .	80
4.2.6.1	Optical Coherence Tomography Fundamentals . . . . .	80
4.2.6.2	Optical Coherence Tomography Imaging Experiments . . . . .	82
4.2.7	Discussions on Prototype I and II . . . . .	87
4.3	Prototype III: Antagonistic SMA Actuators . . . . .	88
4.3.1	Design of Prototype III . . . . .	88
4.3.2	Strain-Temperature Relationship . . . . .	90
4.3.3	Discussions on Prototype III . . . . .	92
4.4	Prototype IV: Nonmetallic Segments . . . . .	92
4.4.1	Pulse-width Modulation-Based Motion Control . . . . .	94
4.5	Prototype V: A Compact Design . . . . .	96
4.6	Summary and Discussions . . . . .	98
5	MOTION PLANNING OF DISCRETELY ACTUATED STEERABLE CANNULA	101
5.1	Trajectory Planning Using Geodesics . . . . .	102
5.2	Configuration Control . . . . .	110
5.2.1	Singularity Avoidance and Obstacle Avoidance . . . . .	113
5.2.2	Joint Limit Avoidance . . . . .	115
5.2.3	Moving Obstacles . . . . .	122
5.3	Summary and Discussions . . . . .	124
6	ULTRASOUND-BASED TRACKING OF DISCRETELY ACTUATED STEERABLE CANNULA	127
6.1	Related Work on Ultrasound Imaging . . . . .	127
6.2	Experimental Setup . . . . .	132
6.3	Lucas-Kanade Optical Flow For In-plane Tracking . . . . .	134

6.3.1	Implementation of In-plane Tracking Algorithm . . . . .	139
6.4	Circular Hough Transform for Tip Detection . . . . .	141
6.5	Experiments and Results . . . . .	142
6.5.1	Obtaining Ultrasound Console Specific Parameters . . . . .	142
6.5.2	In-plane Tracking of the Cannula . . . . .	144
6.5.3	Out-of-plane Detection of the Cannula Tip . . . . .	150
6.6	Summary and Discussions . . . . .	154
7	CONCLUSIONS AND FUTURE WORK . . . . .	156
7.1	Conclusions . . . . .	156
7.2	Future Work . . . . .	160
	Bibliography . . . . .	162

## List of Figures

1.1	This figure demonstrates the anticipated use of the discretely actuated steerable cannula as a delivery tool for therapeutic and diagnostic applications such as a)biopsy, b)RFA, and c)OCT imaging. The final designs or the incorporated tools can be different. . . . .	12
2.1	One-way shape memory effect . . . . .	19
2.2	Stress-strain behavior in the one-way shape memory effect . . . . .	20
2.3	Transformation temperatures of the SMA under no stress . . . . .	21
2.4	Setup used for annealing of the SMA wire . . . . .	22
2.5	Customized SMA shape . . . . .	22
2.6	SMA annealing fixture . . . . .	23
2.7	Relation between strain and arc radius . . . . .	24
2.8	The transformation temperatures of the SMA increase with applied stress. Stress influence ratios can be obtained from the slope of the lines. . . . .	28
2.9	SMA wire bending model . . . . .	30
2.10	Experimental setup used for SMA characterization . . . . .	31
2.11	Geometry of the experimental setup . . . . .	32
2.12	Temperature vs. strain relationship in the constitutive model . . . . .	33
2.13	Encoder readings . . . . .	34
2.14	Temperature vs strain under no loading . . . . .	34
2.15	Change in the location of point $k_5$ . . . . .	36
2.16	Temperature vs. strain under external loading . . . . .	36
2.17	External stress acting on the SMA wire . . . . .	37
2.18	Strain-temperature relation under variable loading. For an SMA wire with 2.1 cm length, the maximum modeling error is $3.67^\circ$ . . . . .	37
2.19	Change in bending angle as SMA wire is heated . . . . .	38
2.20	Relation between strain and bending angle . . . . .	38
2.21	Temperature vs. strain relationship for the SMA wire under no loading . . . . .	40
2.22	External stress acting on the SMA wire as a function of temperature . . . . .	41
2.23	Experimental setup used for the blocked force test . . . . .	42

2.24	Force vs. temperature plot of the blocked force test . . . . .	43
2.25	Temperature vs. strain relationship under variable loading. Maximum modeling error is $\epsilon_{error} = 0.001$ and that corresponds to $\alpha_{error} = 1.16^\circ$ . . . . .	44
2.26	Change in the bending angle as SMA wire is heated . . . . .	45
2.27	Relationship between the bending angle and the arc angle . . . . .	46
2.28	Shape change of the SMA depending on the current flow direction . .	48
3.1	The block diagram of the proposed PWM based NPID controller . . .	56
3.2	Temperature profiles for different current inputs. Solid lines represent the temperature profiles obtained using the empirical model. . . . .	58
3.3	Comparison of different pulse widths and duty cycles . . . . .	58
3.4	Temperature profiles were obtained for different pulse width and current values for $P=200$ ms. Solid lines represent the temperature profiles obtained using the empirical model. . . . .	60
3.5	Change of the desired temperature increase with the PWM input parameter . . . . .	60
3.6	Step-wise temperature references and the temperature change of the SMA . . . . .	63
3.7	Temperature tracking error for the step-wise temperature trajectory .	63
3.8	Continuous polynomial references and the temperature change of the SMA . . . . .	64
3.9	Step-wise reference temperature and the change in temperature of the SMA . . . . .	65
3.10	The change in strain in the SMA and the strain predicted by the model for a step-wise temperature reference . . . . .	66
3.11	A continuous temperature reference and the change in temperature of the SMA . . . . .	67
3.12	The change in strain of the SMA and the strain predicted by the model for a continuous temperature reference . . . . .	67
4.1	Schematic of the discretely actuated steerable probe . . . . .	70
4.2	Components of the discretely actuated steerable probe . . . . .	70
4.3	An actual 2-DOF discretely actuated steerable probe . . . . .	71
4.4	Temperature profile and PWM control signal for PWM-P based temperature controller . . . . .	72
4.5	Shape of the probe after actuation . . . . .	72
4.6	Demonstration of the steerable probe actuated in gelatin . . . . .	73
4.7	The 2-DOF cannula prototype with an imaging window . . . . .	74
4.8	Six markers were placed on the cannula for tracking the configuration.	75
4.9	Bending angle vs. time for the cannula . . . . .	76
4.10	PWM command signals for the two SMA wires . . . . .	76
4.11	Change of bending angle inside translucent gelatin . . . . .	77
4.12	The cannula moving inside the gelatin . . . . .	78
4.13	Temperature vs. strain relationship of the prototype II . . . . .	79

4.14	The experimental setup used for force measurement . . . . .	80
4.15	Experimental setup for the OCT system . . . . .	83
4.16	Details of the OCT probe . . . . .	83
4.17	The actual OCT probe . . . . .	83
4.18	Microstructures of the chicken breast . . . . .	84
4.19	Microstructures of the porcine tissue . . . . .	84
4.20	Histogram of chicken breast OCT images . . . . .	85
4.21	Histogram of porcine tissue OCT images . . . . .	85
4.22	The inner wall of the cannula, sheath and tape . . . . .	86
4.23	OCT images at various angles . . . . .	87
4.24	At each joint there are two SMA actuators and 1 DOF. The markers were attached on the outer surface for tracking the pose of the cannula.	89
4.25	Schematic of the discretely actuated steerable cannula . . . . .	90
4.26	Progression of back and forth joint motion - Solid line corresponds to the actuated SMA actuator and dashed line corresponds to the unactuated SMA actuator. . . . .	90
4.27	Temperature vs. strain relationship for the prototype III . . . . .	91
4.28	Discretely actuated steerable cannula has a pair of antagonistic SMA actuators at each joint. . . . .	93
4.29	Experimental setup used for the tracking experiments. . . . .	94
4.30	Tracking of the joint trajectories using the PWM-based controller. There are 6 datasets for trajectory 1 and 3 datasets for trajectory 2. The average root-mean-square error (RMSE) for trajectory 1 is 0.6414° and RMSE for trajectory 2 is 0.5816°. . . . .	95
4.31	Tracking of the joint angle trajectories using PWM-based controller using both SMA actuators. The chattering decreases since both of the SMA actuators compensate for the error. The RMSE for experiment 1 is 0.4094° and RMSE for experiment 2 is 0.3749°. . . . .	96
4.32	Tracking sinusoidal trajectories (Trajectory 1= $-2.75 \cos(0.03 \pi t) + 2.75$ , Trajectory 2= $4 \cos(0.03 \pi t) - 4$ ). The RMSE for trajectory 1 is 0.6753° and RMSE for trajectory 2 is 0.7696°. . . . .	97
4.33	Discretely actuated steerable cannula made of machinable ceramic . .	98
4.34	Heat transfer between antagonistic SMA actuators for different ma- terials . . . . .	100
5.1	The schematic used for the forward kinematics map . . . . .	103
5.2	Motion in 3D . . . . .	106
5.3	The change of joint angles with time . . . . .	108
5.4	The change of joint angles with $\eta$ . . . . .	109
5.5	The change of 3D position with time . . . . .	109
5.6	Errors along the trajectory . . . . .	110
5.7	The variables used in geometric relations . . . . .	113



5.8	Example to illustrate the physical joint limit of the SMA actuator. The obstacles and the final position are inside the workspace of the cannula. However, the maximum joint angle required for trajectory is $25.0726^\circ$ which is $4.0726^\circ$ above the physical limit of the SMA actuator.	114
5.9	Motion planning problem used for analyzing the joint limit . . . . .	117
5.10	Change in $\alpha_2$ with time for the trajectory shown in Figure 5.9 . . . .	117
5.11	The maximum recoverable strain of the SMA actuator depends on the initial strain $\epsilon_o$ and the stiffness $K$ . . . . .	119
5.12	Change in joint limits with time . . . . .	121
5.13	Change in joint variables with and without the additional task of joint limit avoidance. The case with joint limit avoidance has the joint variables with subscript <i>new</i> . . . . .	121
5.14	Movement of the obstacles and the motion of the cannula in trajectory A. The cannula and the obstacles are shown in a darker color as the time progresses. . . . .	123
5.15	Change of joint variables with time for trajectory A . . . . .	123
5.16	Movement of the obstacles and the motion of the cannula in trajectory B. The cannula and the obstacles are shown in a darker color as the time progresses. . . . .	124
5.17	Change of joint variables with time for trajectory B . . . . .	124
5.18	PRR kinematics is a valid simplification that can capture the arc-shaped SMA. Dashed lines represent PRR kinematics. . . . .	125
6.1	Needle and ultrasound transducer configurations: (a) out-of-plane tracking, (b) in-plane tracking, (c) out-of-plane tracking with an angle.	130
6.2	Linear rail system used for the ultrasound experiments. . . . .	133
6.3	Schematic of the control system: The image acquisition rate is fixed at 15 Hz, and hence the hardware control is done with another PC at 60 Hz. The serial port communication takes 15 ms. Therefore, the hardware control is currently limited to 60 Hz. . . . .	135
6.4	The markers are the tracked features (points). A line was plotted to connect the two points to show the orientation of the cannula tip. (a) Two points were selected (shown on left). The point at the tip shifted across the needle cross-section due to pixels having similar brightness as the cannula was further inserted into the tissue phantom (shown on right). This introduces an error in the angle calculation. This means the pixels that are further down the cross-section had similar brightness with the ones that were originally selected on the top surface. (b) This figure shows another example where the algorithm fails in the beginning when a point on the distal link was selected. When a point on the top surface was clicked with the mouse, the algorithm detected a feature (a brighter edge) that is lower down the cross-section.	138
6.5	Schematic of a 2-DOF planar cannula. . . . .	140

6.6	Ultrasound beam width and spatial resolution experiments: (a) The schematic of the experimental procedure, (b) the ultrasound images of the object from left to right: the object starts to appear - the object has maximum visibility - after 0.597 cm (center hole)- after 1.029 cm - object starts to disappear, (c) the dimensions of the object, and (d) the dimensions of the object that were measured using the ultrasound console . . . . .	144
6.7	Pseudocode of the in-plane tracking algorithm . . . . .	145
6.8	The top surface of the cannula was clearly resolved after applying the Sobel operator to the pre-processed images. . . . .	146
6.9	Using the optical flow algorithm with brightness enhancement, the cannula can be tracked in real-time: (a) Cannula shape was overlayed on the ultrasound images from the experiment, and (b)the change in joint variables in time . . . . .	146
6.10	<i>Ex-vivo</i> bovine kidney image with (right) and without (left) the cannula. Soft-tissue has more intensity variation compared to the tissue phantom made of gelatin, yet the cannula is still the brightest line in the image. . . . .	147
6.11	Morphological operations remove the amount of noise and detail. Sobel operator detects the top surface of the cannula. The output of the Sobel operator is overlayed on the original image and used as an input to the in-plane tracking algorithm. . . . .	147
6.12	<i>Ex-vivo</i> bovine kidney experiment: (a) The Sobel operator was applied to the pre-processed images. (b) The shape of the cannula was successfully detected and drawn on the ultrasound images. . . . .	148
6.13	(a) Needles that were used in <i>ex-vivo</i> bovine experiments, (b) ultrasound image (left) and the processed image (right) of the prostate brachytherapy, and (c) ultrasound image (left) and the processed image (right) of the coaxial biopsy needle. . . . .	149
6.14	Color map of the ultrasound image (top) and the processed image (bottom) for the (a) prostate brachytherapy needle, (b) coaxial biopsy needle, and (c) discretely actuated steerable cannula . . . . .	149
6.15	To demonstrate tip detection using circular Hough transform, the ultrasound transducer was slid over the cannula and the images were recorded with 0.127 cm intervals. . . . .	150
6.16	The images show (a)the pre-processed images prior to the application of circular Hough transform, and (b) the original ultrasound images. From left-to right: the cannula starts to appear - a bright region is observed which corresponds to the upper part of the cross-section (bevel-tip)- the cannula cross-section is detected. . . . .	151
6.17	Pseudocode of the out-of-plane tracking algorithm . . . . .	152
6.18	Change in ultrasound transducer rotation and position, and the cannula displacement with time . . . . .	153

6.19	Ultrasound images: (a) before the ultrasound transducer rotates (initially the tracking is in-plane), (b) when ultrasound transducer is rotated, (c) 90° rotation is achieved and the cannula tip is observed ahead of the ultrasound transducer, and (d) the transducer moves towards the cannula and the circular cross-section is detected. The location of the tip is $[x, y, z] = [56.05, 40.30, 58.75]$ mm in the imaging plane. . . . .	154
------	------------------------------------------------------------------------------------------------------------------------------------------------------------------------------------------------------------------------------------------------------------------------------------------------------------------------------------------------------------------------------------------------------------------------------------------------	-----

## List of Abbreviations

RFA	Radio-frequency Ablation
SMA	Shape Memory Alloy
PWM	Pulse Width Modulation
RTD	Resistance Temperature Detector
OCT	Optical Coherence Tomography
RCM	Remote Center of Motion
MRI	Magnetic Resonance Imaging
DOF	Degrees of Freedom
FPS	Frame Per Second
ROI	Region of Interest

## Chapter 1: INTRODUCTION

### 1.1 Motivation

Percutaneous needle-based procedures such as biopsy and radio-frequency ablation (RFA) require guidance of the needle to the target region for therapy or diagnosis. These needles need to be steered to the target location by a variety of maneuvers at the distal end of the needle. Frequently, due to errors in targeting, they have to be withdrawn slightly and re-inserted to make trajectory corrections as they are guided inside the soft-tissue. The problem is further compounded when there is a change in the tissue consistency as the needle traverses through the tissue or there is presence of calcified regions, which can deflect the needle from its pre-planned trajectory. Targeting errors correspondingly lead to sampling errors and poor treatment outcomes.

Some of the common examples of percutaneous needle-based procedures are prostate brachytherapy, breast biopsy and radio-frequency ablation. Prostate brachytherapy is a common form of treatment for early-stage prostate cancer. Prostate cancer is the most common malignancy in men and it is the second most common cause of cancer death, after lung cancer with 233,000 estimated new cases, and 29,480 deaths from prostate cancer in the United States only in 2014 [1]. Prostate brachytherapy

is a radiation therapy where radioactive seeds are injected through needles directly into the prostate gland to destroy the cancer cells. Intraoperative treatment planning is commonly performed using contiguous transverse images of the prostate from the transrectal ultrasound to determine a treatment plan containing needle locations and the number of seeds and dosage [2]. The average seed placement error reported with manual needle insertions under ultrasound guidance is approximately 6.3 mm and that corresponds to 15% of the average prostate diameter [3]. The clinical targeting error of the magnetic resonance imaging guided robotic prostate biopsy system that has been used in the US National Cancer Institute for over 6 years was reported as 4.3 mm [4]. These seed placement errors can lead to suboptimal implant dosimetry. In some cases seeds are placed outside of the prostate, in the bladder, the urethra, or the circulatory system that may correspondingly lead to adverse effects from radioactivity [5, 6].

Breast biopsy is a needle-based procedure in which breast tissue samples are removed using a needle. The goal is to insert the needle to the suspicious site determined by the physician and get a small sample tissue for breast cancer diagnosis. Breast cancer is the most common cancer among women, except for skin cancers. According to The American Cancer Society's estimates for breast cancer in the United States for 2014, about 232,670 new cases of invasive breast cancer will be diagnosed in women and 40,000 women will die from breast cancer [1]. Mammogram and ultrasound can find a suspicious area. However, they cannot directly tell whether the suspicious site is cancerous. A needle biopsy needs to be performed for further pathological analysis. Image guided percutaneous needle biopsy of the breast

is widely practised. The simplest procedure is fine needle aspiration, in which a thin fine-gauge needle is inserted into the tumor. Due to limited tissue extraction it can give a false negative result. A core needle biopsy is used when more information about a breast lump is required and when it cannot be achieved with a mammogram, ultrasound, or fine needle aspiration alone. Larger needles, commonly as large as 11 gauge or 14 gauge, are frequently deployed. A stereotactic breast biopsy system incorporates a digital camera system that scans the breast structure with x-rays. In a stereotactic core biopsy targeting study, it was found that the tissue and needle displacements cause a total positioning error of 2.4 mm, which limits the attainable diagnostic accuracy [7]. After a core needle breast biopsy procedure, a small metal clip may be inserted into the breast to mark the site of biopsy in case the tissue proves to be cancerous and additional surgery is required. These clips are dislodged from the tip of a needle. These clips can be introduced through a flexible introducer [8]. A clip deployment study was performed over a hundred clips were deployed using a 11 gauge and a 18 gauge needle [9]. The position of 70% of 11-gauge clips and 63% of 18-gauge clips were within 1 cm of the pre-biopsy calcifications.

Percutaneous radio-frequency ablation (RFA) is another needle-based minimally invasive procedure offering excellent patient recovery and lower rates of procedure-related complications. It is mostly used to treat patients with unresectable primary and metastatic hepatic cancers. It is an *in-situ* ablation method and it is desirable compared to the extirpative approach. It is commonly performed to treat tumors in lung [10], liver [11] and kidney [12]. In a RFA procedure, the

tumor or other dysfunctional tissue is ablated using a needle electrode. The electrode has an array of hooked tines that are coaxially deployed after the RFA probe is placed into the ablation zone. In general, RFA is an effective treatment for unresectable tumors less than 6.0 cm in diameter. Tumors larger than 2.5 cm require more than one deployment of the needle electrode [13]. It is desirable to minimize the number of insertions since each insertion causes a substantial tissue damage. Interstitial flexible ultrasound applicators made of a array of tubular piezoceramic radiators can also be used for thermal ablation of the soft-tissue [14]. Burdette *et al.* combined real-time spatially tracked image guidance with directional interstitial ultrasound ablation [15]. A targeting study was performed by placing 1 mm targets inside pig liver and 3-4 mm targeting accuracy was achieved.

Targeting errors may lead to false negatives in biopsy procedures, imprecise delivery of radiation therapy in brachytherapy procedures and ablation of healthy tissue in radio-frequency ablation procedures. There are many challenges in reducing targeting errors and achieving accurate needle targeting in the aforementioned needle-based procedures. Needle-tissue interaction causes needle to deflect from its pre-planned trajectory. Tissue inhomogeneity and the variability in tissue properties between individuals make the needle trajectory hard to predict. Additionally, needle insertion and tissue deformation cause the movement of the target and the organ. Automation of needle insertion procedures can eliminate the human error and decrease the targeting error. However, some sites are inaccessible using straight trajectories due to the presence of calcified regions and anatomical obstacles that need to be avoided. These targeting challenges motivate the need for a discretely



actuated needle that can generate localized forces to correct for errors in trajectory execution. We envision a multi degree of freedom cannula with a hollow inner core that can generate steering forces and follow trajectories that are not limited to straight-line trajectories. The hollow inner core can also be potentially used to deliver diagnostic and therapeutic (theranostic) tools to a desired region.

## 1.2 Related Work

There are many challenges in achieving accurate targeting in needle-based procedures, and hence there is no single solution to overcome these challenges. There have been various approaches to improve the targeting accuracy of needle-based procedures. The methods presented in this section are effective ways for reducing errors, increasing targeting accuracy and understanding the needle-tissue interaction.

### 1.2.1 Robot-assisted Needle Insertion

Robot-assisted needle insertion combined with image guidance promises to improve the accuracy of percutaneous procedures. Boctor *et al.* proposed virtual remote center of motion control algorithm that guides the needle to the insertion point and orients it to align with the target-entry-point line [16]. This approach enables the needle positioning tasks such as guiding the tip to the desired entry point and pivoting the tip around the entry point and inserting the needle into the body using translation along a straight trajectory. Hata *et al.* developed an MRI compatible manipulator and implemented virtual remote center of motion (RCM)

control that interactively selects the optimal needle insertion path for liver ablation therapy under open-configuration MRI [17]. This system allows the physician to select the needle insertion path while maintaining remote center of motion at the tumor site. Fichtinger *et al.* presented a robotically assisted prostate brachytherapy system [18]. The robot moves the needle guide onto the entry point over the perineum and orients it to the desired angle. The physician inserts the preloaded needle into the guide sleeve, and enters the needle into the desired depth while observing its progress using ultrasound. Yang *et al.* developed a fully MRI compatible master-slave surgical system for breast biopsy that operates under continuous MRI [19]. The slave robot is located under the space of the breast coil and the master robot enables the physician to adjust needle orientation and it can be locked in place to help the physician maintain a stable needle orientation while performing needle insertion. Robots aid in aligning the needle with the target and robot-assisted procedures have high positioning accuracy. However, the trajectory errors that arise after the insertion due to the needle-tissue interaction still needs to be accounted for.

### 1.2.2 Modeling Needle Tissue Interaction

Developing needle deflection and tissue deformation models for needle insertion is essential to improve the targeting accuracy of percutaneous procedures. DiMaio and Salcudean took the lead in modeling the tissue deformations due to needle insertion [20]. Using a 3-DOF planar robotic manipulator, insertion forces were

recorded and the phantom tissue deformation was calculated by tracking markers placed on the phantom. They developed a two-dimensional linear elastostatic finite element material model and introduced a needle manipulation Jacobian that relates the needle tip motion to needle base motion using the finite element model of the tissue [21]. Hence, the steering is achieved by manipulating the needle at the base. Misra et al. presented an analytical model for the loads developed at the bevel tip of a 1.5 cm diameter needle during needle-tissue interaction [22]. Roesthuis *et al.* developed a mechanics-based model which predicts the deflection of a bevel-tipped needle during insertion into soft tissue [23]. The needle was modeled as a cantilever beam supported by a series of springs that have constant interaction stiffness. Chentanez *et al.* developed a simulator for needle insertion into the prostate that uses local meshing where needle is modeled as a 1-D elastic rod and tissue model is discretized using tetrahedral meshes [24]. These models are useful for developing needle insertion simulators to generate haptic feedback and achieving accurate visualization for surgical training. Mechanical modeling of living tissues is one of the most crucial challenges and is still has not been fully explored. Tissue deformation is complex and shows variability between individuals. It is mostly inhomogeneous, and has nonlinear and viscous behavior. Therefore, without any active control on the needle, purely relying on the deflection and position information of the needle that are calculated using linear elastic assumptions may lead to errors.

### 1.2.3 Tissue Manipulation

Manipulating the tissue is another way to improve the accuracy of targeting. Torabi *et al.* proposed the use of single-point tissue manipulation using a robotic device to improve the accuracy of prostate cancer brachytherapy procedure by pushing obstacles and sensitive tissues away from the needle path to increase target accessibility [25]. Mallapragada *et al.* presented a control architecture for the tissue manipulators to guide the tumor towards the line of insertion of the needle for the breast biopsy procedure [26]. Physicians already perform such tissue manipulation by hand. These works provide more insight into tissue manipulation in terms of the number of palpation points needed and where the tissue manipulators should be located.

The methods presented so far are effective in achieving high positioning accuracy prior to insertion and reducing the targeting error during needle insertion. Achieving non-straight trajectories and accessing sites that are not accessible using straight trajectories still remains as a challenge. It would be advantageous to be able to make large trajectory corrections. This can be achieved by designing new needles that can overcome the limitations of the conventional rigid needles.

### 1.2.4 Steerable Needle Design

Kuhle proposed a biopsy needle with an asymmetric tip such as convex, flat, or concave shaped to take advantage of the lateral deflecting force acting on the asymmetric tip [27]. To avoid an obstacle, a needle with a bevel tip can be rotated

into a position such that the bevel faces away from the desired direction of the arc. Advancing the needle through tissue naturally deflects the needle into the desired arc. The amount of deflecting forces generated at the needle's tip is proposed to be controlled by appropriately selecting the design parameters such as needle diameter and bevel surface area.

The needle deflection due to tip asymmetry is more profound when the tip has bevel tip. Beveled needles bend much more than cone or triangular tipped needles [28]. Physicians often spin the needles by hand to reduce needle bending and achieve straight trajectories during insertion. Webster *et al.* proposed using a needle with a bevel tip made of nitinol that is less than 1 mm in diameter and more flexible compared to the tissue [29]. The tip asymmetry can aid in steering around obstacles by controlled rotations at the base of the flexible needle. The steering capability of flexible needles has been demonstrated on homogeneous and fairly stiff phantom tissues [30,31]. In this method of steering, the tip deflection is coupled to the insertion distance. Therefore lateral motion cannot be achieved without further insertion of the needle. Flexible needles need tissue reaction forces to generate asymmetric forces at the needle tip for steering. Hence, the tissue properties have a profound effect on the performance of steering. If there is a change in the tissue consistency as the needle moves through the tissue, the needle can deflect from its pre-planned trajectory. Since these needles are flexible and there is no local actuation, the minimum radius of curvature is limited.

Another method for steering is to use telescoping concentric tubes. There are several patented designs that involve a rigid cannula and a more flexible stylet

with a curved distal portion made of a superelastic material such as Nitinol [32–34]. When the flexible stylet is extended beyond the tip of the rigid cannula, it can be curved to its pre-defined curvature. The steering direction is selected by rotating the stylet. In this approach, curvature direction can be selected prior to extending the stylet beyond the cannula tip. However, it has not been demonstrated whether the curvature direction can be changed once the stylet is inside the soft-tissue. Heaven and Klapper proposed a steerable surgical device that is composed of an inner tubular member and an outer tubular member that are pre-bent in a curved configuration [35]. By rotating the inner and outer tubular members with respect to each other the device can be oriented. When both tubes are oriented in the same direction the device bends, when they are oriented in opposite direction both tubes are deformed and the device straightens. A similar yet more improved design was proposed where telescoping curved concentric tubes with different stiffness are used [36,37]. Depending on the actuation of a particular tube in the group, bending forces can be generated along the entire length of the tube. This design can be grouped under continuum robots. By rotating and extending the tubes with respect to each other a resultant curvature is obtained. Bedell *et al.* presented an optimization procedure to design the pre-mentioned concentric tube robots for applications in intracardiac surgery to achieve a desired workspace within the anatomy constraints [38]. The algorithm finds the desired number of tubes as well as the curvature and length selection of each curved tube. Curved concentric tubes have potential use in procedures involving open cavities such as endonasal surgery [39] and intracardiac surgery [40].

Another way to achieve steering is using a tendon-driven actuation. Seeker<sup>®</sup> is a manually-operated tendon-driven needle marketed by PneumRx Inc. for use in lung biopsy. When the joystick located at the hub is flexed, cables located along the stylet are shortened thus causing the needle to bend. Kratchman *et al.* designed a robotically controlled system and used a digital camera feedback to control the tip of the Seeker [41]. As far as the author is aware, there is no study that shows how much force can be generated using Seeker and whether it can be applied to other organs such as breast tissue where steering forces are required.

### 1.3 Discretely Actuated Steerable Cannula

Due to the nonlinear, non-homogeneous nature of the soft tissue and anatomical obstacles, trajectory planning and execution are challenging. These targeting challenges motivate the need for a discretely actuated needle that can generate localized forces to correct for errors in trajectory execution, rather than relying on the needle and soft tissue interaction forces for steering. Smart materials including, but not limited to, shape memory alloys, piezoelectric actuators and electroactive polymers can also be used in needle and cannula design to generate steering forces. Among these materials, SMAs are attractive, where large forces or displacements are required and limited space is available. SMA actuators have been used as artificial muscles for prosthetic limbs [42] and in the design of the active catheters [43–45]. To overcome the reaction forces, achieve precise positioning and exert force on the soft-tissue to make trajectory corrections during insertion, it is advantageous to have

actuators along the length of the needle or the cannula. We want to take this a step further and use the hollow inner core of the cannula to deliver theranostic tools to the target region. Figure 1.1 demonstrates some of the envisioned applications of the discretely actuated cannula. The cannula can be integrated with a core biopsy probe to reduce sampling errors and it can be used for introducing a diagnostic probe such as OCT that is capable of imaging *in-vivo* at high resolution to assess tumor margin. Such a cannula is also advantageous for a RFA procedure. The cannula can be steered to adjacent regions when the tumor size is large, and hence the number of needle insertions can be minimized. It is important to note here that the cannula has a bevel tip and can also do passive steering.

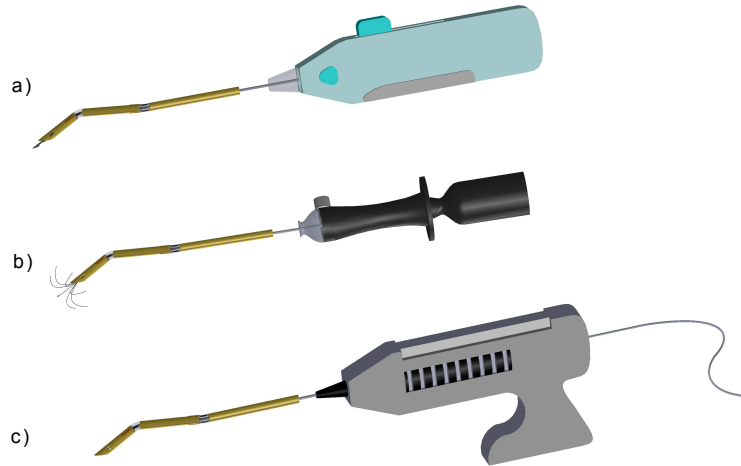


Figure 1.1: This figure demonstrates the anticipated use of the discretely actuated steerable cannula as a delivery tool for therapeutic and diagnostic applications such as a) biopsy, b) RFA, and c) OCT imaging. The final designs or the incorporated tools can be different.



## 1.4 Dissertation Overview

The introduction chapter presents the current limitations of needle-based procedures and the motivation for developing a discretely actuated steerable cannula. Chapter 2 gives the background on the shape memory effect and the arc-shaped SMA actuator. The constitutive model of the SMA is given and the important parameters of the model that need to be determined experimentally are discussed. A step-by-step characterization procedure is presented to find the parameters of the SMA actuator. Chapter 3 describes the PWM-based controllers that are used for temperature feedback and image-feedback control of the SMA actuators. Chapter 4 describes the design of the prototypes. The improvements of each prototype over the previous prototypes are discussed. The evaluation of the cannula involves testing of the PWM-based controllers, demonstration of the cannula to aid in OCT imaging, and experiments inside a tissue phantom made of gelatin. In Chapter 5, a trajectory planning algorithm using geodesics is presented and a trajectory execution scheme is demonstrated. Configuration control approach is introduced to take advantage of the redundancy of the cannula. The algorithm can generate trajectories that satisfy multiple criteria such as joint limit avoidance and obstacle avoidance. Chapter 6 describes an in-plane image processing algorithm that tracks the cannula in 2D and an out-of-plane tip detection method that localizes its tip using 2D ultrasound. These algorithms are aimed to be used for ultrasound-guided steering of the cannula. Finally in Chapter 7, we make some concluding remarks and discuss the directions for the future work.

## 1.5 Dissertation Contributions

The main contributions of this dissertation can be summarized as follows:

- **Design of a Steerable Cannula**

-This dissertation presents a novel discretely actuated hollow needle (cannula) that employs SMA actuators for generating steering forces inside soft-tissue. The cannula can be potentially used to introduce diagnostic and therapeutic tools through its inner core.

- **SMA Modeling and Control**

-The uniaxial constitutive model of the SMA that describes the tensile behavior was extended to one-dimensional pure-bending case to model the phase transformation of an SMA wire that transforms into an arc.

-A step-by-step experimental characterization procedure was devised to obtain the parameters of the SMA that are used in the constitutive model.

-It was demonstrated that temperature-feedback can be effectively used to control the strain of the arc-shaped SMA actuator using the constitutive model of the SMA. A PWM-based temperature controller was developed which can effectively track continuous temperature trajectories.

- **Motion Planning**

-A configuration control-based motion planning algorithm was formulated to steer the cannula to the desired location without exceeding the maximum

recoverable strain of the SMA actuators while avoiding obstacles. The constitutive model was incorporated into the motion planning algorithm to actively determine the joint limit of the SMA actuator.

- **Ultrasound-based Tracking**

-Spatial resolution and ultrasound beam-width are two important parameters that effect the accuracy of the ultrasound-based tracking algorithms and yet they are commonly overlooked while assessing the accuracy of the tracking algorithms. A simple procedure was established to quantify the beam width and spatial resolution of the ultrasound transducer to assess the tracking accuracy.

-An in-plane tracking algorithm based on optical flow was developed to track the cannula configuration using 2D ultrasound. Spatial and temporal coherence assumptions of the optical flow algorithm make it troublesome to apply it to the ultrasound images where there are spatial and temporal intensity variations. A pre-processing step was developed that alleviates the assumptions of the optical flow algorithm. Using this method, the top surface of the needles can be highlighted and smooth intensity can be achieved which makes it possible to use the fast and powerful optical flow algorithm to track the features of the cannula in ultrasound images.

-An out-of-plane tracking algorithm based on circular Hough transform was developed to localize the needle-tip. A scanning method was introduced which takes advantage of the bevel tip and the circular cross-section of the cannula. This method guarantees that the detected circle is the cannula-tip.

## Chapter 2: SHAPE MEMORY ALLOYS

This chapter discusses the arc-shaped SMA actuator and its characterization process. In Section 2.1, the background of the SMA and the shape memory effect are described. In our application, SMA wires are annealed in an arc shape and the radius of curvature changes during phase transformation. The shape-setting of the arc shape and the setup used for SMA annealing are discussed in Section 2.2. SMA behavior is a function of three variables: stress, strain and the temperature of the SMA. The constitutive model that describes the relationship between these three variables is introduced in Section 2.3. Section 2.4 describes the step-by-step characterization procedures for the SMA actuators. One of the actuators is a commercially available SMA actuator and the other one is a drawn Nitinol which does not exhibit any shape memory effect prior to annealing. Finally, Section 2.5 has some concluding remarks. Most of the contents of this chapter were published in [46, 47].

### 2.1 Fundamentals of SMA

Shape memory effect (SME) is a unique property of certain alloys exhibiting martensitic transformation. When the alloy is deformed in the low temperature phase, it recovers its original shape upon heating above a critical temperature. When

shape memory effect is exhibited upon heating, it is called one-way shape memory. Some materials also undergo a change in shape upon cooling. The first shape memory transformation was observed by Chang and Read in AuCd alloy in 1951 [48]. Buehler *et al.* discovered the shape memory effect in equiatomic nickel-titanium (Ni-Ti) and it was publicized as Nitinol in 1963 [49]. It was discovered at Naval Ordnance Laboratory (NOL) and hence the acronym Nitinol was derived from Nickel Titanium Naval Ordnance Laboratory. Ni-Ti alloys are the most practical shape memory alloys. The recoverable strain of Nitinol is up to a maximum of about 8% [50]. The mechanical properties of SMAs vary greatly over the temperature range spanning their transformation. One of the biggest challenges in SMAs is in developing the proper processing procedures to yield the desired properties. SMAs make great actuators. Large shape changes can be induced easily and in a constrained situation large stresses can be generated. Since the resistance of the SMA is small, it can be heated using resistive heating without any complicated hardware. Another key characteristic of SMAs is their unique pseudoelasticity. Pseudoelasticity refers to the material's ability at the high temperature phase to undergo large strains during loading and then recover upon unloading. Hence, SMA has an elastic response to an applied stress at the high temperature (parent) phase. This is widely employed in designs that require superelasticity. Because of their biocompatibility, NiTi SMA have become a material of choice for stents, guidewires and many other medical devices. Superelasticity enables designing medical devices and implants that can be squeezed inside tight spaces.

It is important to understand what happens at the microscale to understand

the macroscopic behavior of SMA. SMA has two main crystal structures: a high temperature phase called austenite and a low temperature phase called martensite. In a stress-free state at high temperatures, SMA has a body-centered cubic crystal structure. When the temperature is reduced in the unstressed state, at low temperatures the phase changes from austenite to martensite. The martensite phase either has a randomly twinned structure with multiple variants or a stress-induced detwinned structure where multiple variants converts to a single variant under stress. The transformation from austenite phase to twinned martensite is achieved through thermal transformation and results in a negligible shape change. The transformation from twinned martensite to detwinned martensite occurs when a sufficient level of external stress is present. Stress-induced detwinned can accommodate relatively large deformation and recover large strains when transformed into the austenite phase upon heating. The martensite can be deformed with low stress since the bonds between the atoms are not broken in the process. Only the rearrangement of the atoms change during detwinning. These small atomic displacements result in a macroscopic shape change that can be observed. The one-way shape memory effect is depicted in Figure 2.1. Almost all the mechanical, electrical and thermal parameters of martensite and austenite phases such as resistivity, Young's modulus and specific heat are different. The austenite phase is relatively stiff and has much higher Young's modulus compared to the martensite phase. The stress-strain curve of the SMA is shown in Figure 2.2.

SMA is initially at point A in the martensite phase at a low temperature. When there is loading, SMA initially deforms elastically up to the critical stress,  $\sigma_s^{cr}$

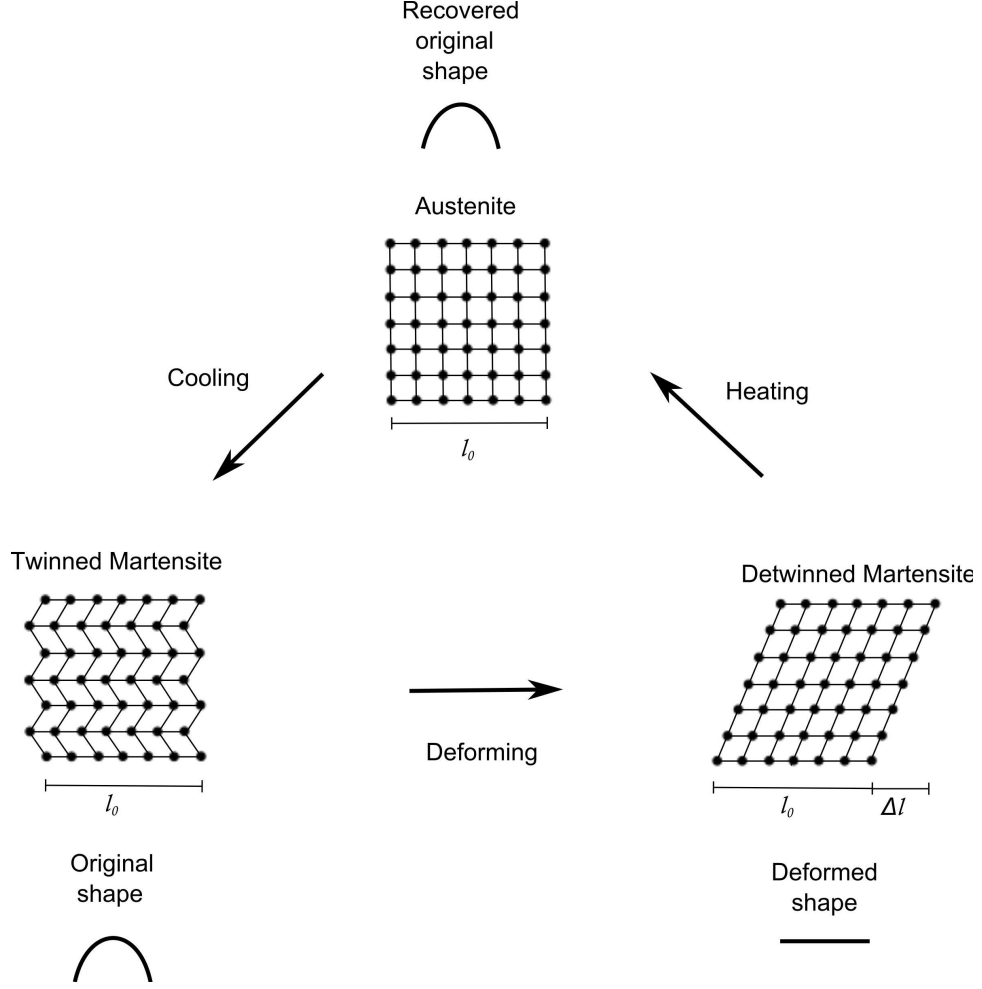


Figure 2.1: One-way shape memory effect

at point B. When the applied stress exceeds the critical stress, the detwinning starts and all the variants are aligned in the loading direction. At point C, the stressed-induced martensitic transformation is completed. During unloading the material is at point D and only the elastic deformation is recovered. There is the remaining residual strain,  $\varepsilon_r$ . If the SMA is now heated above the transformation temperature, the material transforms into austenite and recovers the residual strain. If the material is now cooled, the SMA transforms into the low temperature martensite phase while the shape remains the same as in the high temperature austenite phase.

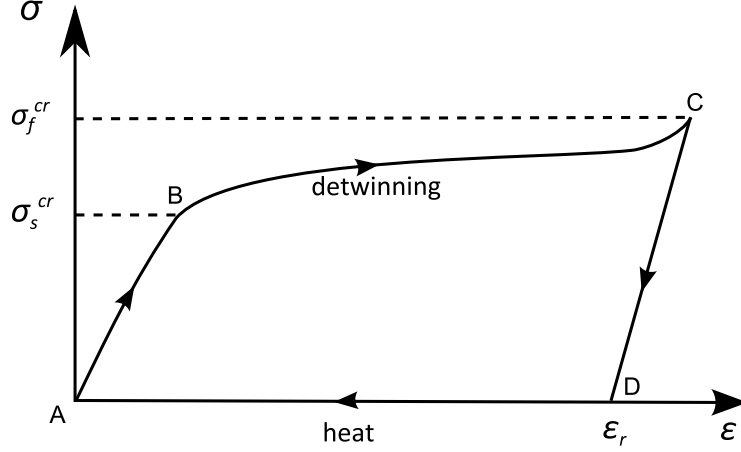


Figure 2.2: Stress-strain behavior in the one-way shape memory effect

It is important to note that if the stress at point C exceeds the yield strength of the material, plastic deformation occurs and strain can be recovered partially upon heating. In other words, if the residual strain  $\varepsilon_r$  is larger than the maximum recoverable strain  $\varepsilon_L$  of the SMA wire, only  $\varepsilon_L - \varepsilon_r$  can be recovered.

In the stress-free state SMA can be characterized by four different transformation temperatures. An important characteristic of the phase transformation is the hysteresis. For temperatures below the austenite start,  $A_s$ , the material is in the 100% martensite phase. Between martensite start and austenite start temperatures ( $M_s < T < A_s$ ) there is no phase change. Once the temperature is increased beyond  $A_s$ , the material starts transforming into the austenite phase. For temperatures above  $A_f$ , the material is in the 100% austenite phase. In the cooling cycle, for temperatures above  $M_s$ , the material is in 100% austenite phase. Once the material cools down below  $M_s$ , martensite starts to form. Below the martensite finish temperature,  $M_f$ , the material is in 100% martensite phase. When the temperature of the SMA is between  $A_s < T < A_f$  or  $M_f < T < A_s$ , the material is



partially in the martensite phase and partially in the austenite phase. The phase transformation is characterized by the martensite volume fraction. When the SMA is in 100% martensite phase, the martensite volume fraction is equal to 1 and it is equal to 0 when the SMA is in 100% austenite phase. Figure 2.3 shows the change of martensite volume fraction in the phase transformation range.

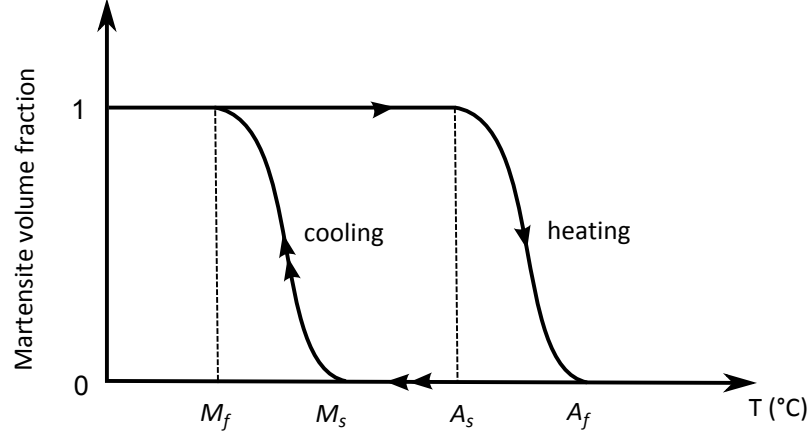


Figure 2.3: Transformation temperatures of the SMA under no stress

## 2.2 Annealing of Arc-shaped SMA

Annealing (or shape-setting) of SMA is a thermally-induced process which can occur inside a furnace or via resistive heating with high current. SMA is shape-setted inside a small furnace to make sure temperature distribution is uniform along the length of the wire. The SMA wire is first deformed into the desired arc shape and clamped down to a ceramic fixture using bolts as in Figure 2.4. SMA wire can also be annealed in a customized shape that has a straight portion for attachment and an effective section for bending as in Figure 2.5. The effective part of the SMA wire which contributes to bending is the arc and the parts shown with dashed lines

are straight and remain straight upon thermal actuation. A customized jig was also developed to anneal multiple SMA wires in the desired shape as shown in Figure 2.6.

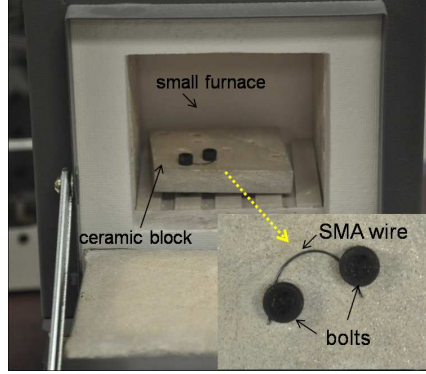


Figure 2.4: Setup used for annealing of the SMA wire

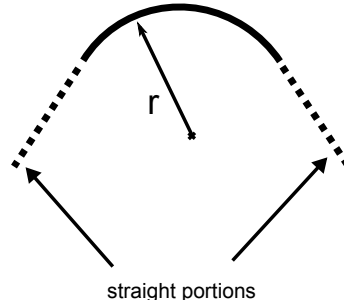


Figure 2.5: Customized SMA shape

One of the important considerations before annealing is to select the desired radius of curvature of the SMA wire. If we consider an initially straight wire bent into the circular arc shape as shown in Figure 2.7, the relationship between strain and the arc radius can be derived as:

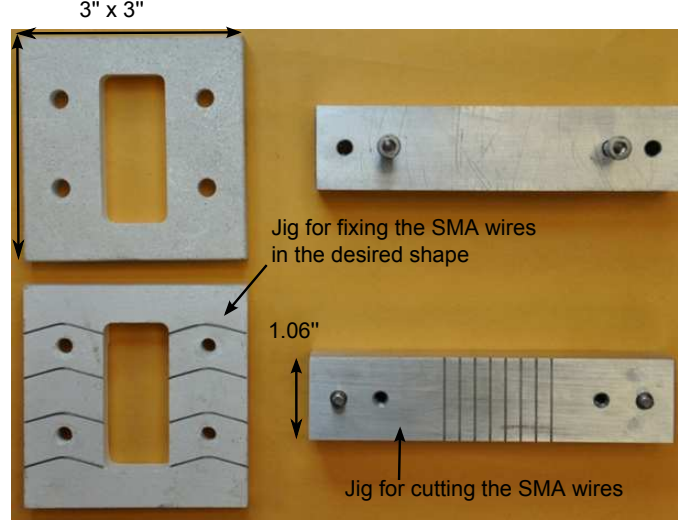


Figure 2.6: SMA annealing fixture

$$\varphi(r + \frac{d}{2}) = \ell + \epsilon\ell \text{ and } \varphi = \frac{\ell}{r} \implies r = \frac{d}{2\epsilon} \quad (2.1)$$

where,  $d$ , is the diameter of the SMA wire and  $\ell$ , is the length of the section of radius,  $r$ , and arc angle,  $\varphi$ . Nitinol can recover strains up to 8% for low-cycle use or up to about 2.5% strain for high-cycle use [51]. For instance, for a 0.508 mm diameter SMA wire, 2.5% strain corresponds to a 10.16 mm radius of curvature. A radius of curvature above 10.16 mm has a strain smaller than 2.5%. For a given length of the SMA wire, a smaller arc radius corresponds to a larger bending angle. Another consideration is the transformation temperature range (the difference between the temperature at which the SMA starts to deform and the temperature at which the transformation is complete). A wider transformation range is advantageous since a wider range increases the resolution of the bending angle. The smaller the transformation range, the higher the resolution that is required for the temperature controller, since a small temperature fluctuation can result in a large change in the

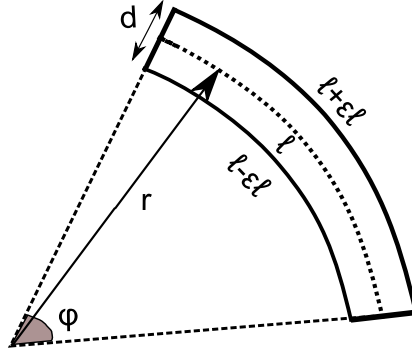


Figure 2.7: Relation between strain and arc radius

bending angle. Achieving the desired transformation temperature is not trivial. The transformation temperatures of the annealed SMA wire depend on various factors such as the percentage of Nickel and Titanium, the level of cold work, the annealing time and annealing temperature. Among these factors, the annealing time and the annealing temperature can be varied by trial and error to achieve the desired transformation temperatures. The proper selection of a sheath that covers the SMA actuators for heat insulation would relax the requirement on the maximum allowable transformation temperature for a medical procedure.

SMA has high fatigue life. For instance, when an SMA wire with strain level below 4% is subjected to cyclic bending between maximum strain and zero strain, it starts to fatigue after approximately  $2 \times 10^4$  cycles [52]. Due to the characteristics of the SMA actuator, it has a one-way shape memory effect after the annealing process is completed. Upon heating the SMA above its phase-transition temperature (martensite to austenite phase), the SMA transfers to the desired arc shape. Cooling down the SMA wire causes a transformation from austenite to twinned martensite

without any shape change. Therefore for each joint, antagonistic SMA wires are needed for bending in either direction. The mechanical, electrical and thermal properties of the SMA wire change after annealing. The SMA actuator needs to be characterized after the annealing process to determine the properties of the actuator. The arc-shaped SMA can then be used in a robotic device to generate joint torques.

### 2.3 Constitutive Model of SMA

SMA characteristics are primarily dependent on the external stress, strain and temperature and their associated time derivatives. These variables are interdependent and the SMA behavior is a nonlinear function of these variables. Most of the constitutive models have been developed for one-dimensional quasistatic loading, and as such, it is assumed that the material at each instant is in thermodynamic equilibrium [53–55]. Since stress is a function of temperature  $T$ , the martensite volume fraction  $\lambda$ , and strain  $\epsilon$ , the material constitutive relation in the differential form is given by [53]:

$$d\sigma = \frac{\partial\sigma}{\partial\epsilon}\epsilon + \frac{\partial\sigma}{\partial\lambda}\lambda + \frac{\partial\sigma}{\partial T}T \quad (2.2)$$

This leads to the a general expression:

$$d\sigma = E(\epsilon, \lambda, T) + \Omega(\epsilon, \lambda, T) + \Theta(\epsilon, \lambda, T) \quad (2.3)$$

where  $E(\epsilon, \lambda, T)$  represents the Young's modulus of material,  $\Omega(\epsilon, \lambda, T)$  is transformation tensor and  $\Theta(\epsilon, \lambda, T)$  is thermal coefficient of expansion for the SMA material. Since the strain in the SMA due to thermal expansion is significantly lower than the strain due to phase transformation, this coefficient is normally neglected.

We use the model developed by Tanaka [53] to characterize the SMA actuator. In Tanaka's model, the strain,  $\epsilon$ , temperature,  $T$ , and martensite volume fraction,  $\lambda$ , are assumed to be the only state variables. The stress,  $\sigma$ , in the material is calculated from these quantities. From Equation 2.3, the constitutive equation is derived as [53]:

$$\sigma - \sigma_o = E(\lambda)(\epsilon - \epsilon_o) + \Omega(\lambda)(\lambda - \lambda_o) + \Theta(\lambda)(T - T_o) \quad (2.4)$$

where  $E$  is the Young's modulus in the elastic regime of the material,  $\Theta$  is a thermoe-  
lastic constant, and  $\Omega$  is the phase-transformation constant. The terms associated with subscript 'o' refer to the initial state of the material. The elastic modulus is defined as:

$$E(\lambda) = E_A + \lambda(E_M - E_A) \quad (2.5)$$

Let us consider a SMA material in the austenite phase ( $\lambda_0 = 0$ ) at the zero stress/strain condition ( $\epsilon_o = 0, \sigma_o = 0$ ). If the material is cooled down to the martensite phase and stretched to the maximum recoverable strain ( $\epsilon_o = \epsilon_L, \lambda = 1, \sigma = 0$ ) From Equation 2.4, the transformation constant,  $\Omega$ , can be determined as [54]:

$$\Omega(\lambda) = -\epsilon_L E(\lambda) \quad (2.6)$$

where  $\epsilon_L$  is the maximum recoverable strain. Martensite volume fraction determines the shape of the temperature-strain curve. The shape of the curve that describes the change in martensite volume fraction with temperature is independent of the SMA phase transformation phenomena and its dependence on stress. Depending on the SMA material used, this curve can be represented with a cosine expression or an exponential expression. Tanaka's model assumes an exponential function

for the martensite volume fraction. During the martensite to austenite (M→ A) transformation,  $\lambda$  is given by:

$$\lambda_{M \rightarrow A}(\sigma, T) = e^{a_A(A_s - T) + b_A \sigma} \quad (2.7)$$

Transformation from austenite phase to martensite phase (A→ M),  $\lambda$  is given by:

$$\lambda_{A \rightarrow M}(\sigma, T) = 1 - e^{a_M(M_s - T) + b_M \sigma} \quad (2.8)$$

where  $a_M$ ,  $b_M$ ,  $a_A$  and  $b_A$  are constants defined as:

$$\begin{aligned} a_M &= \frac{\ln(0.01)}{M_s - M_f} & b_M &= \frac{a_M}{C_M} \\ a_A &= \frac{\ln(0.01)}{A_s - A_f} & b_A &= \frac{a_A}{C_A} \end{aligned} \quad (2.9)$$

where  $C_M$  and  $C_A$  are the stress influence coefficients for the martensite phase and the austenite phase, respectively. The stress influence coefficients quantify the increase in transformation temperatures with applied stress.  $C_M$  and  $C_A$  are constants and they represent the slope of the lines in Figure 2.8. To fully characterize the SMA wire we need to find the transformation temperatures and the stress influence coefficients.

Liang and Rogers utilized the same constitutive relation and assumed a cosine function for the martensite volume fraction [54]. The difference between the two models is the modeling of the martensite volume fraction. In the Liang and Rogers' model,  $\lambda$  is modeled as a cosine function. During the martensite to austenite (M→ A) transformation,  $\lambda$  is given by [54]:

$$\lambda_{M \rightarrow A} = \frac{\lambda_0}{2} \{ \cos[a_A(T - A_s) + b_A] + 1 \} \quad (2.10)$$

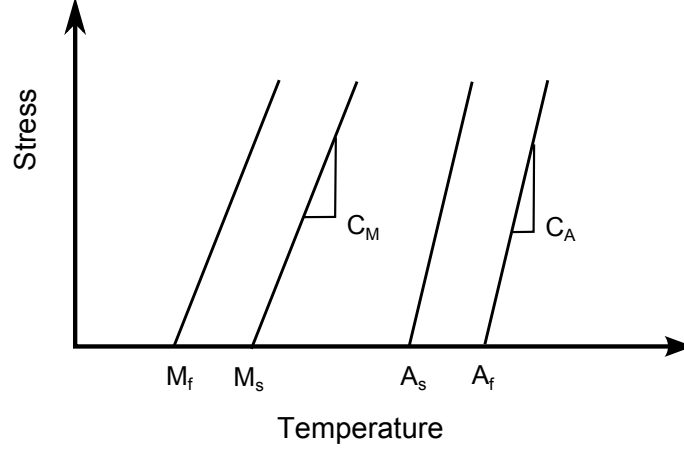


Figure 2.8: The transformation temperatures of the SMA increase with applied stress. Stress influence ratios can be obtained from the slope of the lines.

and for the austenite to martensite ( $A \rightarrow M$ ) transformation,  $\lambda$  is defined as:

$$\lambda_{A \rightarrow M} = \frac{1 - \lambda_0}{2} \cos[a_M(T - M_f) + b_M \sigma] + \frac{1 + \lambda_0}{2} \quad (2.11)$$

the constants,  $a_M$ ,  $b_M$ ,  $a_A$  and  $b_A$  are given as:

$$\begin{aligned} a_M &= \frac{\pi}{M_s - M_f} & b_M &= -\frac{a_M}{C_M} \\ a_A &= \frac{\pi}{A_s - A_f} & b_A &= -\frac{a_A}{C_A} \end{aligned} \quad (2.12)$$

The advantage of using these models is that the parameters are engineering-based and they can be experimentally determined through mechanical testing. They represent the thermomechanical behavior and their mathematical form can be easily incorporated into the control algorithms.

## 2.4 Characterization of Arc-shaped SMA Actuator

Nitinol in the cold work condition has not been subject to a heat treatment. Therefore, the drawn Nitinol does not exhibit shape memory effect prior to the an-



nealing. The mechanical, electrical and thermal properties of the SMA wire need to be determined after annealing. When a commercially available straight annealed SMA wire is used, its mechanical, electrical and thermal properties are available from the manufacturer. However, annealing the SMA actuator changes its transformation temperatures. To effectively design an SMA actuator, it is essential to understand the thermomechanical behavior of the SMA. The material properties are important to develop model-based controllers. Most of the research in SMA characterization and modeling were done on straight annealed SMA wires and springs. Though characterization and modeling of SMA wires and springs in the straight configuration have been extensively studied [56–58], doing similar characterization studies for arbitrarily shaped SMA wires is challenging. The uniaxial testing devices and experimental setup used in characterizing straight annealed SMA wires are not applicable when the SMA wire is annealed in an arbitrary shape. For example, measuring the elastic modulus of the austenite phase is not possible using the conventional tensile testing machine since the SMA wire does not move along a line and it moves in a plane as the temperature of the SMA increases. This section describes step-by-step characterization procedures for the annealed Flexinol<sup>®</sup> and the drawn Nitinol that are annealed in an arc-shape.

To model the phase transformation of an SMA wire that transforms into an arc, the one-dimensional constitutive model of the SMA described in Section 2.3 was used. The arc radius can be related to the strain using the relation  $r = \frac{d}{2\epsilon}$  as described in Section 2.2. When modeling the external stress, we consider the maximum stress acting on the top layer that is under tension as shown in Figure 2.9.

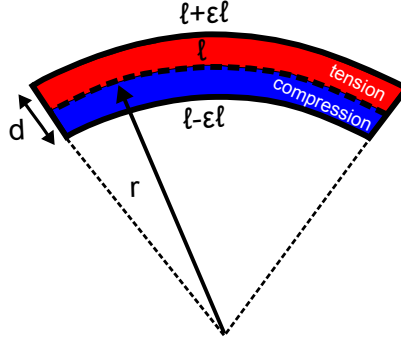


Figure 2.9: SMA wire bending model

Due to the two antagonistic wire setup for each joint, the non-heated SMA wire is naturally deformed by the heated wire. If the bending direction needs to be reversed, the antagonistic SMA actuator is actuated once the actuated SMA wire is cooled to the martensite phase. Therefore, the hysteresis of SMA can be ignored and only the heating cycle needs to be characterized.

#### 2.4.1 Experimental Setup

To measure the strain of the SMA, the experimental setup shown in Figure 2.10 was used. The main frame was previously developed in [59]. The apparatus consists of a rotary encoder and a pin attached at a fixed distance,  $L$ , away from the center of the encoder. As the SMA wire deforms into an arc, it rotates the pin. The pin rotates around the encoder axis. The geometry of the setup is given in Figure 2.11. The origin,  $k_1$ , is defined as the location of the SMA fixer and  $k_2(x, y)$  is the location of the encoder axis. There is a cable connected to the SMA wire at point  $k_5$ . The cable is routed around a screw and goes through a pulley mounted on the

main frame. Constant loading can be applied to the SMA wire by hanging a weight at the tip of the cable. Variable external loading can be applied to the SMA wire by connecting the cable to the extension spring that is connected to a force sensor (MBD-2.5, Transducer Techniques Inc.).

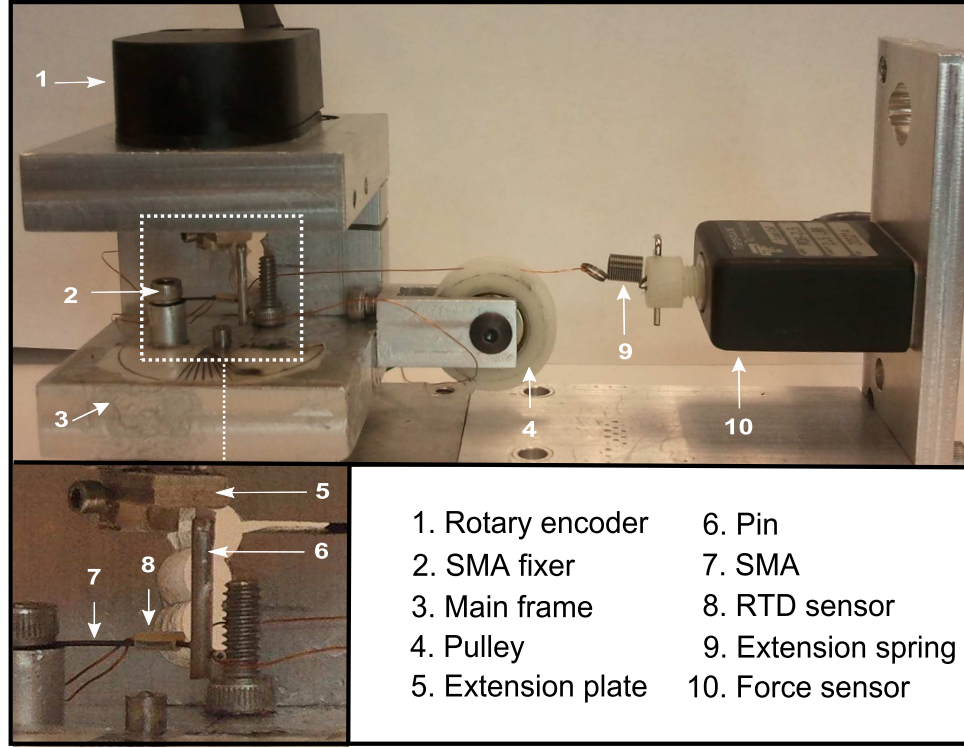


Figure 2.10: Experimental setup used for SMA characterization

From the apparatus geometry, the relationship between encoder reading ,  $\theta$ , and the arc radius,  $r$ , can be found using Equation (2.13).

$$(L\cos\theta + x)^2 + (L\sin\theta + y - r)^2 = r^2 \quad (2.13)$$

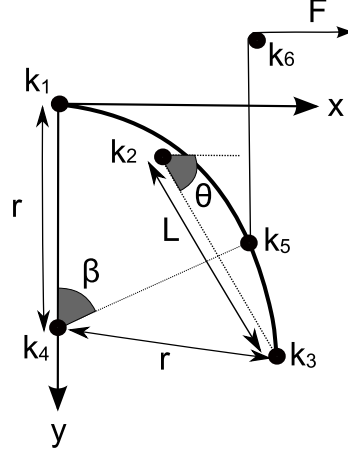


Figure 2.11: Geometry of the experimental setup

## 2.4.2 Characterization of Annealed Flexinol<sup>®</sup>

The SMA actuator used for annealing is a 0.508 mm diameter Flexinol<sup>®</sup>. A small furnace was used to anneal the SMA wire. The SMA wire was first deformed into an arc shape and clamped down to the ceramic fixture using bolts to secure the SMA wire. The bolts were placed such that the radius of curvature is near 15 mm. We obtained a 15.64 mm radius of curvature and that corresponds to 0.01624 strain. Heat treatment of the SMA takes about 40 minutes followed by forced convective cooling with a fan for 10-15 minutes until the ceramic fixture cools down to room temperature.

### 2.4.2.1 Finding Transformation Temperatures

To find the transformation temperatures for the heating cycle of SMA wire,  $A_s$  and  $A_f$ , and to measure the relationship between the strain in the SMA wire and its temperature, the external stress on the SMA wire should be kept constant.

When the SMA wire is straight, the radius of curvature is infinite. As the strain in the SMA wire is computed from the radius of curvature, we analyze the motion from  $\theta = 0^\circ$  ( $\epsilon'$  as shown in Figure 2.12). Initially, the SMA wire is at room temperature in the straight configuration and as the wire is heated beyond  $A_s$ , the wire starts to transform from the martensite phase to the austenite phase. The encoder starts recording when the SMA wire contacts the pin. Above  $A_f$ , the SMA wire recovers its unstrained arc shape.

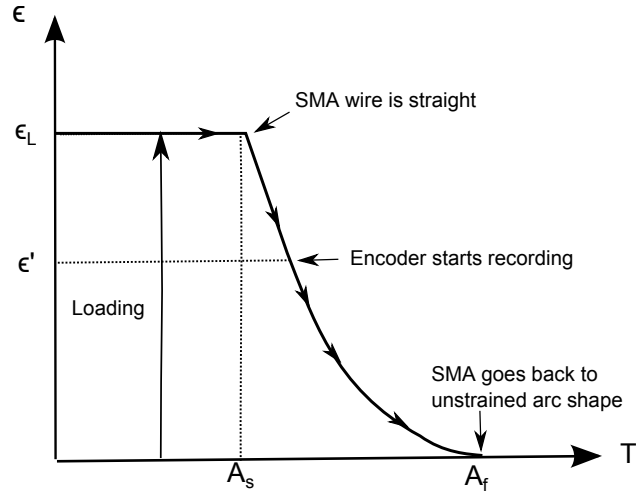


Figure 2.12: Temperature vs. strain relationship in the constitutive model

Four experiments were carried out to find the strain-temperature relation of the SMA wire. A mini resistance temperature detector (RTD) (Alpha Technics , Inc.) was used to monitor the temperature of the SMA wire. To ensure good thermal contact between the RTD sensor and the SMA wire, a thermally conductive paste (Omegatherm 201) was used. To ensure quasistatic deformation, the temperature of the SMA wire was increased incrementally in steps and it was maintained at each intermediate temperature. Figure 2.13 shows the plot of encoder vs. temperature

and Figure 2.14 shows the plot of temperature vs. strain along with the relationship from the model using Equation 2.1. The transformation temperatures  $A_s$  and  $A_f$  were determined to be  $31.5^\circ\text{C}$  and  $54^\circ\text{C}$ , respectively. In the model, maximum strain  $\epsilon_L$  is modeled to be the strain when the SMA wire is deformed into a straight wire and bending angle,  $\alpha$ , is  $0^\circ$ . The maximum strain is 0.01624 and that corresponds to 1.564 cm radius of curvature.

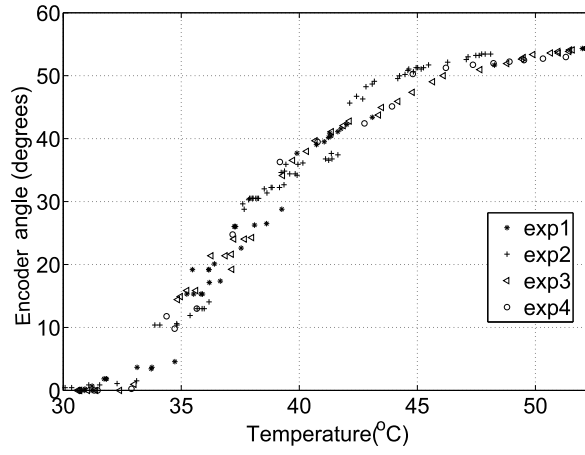


Figure 2.13: Encoder readings

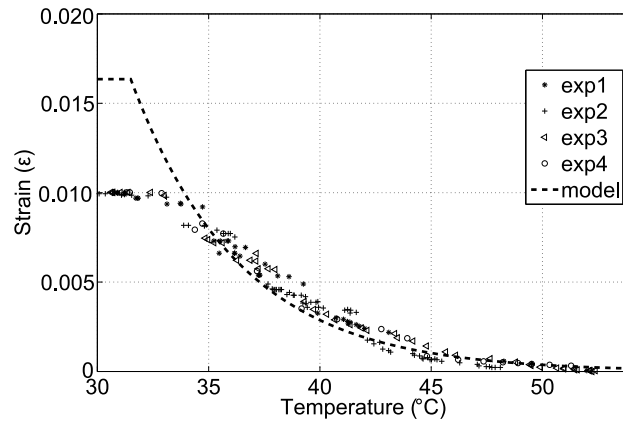


Figure 2.14: Temperature vs strain under no loading

#### 2.4.2.2 Finding Stress Influence Coefficient

Once the transformation temperatures are found, the next step is to find the stress influence coefficient. Stress influence coefficient quantifies the effect of stress on the phase transformation temperatures. Different external loadings can be applied to the SMA actuator by hanging a mass via the pulley. As the temperature of the SMA wire increases, the location of the point  $k_5$ , where the cable is connected to the SMA actuator, changes. Let  $s$  be the distance between the origin (SMA fixer) and point  $k_5$ . For pure bending, the length of the wire remains unchanged and we can thus find the location of point  $k_5$  using:

$$k_5 = (r \sin\beta, r (1 - \cos\beta)) \quad (2.14)$$

where  $\beta = s/r$ . The force direction can be computed by drawing a line between points  $k_5$  and  $k_6$ . Figure 2.15 shows that the angle between the force vector and the x-axis ranges between  $84.74^\circ$  and  $90^\circ$ . Since  $\sin(84.64^\circ) \approx 1$ , we can assume that the force acting on point  $k_5$  is constant and hence characterize the SMA using the maximum stress at point  $k_5$ . Figure 2.16 shows the strain-temperature relation of the SMA actuator under two different loadings. The  $A_s$  values for 30.91 MPa and 40.85 MPa are  $35^\circ\text{C}$  and  $36^\circ\text{C}$ , respectively. The corresponding stress influence coefficient,  $C_A$ , can be calculated as  $8.8 \text{ MPa}/^\circ\text{C}$  and  $9 \text{ MPa}/^\circ\text{C}$ . The average value of  $C_A = 8.9 \text{ MPa}/^\circ\text{C}$  is used.

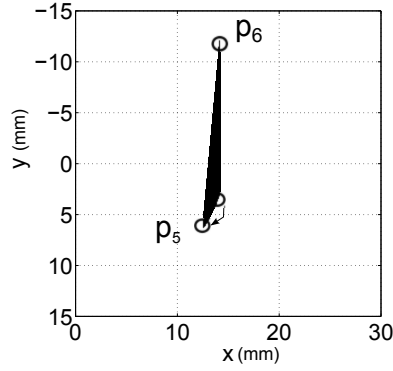


Figure 2.15: Change in the location of point  $k_5$

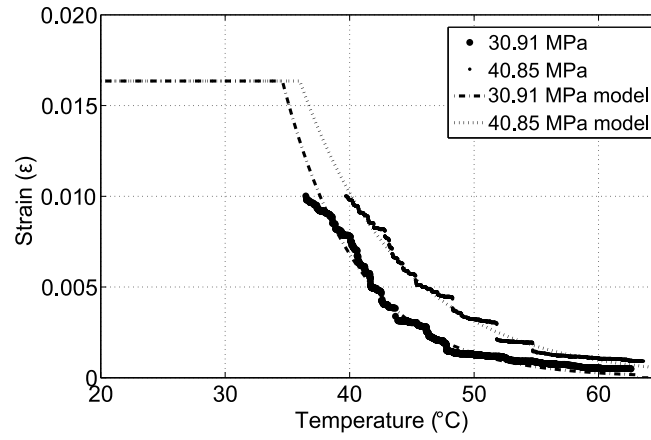


Figure 2.16: Temperature vs. strain under external loading

### 2.4.2.3 Testing Under Variable Loading

To investigate the behavior of the SMA wire and evaluate the model under variable loading, we used the extension spring attached to the force sensor. As the SMA actuator transforms into its original shape from its pre-strained straight condition, it pulls the cable connected to the extension spring. The force exerted by the spring can be recorded using the force sensor. Figure 2.17 shows that the external stress can be modeled as a straight line for this experimental setup. Figure 2.18



shows the strain in the SMA wire and the strain calculated using Tanaka's model with material constants  $C_A = 8.9 \text{ MPa}/^\circ\text{C}$ ,  $E_M = 28 \text{ GPa}$  and  $E_A = 78 \text{ GPa}$ .

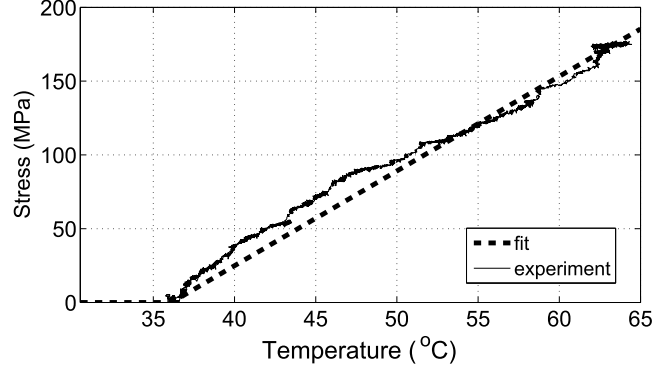


Figure 2.17: External stress acting on the SMA wire

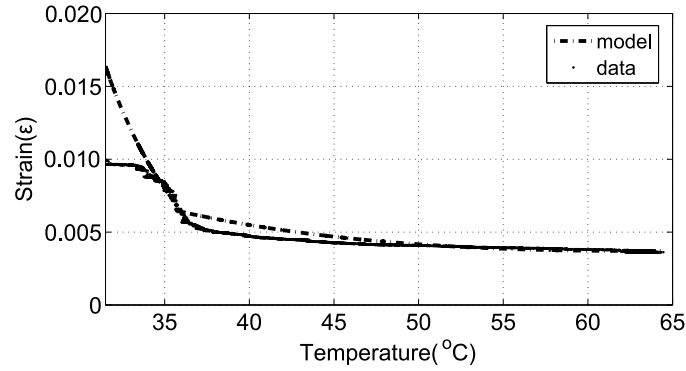


Figure 2.18: Strain-temperature relation under variable loading. For an SMA wire with 2.1 cm length, the maximum modeling error is  $3.67^\circ$ .

#### 2.4.2.4 Finding the Relationship between Bending Angle and Strain

The bending (joint) angle is defined as the angle between consecutive links. The geometric relation between the strain in the SMA wire and the corresponding bending angle needs to be determined. To find this relation, two small links were

attached at both ends of the SMA wire and markers were placed on the links. The optical flow tracking algorithm was used to find the bending angle between the links (Figure 2.19). Figure 2.20 shows the change in bending angle with the strain that was calculated using Tanaka's model at that temperature. The exponential ( $R^2 = 0.9819$ ) curve fit is given by:

$$\alpha = 49.77 e^{-779.1\epsilon} + 17.82 e^{-142.8\epsilon} \quad (2.15)$$

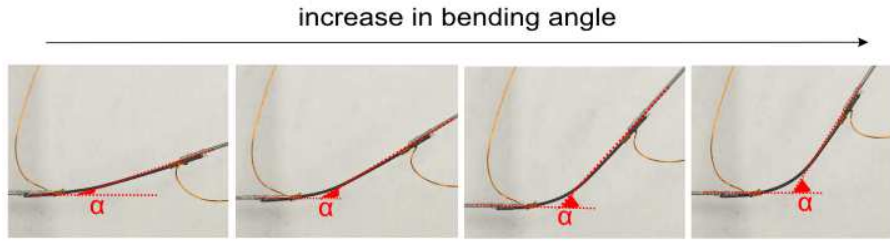


Figure 2.19: Change in bending angle as SMA wire is heated

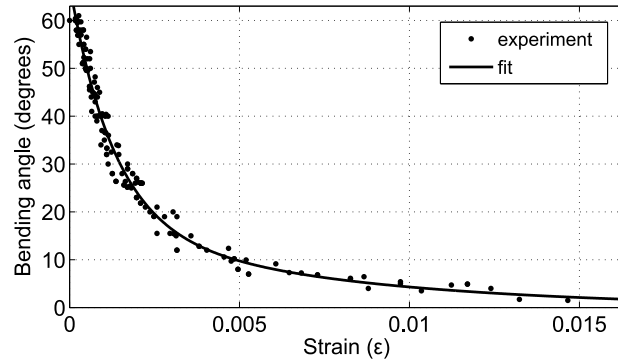


Figure 2.20: Relation between strain and bending angle

### 2.4.3 Characterization of Drawn Nitinol

The SMA actuator is a 0.53 mm diameter drawn Nitinol (Memry, Inc.) wire. The SMA wire was first deformed into an arc shape and clamped down to a ceramic

fixture to keep it fixed during annealing. Heat treatment of the SMA takes about 40 minutes followed by quenching the SMA in a ice-water mixture. After the annealing process is completed, the SMA actuator has one-way shape memory effect and upon heating the SMA actuator above its transition temperature, the SMA actuator can transform into the desired arc shape. The original arc shape has 1.37 cm radius of curvature and straight configuration corresponds to a 0.0195 (1.95%) strain. To fully characterize the SMA wire, we need to find the transformation temperatures, the stress influence coefficient and the elastic modulus of each phase. These constants depend on the particular SMA wire used in the experiments and the annealing parameters (annealing time and annealing temperature). Hence, they need to be determined experimentally. The characterization of the SMA actuator that is annealed from a drawn Nitinol is slightly different than the procedure for characterizing annealed Flexinol. The drawn Nitinol does not exhibit shape memory effect prior to annealing and its mechanical, electrical and thermal properties are completely unknown. During the experiments it was observed that the effect of stress on the transformation temperatures is very small and it is hard to obtain the stress influence coefficient from constant stress experiments. In other words, the stress influence coefficient is large and the shift in the temperature-strain curve due to applied stress is very small to get a reasonable estimate for the stress influence coefficient. Therefore, a regression analysis was applied to obtain the parameters.

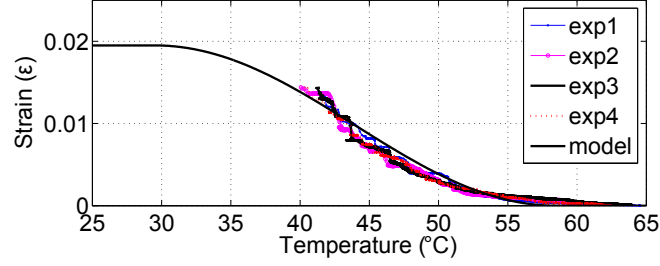


Figure 2.21: Temperature vs. strain relationship for the SMA wire under no loading

#### 2.4.3.1 Transformation Temperatures

To find the transformation temperatures of the heating cycle,  $A_s$  and  $A_f$ , and determine the relationship between the strain and temperature, the third variable, stress, is kept constant. We follow the procedure described in Section 2.4.2.1. Four experiments were carried out to find the strain-temperature relation of the SMA wire. A RTD sensor was attached at the center of a 2.1 cm SMA wire where the maximum deformation takes place. The RTD sensor was attached with the thermally conductive paste to ensure good thermal contact between the sensor and the SMA wire. The temperature of the SMA wire was increased in steps and maintained at each temperature to ensure quasistatic deformation. Figure 2.21 shows the corresponding strain-temperature relation obtained using Equation (2.13) and (2.1). The transformation temperatures  $A_s$  and  $A_f$  were determined to be 29.5°C and 58.5°C, respectively.

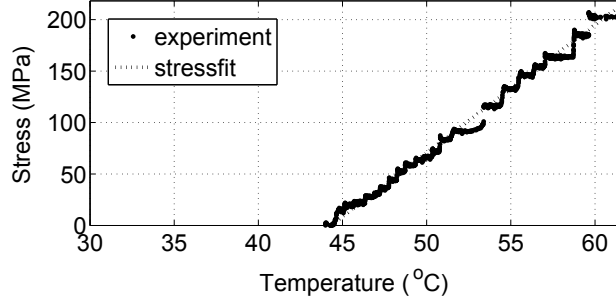


Figure 2.22: External stress acting on the SMA wire as a function of temperature

#### 2.4.3.2 SMA Parameters Related to Stress

To investigate the behavior of the SMA wire under variable loading and find the stress related coefficients, variable loading was applied to the SMA wire using the extension spring. As the SMA actuator transforms into its original shape, it pulls the cable connected to the extension spring. The force exerted by the spring can be recorded using the force sensor. During phase transformation, the location of the point  $k_5$ , where the cable is attached to the SMA, also changes. The angle between the force vector and the x-axis ranges between  $83.11^\circ$  -  $87.66^\circ$ . Since  $\sin(83.11^\circ) \approx 1$ , we can assume that the force acting on point  $k_5$  is perpendicular to the motion of the SMA wire and we can hence characterize the SMA actuator using the maximum stress at point  $k_5$  corresponding to the layer under tension. Figure 2.22 shows that the external stress can be modeled as a straight line for this setup.

The unknown parameters  $E_A$ ,  $E_M$  and  $C_A$  can be found by applying nonlinear regression analysis using the experimental data for temperature, strain and stress. It is important to note that the slope of the strain-temperature curve is mainly

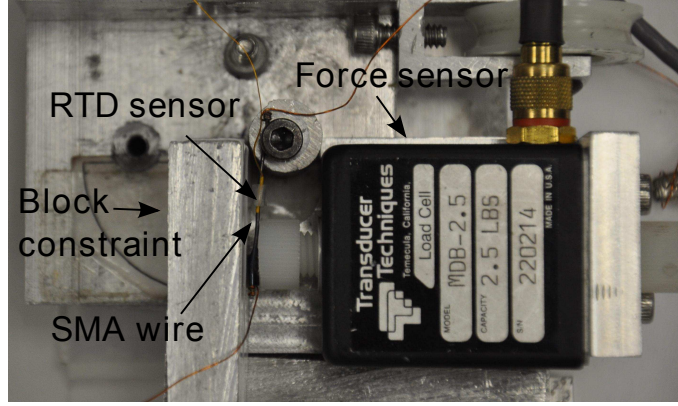


Figure 2.23: Experimental setup used for the blocked force test

determined by  $E_A$  and  $C_A$  and different combinations of these parameters can fit the strain-temperature data. For example, if  $C_A$  is small, high  $E_A$  values are required to satisfy fit the experimental data. Therefore, we carried out a blocked force test to find the upperbound on the elastic modulus in the austenite phase,  $E_A$ . To estimate  $E_A$ , the experimental setup shown in Figure 2.23 was used to perform a blocked force test. In the blocked force test, strain in the wire is kept constant ( $\epsilon - \epsilon_o = 0$ ) and initially the SMA wire is in a stress free state ( $\sigma_0 = 0$ ) at room temperature ( $\xi_o = 1$ ). Using these conditions and neglecting the thermoelastic stress contribution, the constitutive equation (Equation 2.4) simplifies to:

$$\sigma = -\epsilon_L E(\lambda)(\lambda - 1) \quad (2.16)$$

where  $\epsilon_L$  is the maximum recoverable strain ( $\epsilon_L = \epsilon_o$ ). At temperatures above  $A_f$ , the SMA wire is in the austenite phase ( $\lambda = 0$ ) and the constitutive equation further simplifies to:

$$\sigma = \epsilon_o E_A \quad (2.17)$$

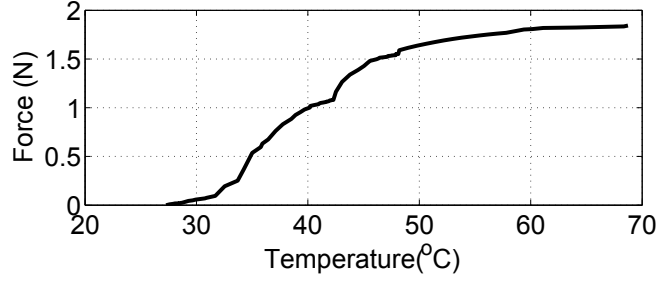


Figure 2.24: Force vs. temperature plot of the blocked force test

Figure 2.24 shows the change in the force generated by the SMA wire as temperature of the wire increases. If we assume only pure bending and neglect the effect of shear stresses in the SMA wire, we can model the stress in the SMA wire using beam theory. For an SMA wire of length  $\ell$  and area moment of inertia  $I$ , the maximum stress can be related to the force,  $F$ , generated by SMA wire as:

$$\sigma_{max} = \frac{F\ell(d/2)}{I} \quad (2.18)$$

Using Equation (2.17) and (2.18), the maximum value that  $E_A$  can take is determined to be 132.34 GPa. It is difficult to know where exactly the SMA wire contacts the pin that is attached to the force sensor. We assume that the force measured by the force sensor is concentrated at the tip of the SMA wire and hence we overestimate  $\sigma_{max}$  (hence the maximum value  $E_A$  can take). This experiment shows that  $E_A$  cannot be more than 132.34 GPa. To find the unknown parameters  $E_A$ ,  $E_M$  and  $C_A$ , we used nonlinear curve-fitting approach using the least-squares method (*lsqcurvefit* function in MATLAB). The lower-bound and upper-bound for the coefficients were defined as:

$$[4, 20000, 60000] < [C_A, E_M, E_A] < [50, 70000, 132340] \quad (2.19)$$

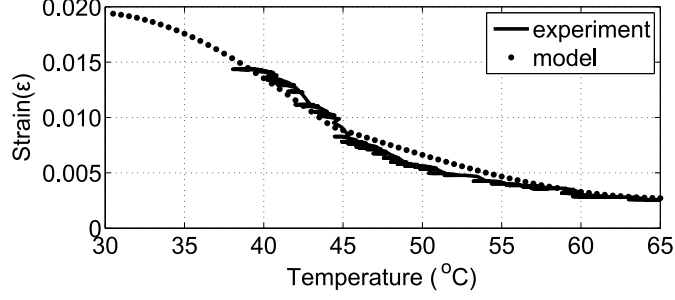


Figure 2.25: Temperature vs. strain relationship under variable loading. Maximum modeling error is  $\epsilon_{error} = 0.001$  and that corresponds to  $\alpha_{error} = 1.16^\circ$ .

The units for the parameters,  $E_A$ ,  $E_M$  and  $C_A$ , were defined as MPa, MPa and MPa/°C, respectively. For the lower-bounds, the parameters of other commercial SMA wires were used which are known to be softer compared to the one that we use. The algorithm converged to parameter values  $[30, 49960, 104720]$ . Figure 2.25 shows the strain in the SMA wire and the strain calculated with the parameters that we found using *lsqcurvefit*.

If external stress is zero or known, the strain will only be a function of temperature. The constitutive model enables us to find the corresponding strain at a particular temperature.

### 2.4.3.3 Geometric Relations

To find the relationship between the bending angle and the arc angle,  $\varphi$ , the same approach in Section 2.4.2.4 was applied. Two small links were attached at both ends of the SMA wire and markers were placed on the links. The tracking algorithm was used to find the bending angle between the links (Figure 2.26). Figure 2.27



shows the relationship between the arc angle and bending angle. Corresponding data points for arc angle were calculated by evaluating the Liang and Rogers' model using the temperature data points of the experiment. The polynomial curve fit ( $R^2 = 0.99$ ) is given by:

$$\alpha = 0.0001372\varphi^3 - 0.01077\varphi^2 + 0.976\varphi + 0.7839 \quad (2.20)$$

where  $\varphi$  is related to strain by:

$$\varphi = \frac{2\epsilon\ell}{d} \quad (2.21)$$

For bending angles smaller than  $20^\circ$ , the arc angle can be assumed to be equal to the bending angle as it is approximately seen in Figure 2.27.

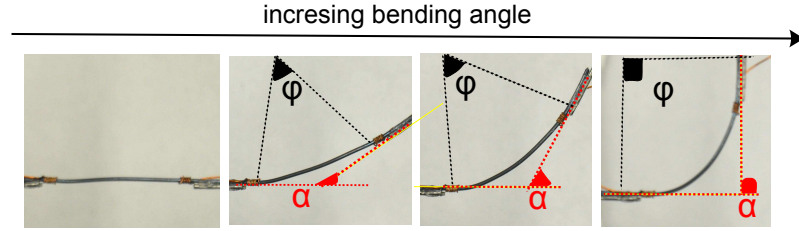


Figure 2.26: Change in the bending angle as SMA wire is heated

## 2.5 Summary and Discussions

This chapter described the design and characterization of an arc-shaped SMA actuator that can be used to generate joint torques. The radius of curvature of the SMA actuator changes during phase transformation. The constitutive model of the SMA for uniaxial loading was applied to the arc-shaped SMA actuator and it was demonstrated that the model can also be used to predict the behavior of the

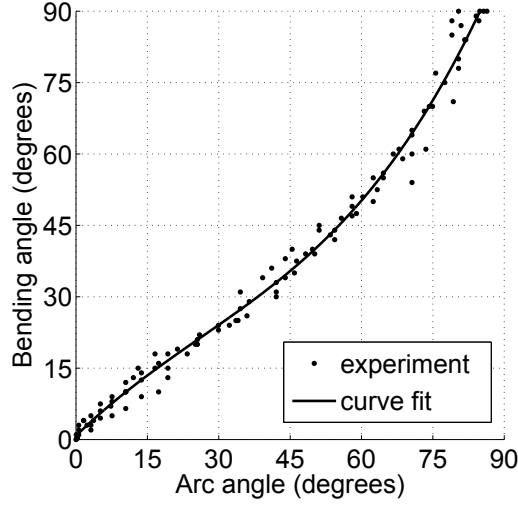


Figure 2.27: Relationship between the bending angle and the arc angle

SMA for bending. The experiments show that the strain of the SMA actuator can be reliably measured by monitoring the temperature of the SMA actuator. This implies that the temperature of the SMA actuator can be used as a feedback to control the strain of the actuator. A characterization procedure was developed to find the parameters of the SMA actuator that are used in the constitutive model.

There are important points to be considered and need further exploration. When the SMA is subjected to external loading in the austenite phase and the stress exceeds the critical stress at which stress-induced martensite occurs, phase transformation from austenite to martensite can be induced. Tanaka's model and Liang and Rogers' model neglect the stress-induced martensite. For our application the external stress,  $\sigma$ , is a function of the strain,  $\epsilon$ . As the bending angle increases the cannula displaces tissue and correspondingly the external stress acting on the cannula increases. Above  $A_f$ , the material is in the austenite phase, which is a stable

state at zero stress. Regardless of the extent of loading, at the end of unloading, the material regains the austenite phase. Once the desired angle is reached, there is no more tissue deformation and the only external stress acting on the SMA is the external stress due to tissue relaxation. We have not performed any studies to measure the tissue relaxation forces, hence it is not known whether the tissue relaxation forces can induce stress-induced martensite. It is reported that the tissue relaxation forces settles down to around half of the maximum force generated during deformation. For example, this value corresponds to approximately 1 N for porcine liver [60]. Any stress-induced martensite formed during the actuation due to tissue deformation (if the critical stress is exceeded) returns back to the austenite phase (as long as the stress due to the tissue relaxation is not above the critical stress). Using Brinson’s model, the stress-induced martensite can be incorporated into the model. In this model, the martensite volume fraction is divided into two parts: temperature-induced martensite and stress-induced martensite. To use this model  $\sigma_s^{cr}$  and  $\sigma_f^{cr}$  need to be determined. For straight annealed SMA wires these parameters can be determined from a tensile test. For the arc-shaped SMA actuator it is hard to obtain a stress-strain curve. Using our experimental setup a constant or variable stress can be applied at a particular location on the SMA. However, in order to obtain a stress strain curve, the loading should be controlled. The stress generated in the SMA should be along the original deformation plane so that SMA preserves the arc-shape and does not deformed in the arbitrary loading direction.

During annealing trials, it was observed that the SMA wires that are annealed in the straight configuration and the arc shaped configuration do not have the same

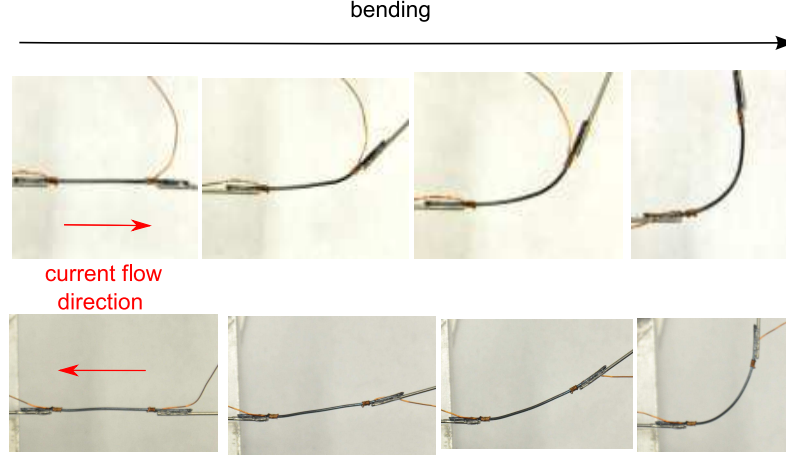


Figure 2.28: Shape change of the SMA depending on the current flow direction

transformation temperatures. They also have different Young's modulus. The drawn Nitinol is a straight wire and for annealing the arc-shaped SMA wire is deformed into an arc shaped and constrained using bolts. Hence, it is under more stress compared to the wires that are annealed in the straight configuration. This might be one of the possible reasons for the variation of the material properties. This implies that one cannot do a tensile test on straight annealed SMA wires that are annealed under the same conditions and use its parameters. Once these critical stress values are determined, stress-induced martensite can be incorporated into the model. Brinson's model represents the shape memory effect from martensite as well as pseudoelasticity and the shape memory effect from austenite [55]. However, this model satisfies the conditions when only the stress increases or only the temperature decreases. In the case of simultaneous change of temperature and stress, this model also needs to be modified.

In our approach, the SMA was modeled using the maximum stress value at

the top layer under tension. Bending is quite different than pure tension. During bending top layer of SMA is under tension while bottom layer is under compression or vice versa. Locally the change in strain (radius of curvature) fits the model well. Each layer of SMA contributes to the total bending angle. Experiments showed that the bending angle is not the same as the arc angle as oppose to what one would expect using the geometrical relations. Hence, the relationship between the arc-shape and bending angle was found. A better way of characterizing the SMA actuator is to measure the strain locally at multiple locations. Another interesting observation is that the direction of current flow effects the shape change. Figure 2.28 shows the shape change of the SMA actuator at different direction of current flow. This could be due to resistive heating. It is important to use the same current flow direction for all the SMA actuators of the cannula.

## Chapter 3: PWM-BASED CONTROL OF SMA

### 3.1 Motivation and Related Work

The behavior and the properties of SMA depend on the temperature and the stress acting on it. Phase transformation, heat transfer and changes in stress and temperature of the SMA material are highly nonlinear. These nonlinear characteristics present difficulties in designing control systems to control the SMA actuators. Most of the work on SMA modeling and control has concentrated on straight annealed SMA wires and springs whereby the phase transformation results in linear motion. The general approach to controlling the SMA is to directly measure the position of the SMA actuator and use a bias spring or a linear actuator to apply forces on the SMA actuator during cooling for recovery [61–64]. The strain and the force measurements are then fed back to the control loop to generate control inputs using the proposed controllers. (See [65] and [66] for a review of different linear and nonlinear control strategies). Tracking a desired trajectory is more difficult than controlling the position of the SMA actuator due to the nonlinear nature of the SMA. When SMA is used as an actuator in a compact device, actuating the SMA actuator becomes a further challenge. Direct measurement of strain and controlling the forces acting on the SMA become impractical.

Electrical resistance of the SMA wire changes during phase transformation and it can be used as a feedback to control the position of the SMA actuator. This is an attractive approach since the electrical resistance is an internal parameter and its measurement does not require an additional sensor. However, SMA has a low resistance and most of the work that implement resistance feedback use 22-100cm length SMA wires [62, 67–69] or multiple SMA wires that are connected in series to increase resistance of the SMA wire [70]. During phase transformation the resistance change of a 2.1cm SMA wire that is annealed in our laboratory is approximately  $0.02\ \Omega$ . A sensitive hardware capable of measuring multiple significant digits may be used to measure the resistance variation during phase transformation. However, this is not possible based on the available hardware in our laboratory. Hence, resistance change has poor resolution and is not a suitable strategy for using in feedback control.

Temperature feedback presents a powerful approach to control the strain in the SMA wire using the constitutive model of the SMA. The constitutive model describes the relationship between the stress, strain and the temperature of the SMA actuator [53–55]. Temperature feedback can be used with a PWM controller for SMA actuation. PWM is an efficient way to actuate the SMA [71, 72] and can be used to control the temperature of the SMA wire along with a linear compensator such as PI, PD, or PID. SMA is a natural low pass filter and is not disturbed by the switching of the input power. PWM can be easily implemented using hardware or software and it is robust to external disturbances. PWM also enables multiple SMA actuation simultaneously using a single power supply [46, 73].

To control the position of the cannula, a combined image-guided control and a model-based temperature feedback control is proposed. The main feedback is image-based as the cannula will be steered with image guidance in a MRI, CT, or ultrasound imaging environment. The image-based feedback controller treats the SMA as a black box since the bending angle is directly measured. When the image feedback from the imaging modality is not optimal, the controller can switch to the temperature feedback controller. In this combined approach, the bending angle (strain) is measured by the imaging modality and the temperature is measured using the temperature sensor. In temperature feedback approach, only the heating cycle of the SMA is used. When one of the actuators is actuated the other one is naturally deformed. If the bending direction needs to be reversed, the controller switches to the antagonistic SMA actuator once the actuated SMA wire is cooled to the martensite phase. This approach increases the execution time of a joint trajectory. However, there is no need to model the hysteresis loop in this approach and this simplifies the control problem. Additionally in trajectory planning, repeated switching between antagonistic actuators is not desirable since that increases the temperature of the two SMA actuators which in return increases the elastic modulus. The elastic modulus of the high temperature austenite phase is 1.5-2 times higher than that in the martensite. Therefore, the actuated SMA wire also needs to overcome the high mechanical resistance of the unactuated SMA wire. This is not energy efficient and should be avoided. Minimum number of switching between the actuators can be given as a constraint in trajectory planning, hence switching between the actuators can be minimized. If the external stress is known, the strain



of SMA is only a function of its temperature.

### 3.2 Implementation of PWM-based Controllers

PWM was implemented with a switching circuit. Sensoray 626 DAQ card (Sensoray, Co. Inc) generates a digital on/off signal to control the solid state relays (SSRs). The maximum turn on time of the SSR is  $50\mu s$  and the maximum turn-off time is  $300\mu s$ . The discrete on/off control signal converts the continuous current into an equivalent PWM output signal. The heating time of the SMA wire,  $\Delta t$ , in a heating period,  $P$ , is computed using the desired control law. The duty cycle is  $\Delta t/P$ . During the interval  $\Delta t$ , the switch for the selected SMA wire is closed and current is supplied for  $\Delta t$  milliseconds. Once the interval is over, the switch is opened until the end of the period. The controller can switch to other SMA wires once the heating time of the actuated SMA wire is completed. Therefore, multiple SMA wires can be actuated in the same period. For example, when a PWM controller with a proportional compensator (PWM-P) is used, the control law for the heating time  $\Delta t$  can be computed as:

$$\begin{aligned}\Delta t &= K_p e \\ e &= x^d - x\end{aligned}\tag{3.1}$$

where  $x^d$  is the desired temperature or bending angle and  $x$  is the current value of the controlled variable. If PWM is used with a PI compensator (PWM-PI), then the heating time can be computed as:

$$\Delta t_i = K_p e + K_i \int (e) dt\tag{3.2}$$

The proportional gain,  $K_p$ , and the integral gain,  $K_i$ , can be tuned to adjust the system performance. Heating period,  $P$ , should be long enough to supply enough current to heat the SMA actuator while compensating for the heat loss. It should not be too long that there is substantial temperature drop in the other SMA actuators. Typical values for  $P$  can be selected between 100ms to 1s.

### 3.3 PWM-based Nonlinear PID (NPID) Controller

Tracking a desired trajectory is more challenging than controlling just the position of the SMA actuator since the desired path is continuously changing. Consequently, tracking the desired strain or controlling the corresponding temperature trajectory is a challenging task. Constant gain controllers result in high errors as the temperature of the SMA wire increases due to increased heat loss and nonlinear dynamics of the SMA actuator. Shameli *et al.* added a cubic term to PID and proposed PID- $P^3$  to reduce the settling time and overshoot of the SMA [74]. For a small error, the cubic term vanishes and the controller works as a regular PID controller. Rahman *et al.* introduced the NPID controller that has a quadratic and a cubic term [75]. When the error is small, the cubic term tends to vanish but the quadratic term still produces a nonlinear control effort.

Heat loss to the environment increases as the temperature of the SMA wire is increased. Thus, at a higher temperature it takes more power to compensate for the same error. It is important to investigate the heat loss and the relation between the supplied power to the SMA wire and the corresponding maximum temperature

that can be reached.

A PWM-based nonlinear PID controller with a feed-forward heat transfer model is proposed to utilize temperature feedback for tracking a desired temperature trajectory. A NPID controller with a feed-forward term given by Equation (3.3) can be used to calculate the required heating time of the SMA actuator.  $\Delta t_h$  is the feed-forward term and it represents the minimum heating time that is required to reach a desired temperature. To find this parameter the relation between the duty cycle of the PWM controller and the corresponding maximum temperature that can be achieved needs to be modeled. The feed-forward term compensates for the heat loss. The integrator is adaptive and depends on the desired temperature of the SMA wire,  $T^d$ , to improve the steady-state response.

$$\Delta t = K_p e + K_D \dot{e} + K_I T^d \int e + K_T (e^2 + e^3) + \Delta t_h \quad (3.3)$$

In Equation (3.3)  $K_p$ ,  $K_D$ ,  $K_I$  and  $K_T$  are the coefficients of the PID controller and  $e$  is defined as the difference between the desired and the current temperature of the SMA wire. Figure 3.1 shows the block diagram of the controller. The blocks that are inside the dashed line were implemented in software. The PWM signal was implemented in the software. The algorithm runs on Windows XP at 500 Hz to obtain high resolution PWM signal.

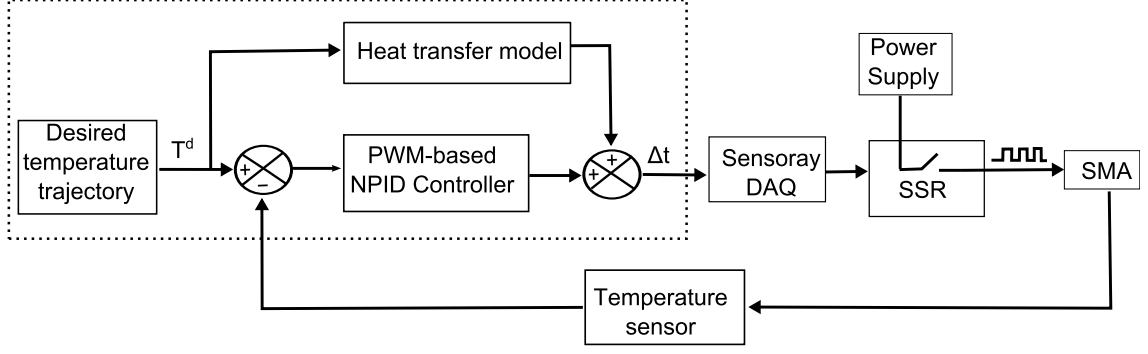


Figure 3.1: The block diagram of the proposed PWM based NPID controller

### 3.3.1 Thermal Modeling

The heat transfer properties of the SMA need to be determined to find the relation between the current supplied to the SMA and the temperature of the SMA. Heat transfer equation of SMA is commonly defined in terms of input power to the SMA, and it depends on the specific heat and the convection coefficient of the SMA [61, 69, 76]. Digital signal calorimetry (DSC) measurement is required to find the specific heat of the SMA. The convection heat transfer coefficient is commonly calculated using the empirical relationship for heat transfer over a horizontal or vertical cylinder based on the configuration of the SMA wire [77–79]. The shape of the arc-shaped SMA actuator changes during phase transformation and a fixed cylindrical geometry assumption cannot be used as in straight SMA wires. Hence, we carry out an empirical approach. Bhattacharyya *et al.* [80] and Senthilkumar *et al.* [81] showed that temperature-current relation of SMA can be represented with an empirical relation:

$$T(t) = T_{\infty} + \frac{a_1}{a_2} IR(1 - e^{-a_2 t}) \quad (3.4)$$

where  $I$  is the current supplied to the SMA,  $R$  is the electrical resistance of the SMA,  $a_1$  and  $a_2$  are the parameters to be determined through experiments. The resistance change of the SMA actuator during phase transformation is less than  $0.1 \Omega$  and it is assumed to be constant. The term  $\frac{1}{a_2}$  is the time constant and  $\frac{a_1}{a_2}IR$  represents the steady-state value. The temperature-current relationship depends on the SMA material used and the dimensions of the SMA actuator. Therefore, the constants  $a_1$  and  $a_2$  are also material dependent. To model the relationship between the temperature and the current supplied to the SMA actuator, different current inputs were applied to the SMA wire. To ensure good thermal contact between the RTD sensor and the SMA wire, a thermally conductive paste is used. Figure 3.2 shows the temperature profiles obtained from the experiments. The parameter  $a_2$  in Equation (3.4) was set to 0.047 and the steady-state temperature values obtained from the experiments were compared to the steady-state term in Equation (3.4). The parameter  $a_1$  can be determined by a linear relation in  $I$  as:

$$a_1 = 49.1I + 18.6 \quad (3.5)$$

PWM has a high energy density. PWM results in a faster response and a higher steady-state temperature compared to continuously supplying the average current value. For instance, a 2A PWM signal with 50% duty cycle results in a faster response and a higher steady-state temperature compared to continuously supplying 1A. Figure 3.3 shows the temperature profiles for different period and heating time values for 2A current. Period values between 50ms - 500ms were tested. A smaller period value may lead to system instability and a high value may result in tem-

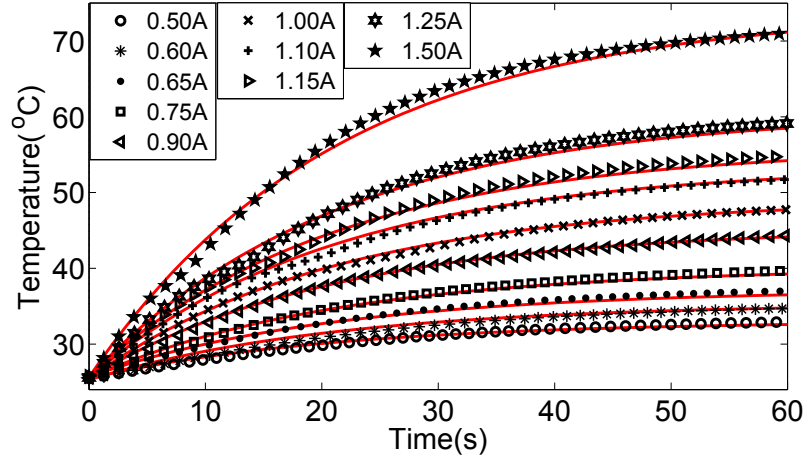


Figure 3.2: Temperature profiles for different current inputs. Solid lines represent the temperature profiles obtained using the empirical model.

perature drop when the current is off. The effect of period,  $P$ , can be neglected in this range and only the duty cycle  $\frac{\Delta t}{P}$  is important. This implies that if more than one SMA wire needs to be actuated, a longer period can be selected to monitor all the wires in the same period. A relation similar to Equation 3.4 can be defined to

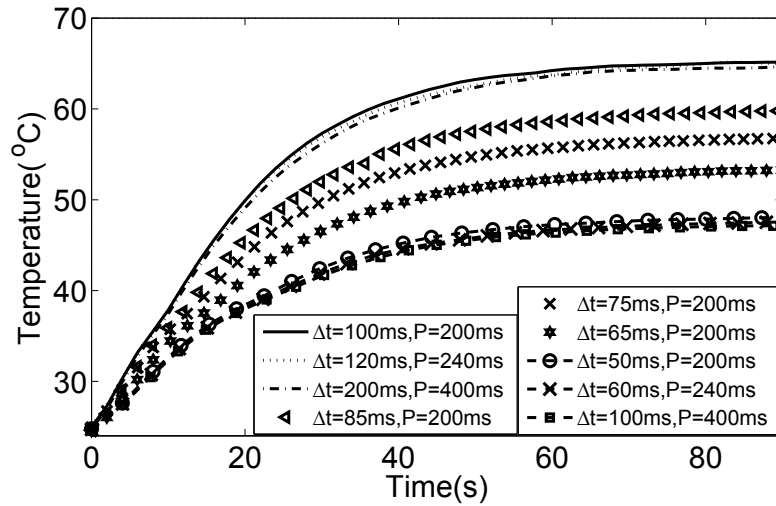


Figure 3.3: Comparison of different pulse widths and duty cycles

obtain the temperature profile using PWM:

$$T(t) = T_{\infty} + \frac{a_1}{a_2} IR \left( \frac{\Delta t}{P} I \right) (1 - e^{-a_2 t}) \quad (3.6)$$

The difference between Equation 3.4 and 3.6 is the addition of the  $(\frac{\Delta t}{P} I)$  term which represents the PWM signal. Figure 3.4 shows the temperature profiles for different current inputs and heating times for  $P=200$  ms. Using  $R=0.35 \Omega$  and setting  $a_2=0.047$ ,  $a_1$  values were obtained by setting the steady state parameter equal to the steady state temperature in each trajectory. Thus,  $a_1$  is given by:

$$a_1 = 7.99e^{-5.417 \frac{\Delta t}{P} I^2} + 3.413e^{-0.112 \frac{\Delta t}{P} I^2} \quad (3.7)$$

A linear relationship can be obtained for  $a_1$  as in Equation (3.5) if a constant current is used. Based on the open loop experiments in Figure 3.4, a relation between the PWM parameter  $(\frac{\Delta t}{P} I^2)$  and the maximum temperature that can be reached is obtained. The maximum temperature increase that can be achieved is defined as  $\Delta T = (T_{ss} - T_{\infty})$  where  $T_{\infty}$  is the ambient temperature and  $T_{ss}$  is the steady state temperature.  $T_{ss}$  values for different PWM input parameters can be obtained from Figure 11. If PWM input parameter is plotted versus  $\Delta T$ , the trend is linear. Figure 3.5 shows the relation between the desired increase in temperature,  $\Delta T$ , and the PWM input parameter. The temperature change is used instead of the final steady-state temperature since the ambient temperature,  $T_{\infty}$ , might be different for each experiment. The linear fit given by Equation (3.8) was obtained from Figure 3.5 and it is used to determine the minimum heating time,  $\Delta t_h$ , that is required to reach the desired temperature. For each sample of the desired temperature trajectory,  $T^d$ ,

$\Delta T$  is calculated by replacing  $T_{ss}$  with  $T^d$ . Then, the corresponding  $\Delta t_h$  is obtained using Equation (3.8).

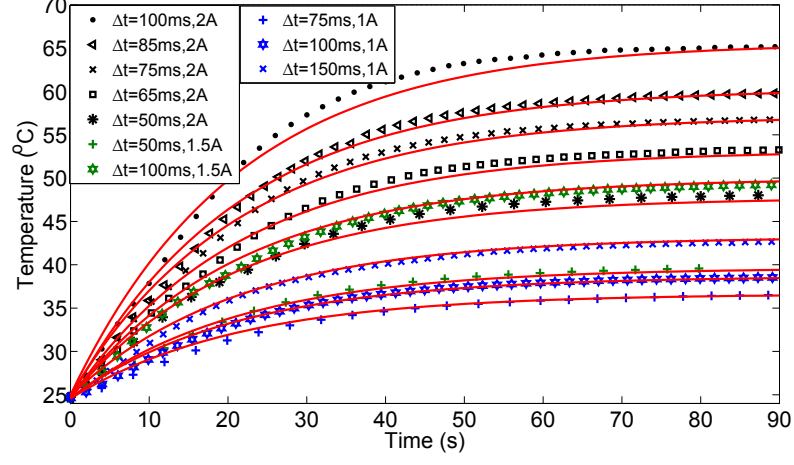


Figure 3.4: Temperature profiles were obtained for different pulse width and current values for  $P=200$  ms. Solid lines represent the temperature profiles obtained using the empirical model.

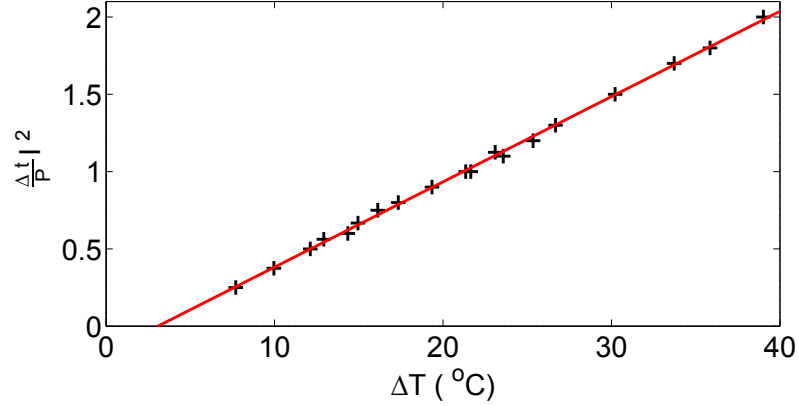


Figure 3.5: Change of the desired temperature increase with the PWM input parameter

$$\left(\frac{\Delta t_h}{P} I^2\right) = 0.05515 \Delta T - 0.16978 \quad (3.8)$$



### 3.3.2 Implementation Of PWM-based NPID Controller

The parameters of the controller were set to  $K_p=55$ ,  $K_D=45000$ ,  $K_I=0.0001T^d$ ,  $K_T=700$ . The following conditions were implemented in the algorithm:

1. Until the temperature of the SMA actuator is within  $1^\circ\text{C}$  of the initial value of the desired temperature trajectory, the integral term ( $K_I(T^d) \int e$ ) is not used.
2. The minimum pulse width is limited by the heat transfer model :  $\Delta t_{min} = \Delta t_h$
3. The maximum pulse width is limited to  $\Delta t_{max} = \Delta t_{min} + 20$
4. Initially, the pulse width calculated using the heat transfer model is used to heat up the actuator until the temperature is within  $2^\circ\text{C}$  of the desired temperature:  $\Delta t = \Delta t_h$  if  $e > 2^\circ\text{C}$
5. The pulse width is set to 0.2 times the minimum pulse width if there is an overshoot (rather than turning the current off):  $\Delta t = 0.2\Delta t_h$  if  $e < 0^\circ\text{C}$

Initially heating the SMA wire with a duty cycle calculated using Equation (3.8) prevents overheating. It also limits the strain rate. A high strain rate causes internal heating and increases the temperature of the SMA wire reducing the reliability of the constitutive model. The quasistatic loading rate can be assumed to be  $0.0005 \text{ s}^{-1}$  [79]. To satisfy quasistatic loading 0.0195 strain (straight configuration to maximum curvature) should be recovered in more than 39 seconds. This corresponds to approximately  $1.6 \text{ }^\circ\text{C s}^{-1}$ . Note that the response time of the SMA actuator can be substantially increased. Fast response is not a crucial requirement for a surgical

procedure and high strain rates corresponds to a quick deformation and tearing of the tissue. Hence, this is not desirable. If a faster response is required, the effect of strain rate on the temperature needs to be taken into account in the constitutive model [79]. The feed-forward term determines the minimum and the maximum heating times for a desired temperature. This is similar to variable structure control [82]. The desired temperature controls the sliding surface and the boundary layer is determined by  $\Delta t_h$ . When the initial value for the desired temperature profile is much higher than the temperature of the SMA wire, the integral term accumulates until the temperature of the wire reaches the desired value. This initial heating period results in overshoot due to large values in the integral term. Therefore, the integral term is not used until the temperature of the SMA actuator reaches the initial value of the temperature profile. The feed-forward term is used to guarantee that the temperature of the SMA actuator reaches within a close range of the desired temperature. When the desired temperature is updated, initially the error is large. Setting a limit to the maximum pulse width limits the initial rate of temperature increase. When the temperature of the SMA actuator exceeds the desired temperature, the current is not shut-off completely. Stopping the current flow results in sudden temperature drop and causes chattering in the control signal [83]. The minimum current supplied to the SMA actuator should be low enough to let the SMA wire cool down but high enough to compensate for the heat loss and prevent sudden temperature drop. The limits for the minimum and maximum pulse width are defined as a function of  $\Delta t_h$  since heat loss increases with increasing temperature. The gains of the NPID controller were selected by trial and error.

To evaluate the performance of the controller a step-wise input was given as a reference. Figure 3.6 shows the performance of the controller in tracking the reference. Figure 3.7 shows the error in temperature tracking. The RMS steady-state error is  $0.0551^{\circ}\text{C}$ . The errors were calculated in the intervals between the time at which SMA actuator reached the desired temperature and the time a new command was sent.

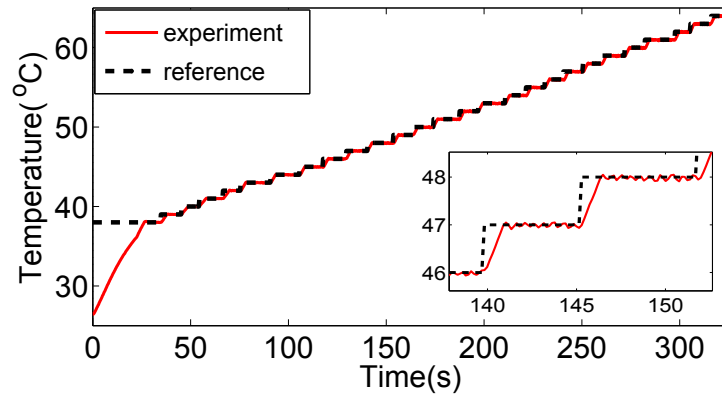


Figure 3.6: Step-wise temperature references and the temperature change of the SMA

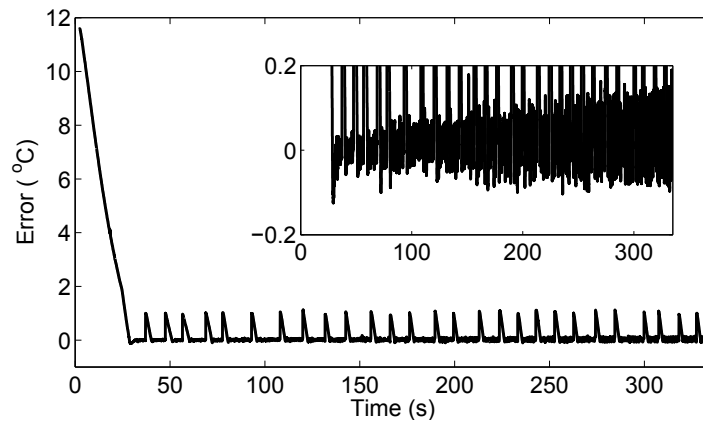


Figure 3.7: Temperature tracking error for the step-wise temperature trajectory

Tracking a continuous trajectory increases the complexity of the system, since the desired path is continuously changing. Tracking of continuous temperature profiles can be achieved by sampling the desired temperature trajectories. Figure 3.8 shows a 6<sup>th</sup> and a 7<sup>th</sup> order polynomial reference. The desired temperature is sampled at 2 second intervals. Phase transformation of SMA is a heat driven process and the response of the SMA actuator is slow. For 1°C increase, the response time of the SMA actuator is approximately 2 seconds. Using a higher sampling rate for the reference signal may be preferable, but it is not required. The RMS errors for the 6<sup>th</sup> and 7<sup>th</sup> order polynomial trajectories are 0.1472°C and 0.1262°C, respectively. The controller shows great performance and it can not only track step inputs but also continuous trajectories.

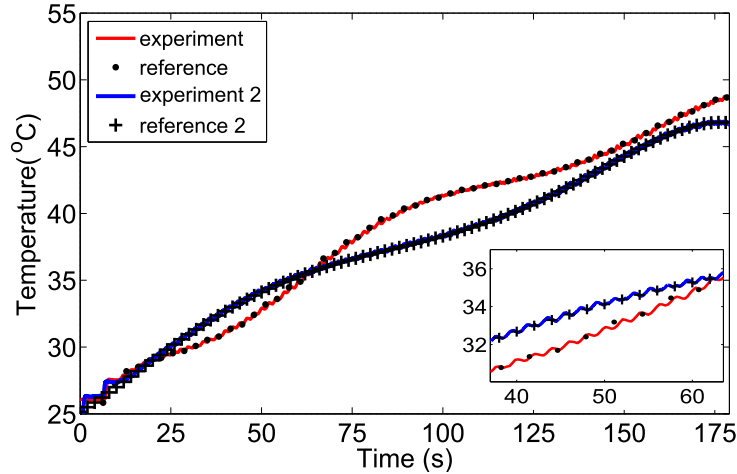


Figure 3.8: Continuous polynomial references and the temperature change of the SMA

Two different experiments were carried out to evaluate the strain using the constitutive model. The experimental setup described in Section 2.4.1 was used to

measure the strain. Figure 3.9 shows a step-wise reference temperature command and the temperature of the SMA actuator. Figure 3.10 shows the change in strain of the SMA actuator and the strain predicted by the constitutive model. A 7<sup>th</sup> order polynomial temperature reference was also applied and Figure 3.11 shows the change of temperature. The change in strain of the SMA actuator is given in Figure 3.12. The RMS errors for the strain trajectories in Figure 3.10 and Figure 3.12 are  $3.4479 \times 10^{-4}$  and  $2.3455 \times 10^{-4}$ , respectively. A continuous temperature profile results in a smooth change in strain and this is essential for accurate trajectory tracking.

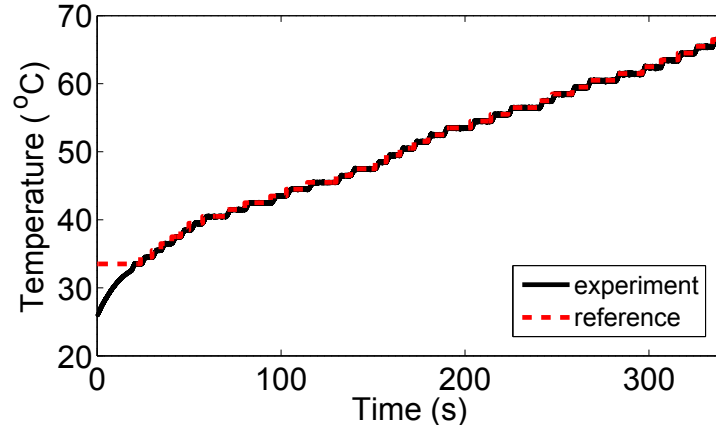


Figure 3.9: Step-wise reference temperature and the change in temperature of the SMA

### 3.4 Summary and Discussions

PWM is an effective method for SMA actuation. A linear or nonlinear compensator can be incorporated into the PWM to develop PWM-based controllers. To control the position of the cannula, a combined image-guided control and a

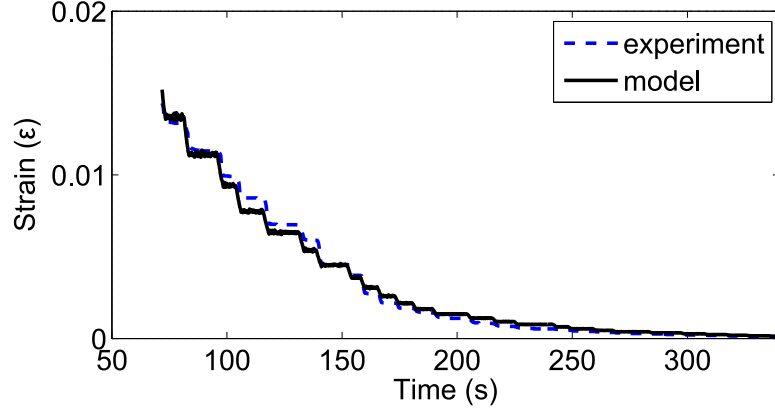


Figure 3.10: The change in strain in the SMA and the strain predicted by the model for a step-wise temperature reference

model-based temperature feedback control was proposed. This chapter discussed a PWM-based NPID controller for temperature feedback and its implementation. A feed-forward heat transfer model was added to the controller to compensate for the heat loss. The results show that the PWM-based NPID controller is effective in tracking complex temperature trajectories which enables using temperature feedback with the constitutive model of the SMA to control the strain of the SMA actuator. The constitutive model of the SMA relates a desired strain trajectory to a corresponding temperature trajectory. Through experiments it was shown that the strain predicted by the model matches with the experimental results. By controlling the temperature of the SMA actuator the change in radius of curvature (thus the strain) can be controlled. Using the proposed controller a desired temperature trajectory can be executed by sampling the temperature values from the desired temperature trajectory. Continuous temperature trajectories can be approximated and smooth strain trajectories can be obtained when the strain rate is limited. In

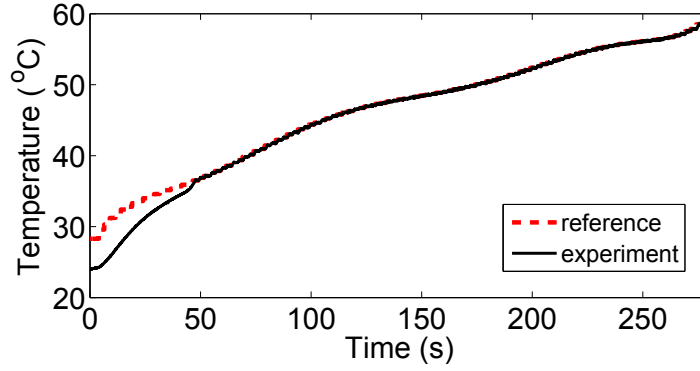


Figure 3.11: A continuous temperature reference and the change in temperature of the SMA

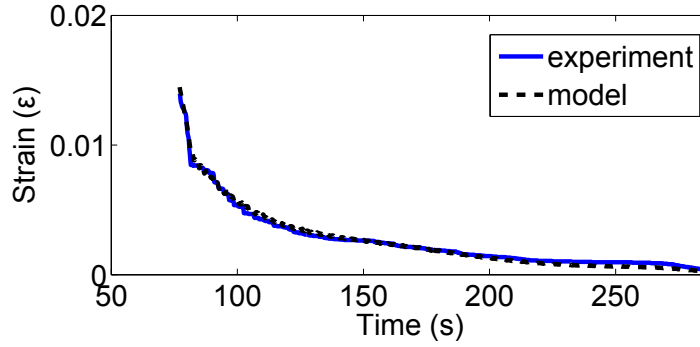


Figure 3.12: The change in strain of the SMA and the strain predicted by the model for a continuous temperature reference

our application, the controller switches to the antagonistic SMA actuator once the actuated SMA wire cools down to the martensite phase. Therefore, the controller is used for the heating phase. This may be a limitation for applications that require fast switching between actuators without waiting for the actuated SMA actuator to cool down to the martensite phase. In the subsequent section, the application of the PWM-based controllers to control the SMA actuators using temperature feedback and image feedback are demonstrated.

## Chapter 4: DISCRETELY ACTUATED STEERABLE CANNULA

This chapter describes the design and development stages of the discretely actuated steerable cannula, and its evaluation through experiments. The steering capability of the cannula was demonstrated in a tissue phantom made of gelatin. An OCT probe was integrated into the cannula for microscale imaging. The results of an OCT imaging experiments demonstrate that the cannula can be used as a delivery mechanism for diagnostic tools. Multiple joint actuation was demonstrated using PWM-based temperature feedback control. A PWM-based motion control method with image feedback was also implemented to execute desired joint angle trajectories.

### 4.1 Prototype I: Steerable Probe with SMA Actuators

The first prototype demonstrates the proof-of-concept of the discretely actuated steerable cannula. The feasibility of using the cannula inside soft-tissue was investigated by an experiment inside a tissue phantom that requires substantial amount of force for steering. There is only one SMA actuator at each joint, and hence the bending is one-directional.



#### 4.1.1 Design of Prototype I

The probe is composed of several discrete segments made of stainless steel connected by a short, flexible and electrically non-conducting annulus. The connecting annulus is flexible but sufficiently rigid (hence semi-flexible) to transmit axial forces along the length and prevent bending due to insertion into soft-tissue. The SMA actuator was attached on the outer surface of the two parts and forms a connection between the two separate pieces of the probe connected by an electrically non-conductive material. The SMA actuators are Flexinol<sup>®</sup> and they were shape-setted in an arc shape. The annealing was done at 520°C for 15-20 minutes followed by forced convective cooling with a fan for 10-15 minutes.

The SMA actuators on the outer surface of the probe enable bending of the probe when the SMA is actuated. Since SMA is used primarily for actuation, it is necessary that the two ends of the SMA wire are not connected to the same metallic component otherwise no actuation will result. Hence, the purpose of the intermediate material (semi-flexible annulus structure shown in Figure 4.1) is to ensure that the SMA actuation will take place and correspondingly result in the bending of the probe locally, which will allow the user to steer the probe to the appropriate target location. Figure 4.2 shows the components on the actual 2-DOF discretely actuated steerable probe controlled via temperature feedback using the thermocouples on the outer surface of the probe along with the SMA actuators. In this design, the outer diameter of the probe is 2.8 mm. Figure 4.3 shows a 2-DOF probe after all the components were assembled.

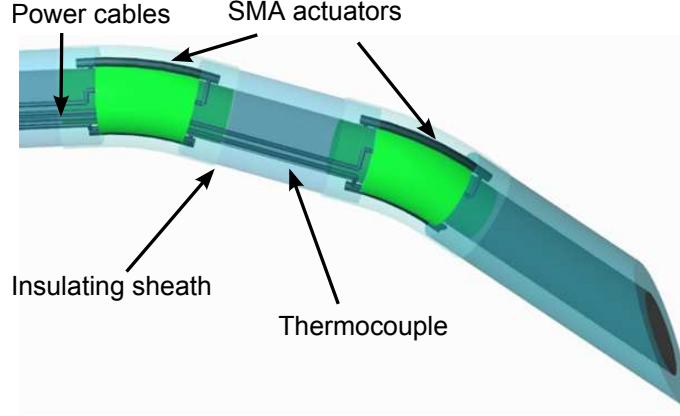


Figure 4.1: Schematic of the discretely actuated steerable probe

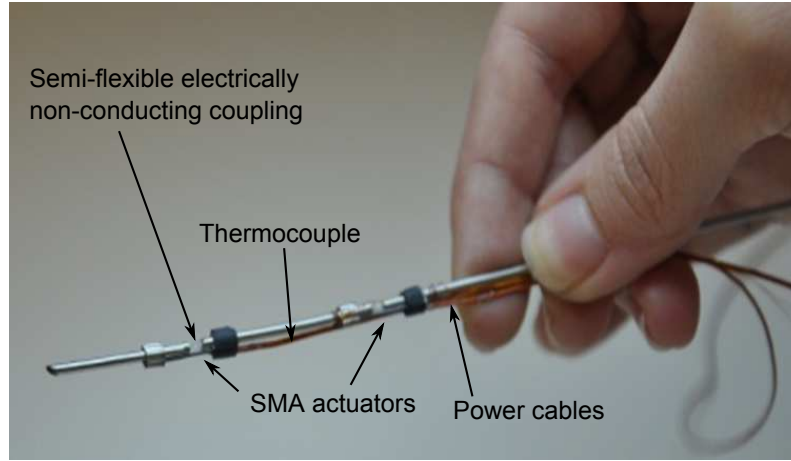


Figure 4.2: Components of the discretely actuated steerable probe

#### 4.1.2 Evaluation of Prototype I

The goals of the experiments presented in this section are to demonstrate the use of PWM based temperature controller for multiple joint actuation and to show that the SMA actuators can generate substantial forces for steering in a tissue phantom. In the first experiment, PWM-P based temperature controller was used to control the temperature of the SMA actuators. The details of the PWM-P tem-



Figure 4.3: An actual 2-DOF discretely actuated steerable probe

perature controller that was used in this experiment is described in [73]. The duty cycle and the period are variable. Both SMA actuators were heated up to  $50^{\circ}\text{C}$ . A 2 A power supply was used to generate the PWM signal. The experiment was stopped after temperature of both joints reached steady state. Figure 4.4 shows the temperature profile and the resulting PWM control inputs. Both wires reached steady state at  $50^{\circ}\text{C}$ . Both joints were successfully actuated using PWM as shown in Figure 4.5. The second experiment was carried out inside gelatin to mimic the motion in soft-tissue. Three packs of Knox Gelatine (Kraft Foods Inc.) were dissolved in a cold water inside a 200 mL cup. Two cups of boiling water were added to the mixture and kept inside the refrigerator until it was fully hardened. Probe was inserted into the gelatin by hand and both SMA wires were simultaneously actuated. PWM-P based temperature control was used to obtain bending along the probe. Figure 4.6 shows the cannula after actuation inside the gelatin. This experiment shows that

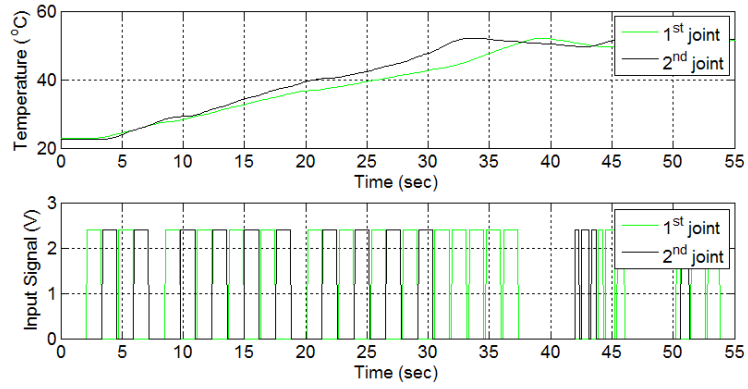


Figure 4.4: Temperature profile and PWM control signal for PWM-P based temperature controller

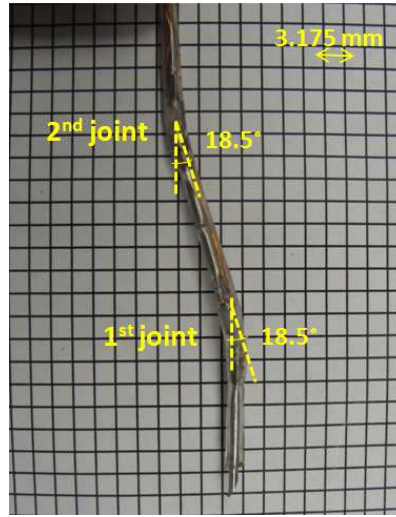


Figure 4.5: Shape of the probe after actuation

SMA wires can generate considerable amount of force to steer inside gelatin. During the experiments it has been noticed that the insulating sheath constrains the SMA during actuation and therefore limits the maximum achievable bending angle.

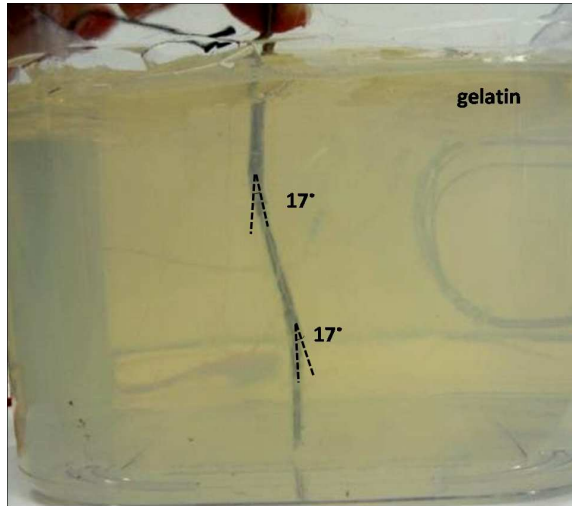


Figure 4.6: Demonstration of the steerable probe actuated in gelatin

## 4.2 Prototype II: Integration of Imaging Window

The discretely actuated steerable cannula can be potentially used to deliver diagnostic and therapeutic tools through the hollow inner core of the cannula. For instance, the cannula can aid in diagnosis with the use of an OCT probe. An imaging window was added to perform microscale imaging with a side-viewing OCT probe. This section has multiple experiments to evaluate the cannula. It was demonstrated that the PWM-based controller can be used with image feedback to control the bending angle. A stereo camera was used for image feedback for demonstration only and in a practical scenario images will be obtained from the imaging modality. PWM-based image feedback was also demonstrated in an experiment inside gelatin.

### 4.2.1 Design of Prototype II

The straight segments have a 1.4 mm inner diameter (ID) and a 1.65 mm outer diameter (OD). The length of each segment from the base to the tip is 6.05 cm, 4.05 cm and 3.05 cm, respectively. There is 1 mm clearance between the adjacent links to prevent short-circuit. The sheath annulus structure and the SMA actuators that join the straight segments are rigid enough to prevent substantial bending during insertion into the soft tissue. The SMA wires were attached mechanically by crimping the wire at the tips via use of stainless steel rings. Enamel-coated wires were wrapped around the tip of the SMA wires for electrical connection. Thermocouples were replaced with resistance temperature detectors (RTD) due to their smaller size. After the assembly, the cannula has 1.4 mm ID and 3 mm overall OD. The prototype is shown in Figure 4.7.

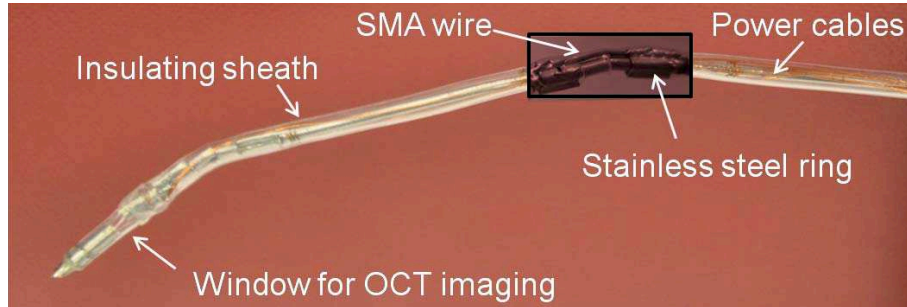


Figure 4.7: The 2-DOF cannula prototype with an imaging window

### 4.2.2 PWM-based Image Feedback Controller

A Micron Tracker camera system (Claron Technologies Inc.) was used for stereo imaging. To find the pose of the cannula, six markers were placed on the

2-DOF prototype. There are two markers on each segment. A tracking algorithm was implemented using a pyramidal Lucas-Kanade optical flow algorithm [84] and OpenCV libraries. OpenCV is a library of programming functions that enable real-time image processing [85]. The optical flow algorithm uses sum-of-squared intensity differences as measurements to minimize the errors for each tracking and works with sub-pixel accuracy [86]. To register the initial configuration, six markers were clicked on the screen via a mouse on the images acquired from the left and right cameras at 15 fps. The 3D locations of the markers were calculated by triangulating the 2D location of the markers on left and right images. The pixel coordinates were then transformed into camera coordinates. A vector was drawn using the location of the two markers on each segment (Figure 4.8) and the bending angle at each joint was calculated by finding the angle,  $\alpha_i$  ( $i = 1, 2$ ), between the vectors drawn on the connected segments.

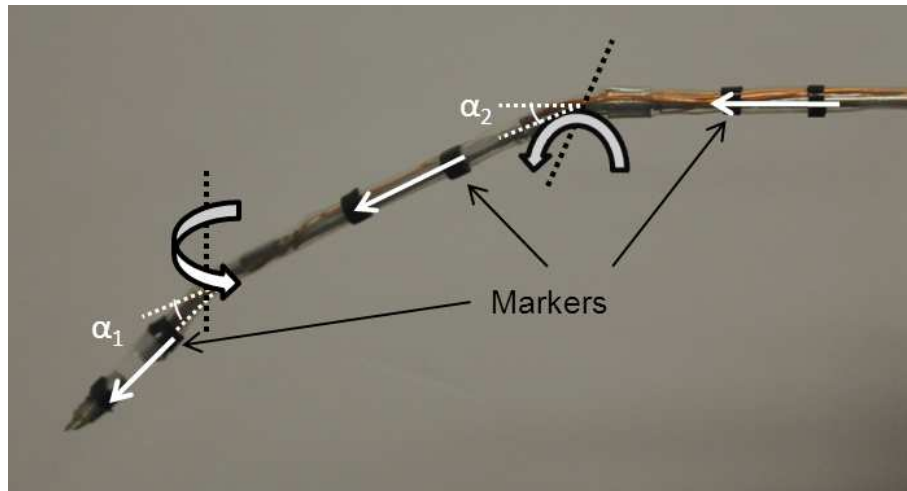


Figure 4.8: Six markers were placed on the cannula for tracking the configuration.

Using the Micron Tracker camera system and the tracking algorithm, the dif-

ference between the desired angle and the current angle were updated at each frame. The position error for the first and second joint were calculated using the stereo image couples and the corresponding heating times  $\Delta t_1$  and  $\Delta t_2$  values were updated. Both links were actuated up to  $11^\circ$ . The period,  $P$ , was chosen as 500 ms and the controller stopped sending control signal when the error was less than  $0.5^\circ$ . The change of bending angle and the corresponding PWM command signal are shown in Figure 4.9 and 4.10, respectively.

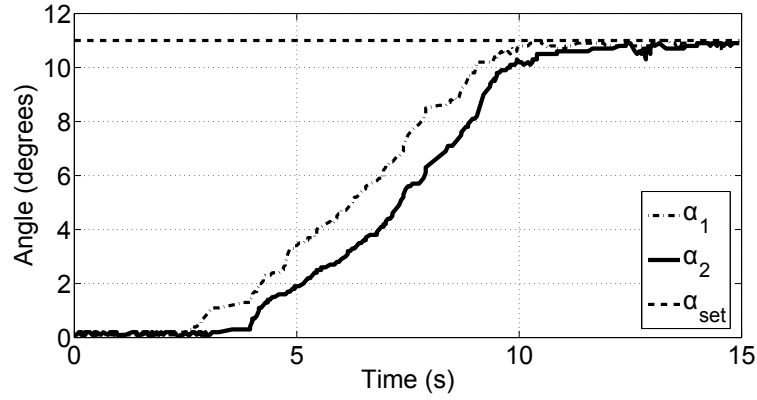


Figure 4.9: Bending angle vs. time for the cannula

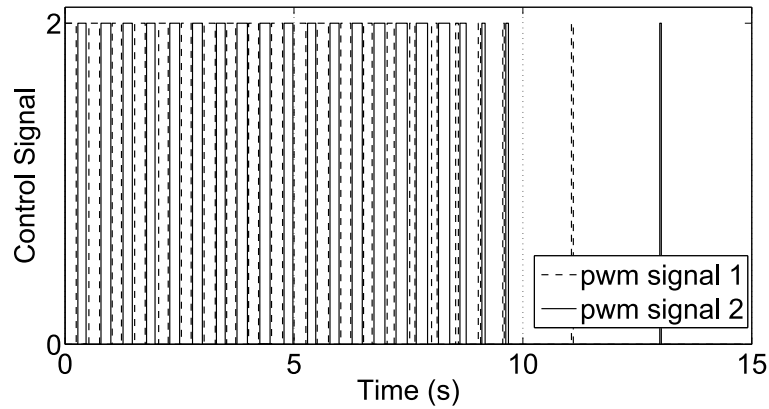


Figure 4.10: PWM command signals for the two SMA wires



### 4.2.3 Testing of the PWM-based Image Feedback Inside Gelatin

The motion of the cannula was evaluated in a phantom of Knox Gelatine using the PWM-P based image feedback controller. Three packets of gelatin were dissolved in cold water inside a 200 ml cup. Two cups of boiling water were added to the mixture, which was kept inside a refrigerator until it was fully hardened. During the experiments, the gelatin was maintained at 15°C. A small hole was drilled on the side of the container and the cannula was clamped between two steel blocks to keep it fixed during the experiment. The controller stopped sending control signals when the error was less than 1°.

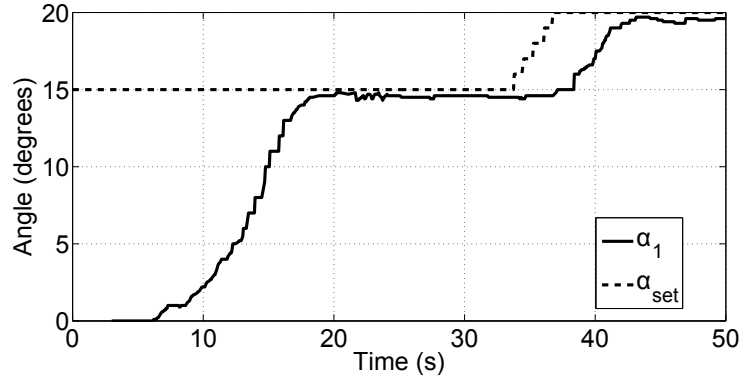


Figure 4.11: Change of bending angle inside translucent gelatin

Initially, the first joint was actuated to 15° and then the desired angle was incremented by 1° up to 20°. The change in bending angle with time is shown in Figure 4.11. The initial actuation took relatively longer compared to actuation in air (Figure 4.9) due to heat loss from the SMA wires to gelatin as the transition temperature of the final SMA wire was substantially higher than the temperature of

the gelatin (15°C). The snapshots from the experiment are shown in Figure 4.12. It is clear from this experiment that the SMA actuator at the joint can exert substantial force to bend inside a medium where a significant force is required to move the medium around.

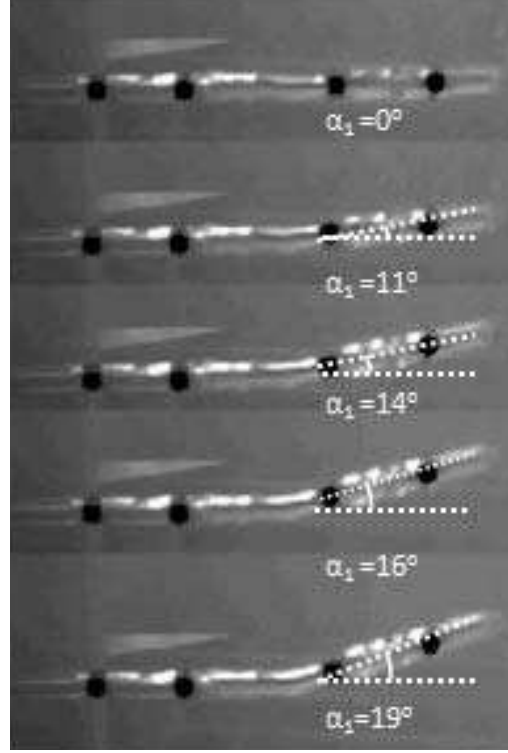


Figure 4.12: The cannula moving inside the gelatin

#### 4.2.4 Strain-Temperature Relationship

PWM-P based temperature feedback controller was used to control the temperature of the SMA actuator. The bending angles were recorded using the stereo camera and the tracking algorithm at different temperatures. The bending angle was mapped to the arc angle using the relation between the bending angle and the arc angle. Arc angle was then converted to the strain of the actuated SMA actuator

using the geometrical relations for bending. The transformation temperatures  $A_s$  and  $A_f$  are 37°C and 68°C, respectively. It was observed that the transformation temperatures of the SMA actuator increases. The transformation temperatures  $A_s$  and  $A_f$  for Flexinol<sup>®</sup> were determined to be 31.5°C and 54°C, respectively. The increase in the phase transformation temperatures  $A_s$  and  $A_f$  are not the same. This shows that the overall external stress generated by the sheath and the crimps increases as the temperature and the bending angle increase. These effects will be explored to model the external stress acting on the SMA actuators accurately.

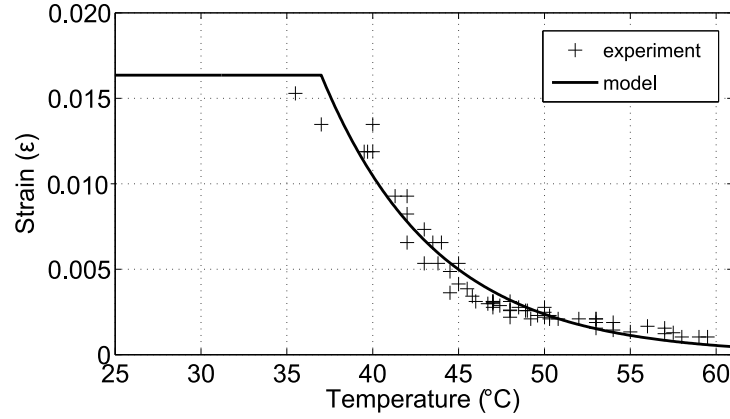


Figure 4.13: Temperature vs. strain relationship of the prototype II

#### 4.2.5 Testing of Maximum Force

To quantify the maximum force that can be generated by the SMA wires, we used the experimental setup in Figure 4.14. The cannula and the force sensor were fixed during the measurements. Thus, the SMA wire was kept at zero strain which enabled us to measure the maximum force exerted,  $F_{block}$ , at the joint. A continuous 1.9 A current was supplied to the SMA wire. All the prototypes we developed in

our laboratory generated a maximum force of between 2.3-2.7 N at each joint.

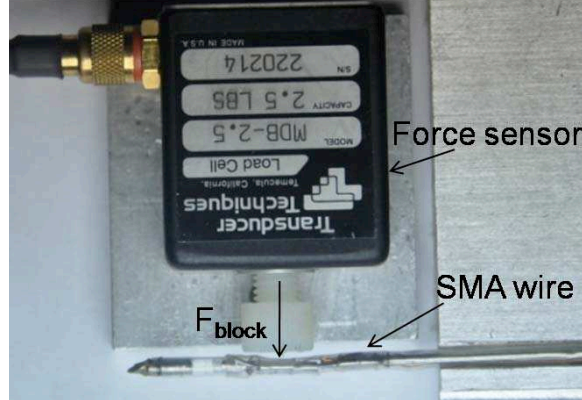


Figure 4.14: The experimental setup used for force measurement

## 4.2.6 Application in Diagnosis

The imaging window and the hollow inner core of the cannula make it a potential guidance tool for a diagnostic application such as optical coherence tomography. To demonstrate the use of the cannula as a delivery mechanism for diagnostic applications, an optical coherence tomography probe was integrated into the cannula and *in-situ* microscale imaging was performed.

### 4.2.6.1 Optical Coherence Tomography Fundamentals

OCT is a new type of optical imaging modality. OCT performs high resolution, cross-sectional tomographic imaging of the internal microstructure in biological tissues by measuring the echo time delay and magnitude of backscattered light [87]. OCT is just like ultrasound where sound waves are sent to the tissue and reflections of sound waves are collected to produce images of the inside of the body. In

ultrasound imaging, sound echoes are measured, while OCT measures the echoes of back-scattered light after passing through a sample. Ultrasound can provide imaging depths of up to around 10 cm, due to the low attenuation of sound waves at frequencies typically used in clinical applications (3MHz - 40MHz). Higher frequencies can be used to achieve higher resolutions, but the attenuation of sound waves at those frequencies is much higher which further limits the imaging depth. Confocal microscopy is an optical imaging method with submicron resolution. The penetration, however, due to optical scattering, is very poor. Optical scattering limits imaging depth to a few hundred microns. OCT has enhanced scatter rejection of out-of-focus light as compared to confocal microscopy. It is based on interference and interferometry principle. It can be in time-domain or spectral-domain. OCT has resolution around 1-15  $\mu\text{m}$  (near that of histopathology) and a penetration depth of around 2-3 mm in biological tissues. For instance, OCT has been shown to provide real-time microscopic images up to 2 mm beneath the tissue surface on excised human breast cancer samples [88, 89], and computational techniques have been proposed to differentiate tissue types [90, 91]. The high-resolution imaging in breast cancer enables detecting tumor margins and finding the local extension of the disease. Furthermore, imaging of tissue can be performed *in situ* and in real-time without the need to remove and process specimens as in histopathology. Since OCT is based on fiber optics, it can be easily incorporated into needles and catheters.

#### 4.2.6.2 Optical Coherence Tomography Imaging Experiments

The feasibility of using the OCT-integrated cannula for tissue imaging was tested on two different biological samples. The aim of the experiments presented in this section is not to quantify the performance of the particular OCT probe, but to verify the imaging capability of the cannula during bending since we are interested in using the cannula to enable *in situ* imaging at the target location. The experimental setup shown in Figure 4.15 consists of the biological sample, a piezoelectric actuator, the OCT probe, the cannula, and a OCT reference arm. The sample arm consists of a fiber-based probe (Figure 4.16). The tip of the OCT probe consists of a gradient-index lens (GRIN) and a micro mirror to deflect the beam. The transverse resolution is 15  $\mu\text{m}$ . The actual OCT probe is shown in Figure 4.17. The OCT interference signal returned from the sample and reference arms was detected by a balanced photo detector and recorded with uniform optical frequency. The OCT probe was actuated at the proximal end by the PZT actuator. The actuator was also synchronized with image acquisition and operated at 14 fps. Discrete Fourier transform (DFT) was performed on the data to produce an axial depth profile of the sample (A-line).

First, the cannula and the OCT system were tested on chicken breast. The OCT probe was inserted into the cannula before insertion into soft tissue. A current of 1.4 A was supplied to the first joint. The same procedure was carried out inside porcine tissue as well. The images were recorded throughout the bending process. Figure 4.18 and Figure 4.19 show the microstructures of the chicken breast

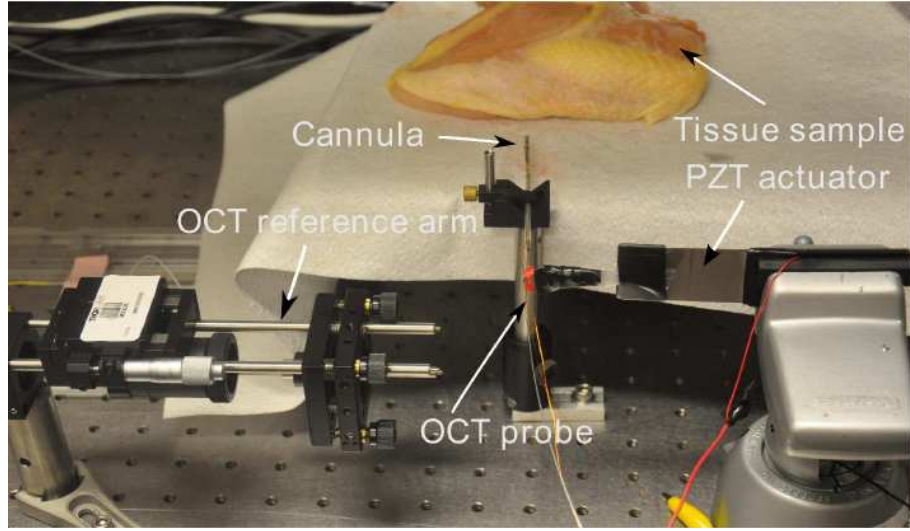


Figure 4.15: Experimental setup for the OCT system

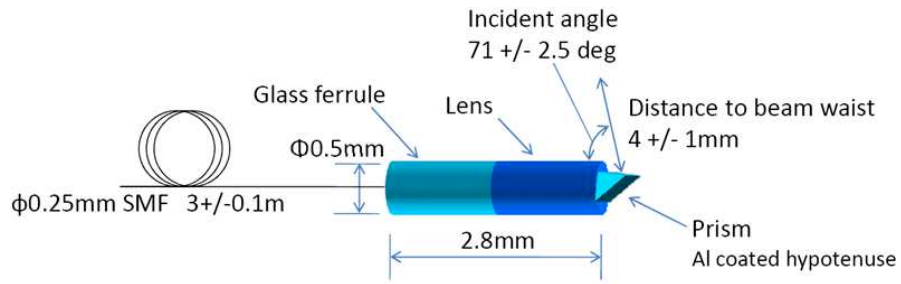


Figure 4.16: Details of the OCT probe

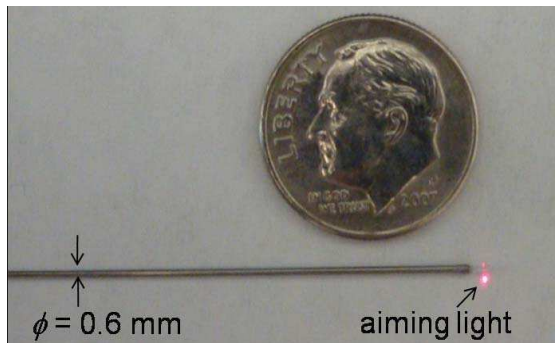


Figure 4.17: The actual OCT probe

and the porcine tissue, respectively. The images are placed with increasing bending angle from left to right, the first one showing the initial OCT image. The images of

connective tissues in porcine tissue and the muscle fibers in chicken breast can be clearly resolved by the imaging system before and during bending. As the bending angle increases, the scanning range of the OCT probe in the imaging window becomes smaller and smaller and finally stops. Figure 4.20 and Figure 4.21 show the histogram of the four images for the chicken breast and porcine tissue OCT images, respectively.

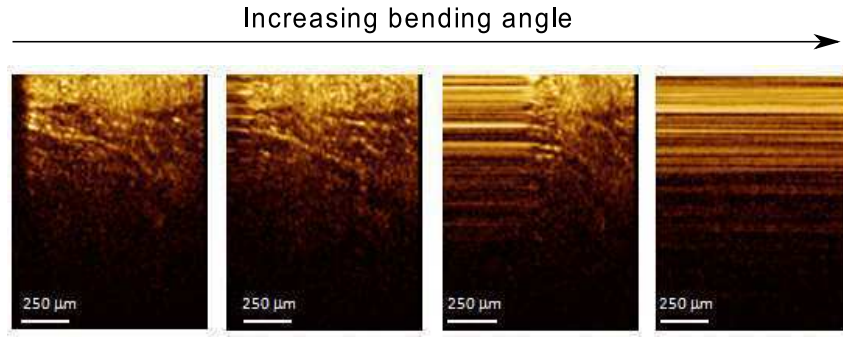


Figure 4.18: Microstructures of the chicken breast

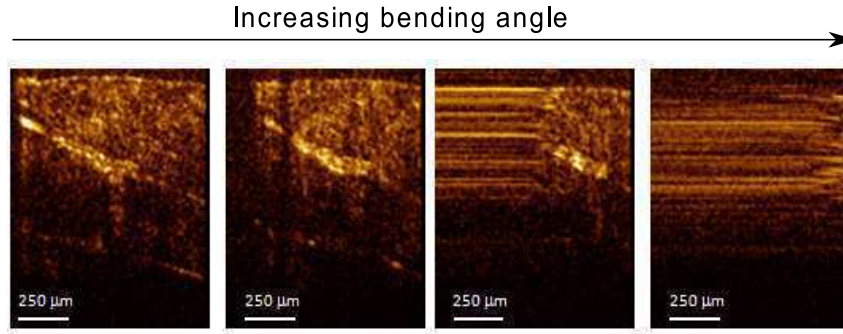


Figure 4.19: Microstructures of the porcine tissue

The images are numbered from 1 to 4 from left to right. The histogram of the images during bending indicates that the images have very similar contrast levels, except the image corresponding to the seized probe (last images). When the probe was stuck, the pixel values at different lateral positions were from the same A-scan



and thus the image appeared as multiple straight lines. These straight lines increase the histogram distribution on the high intensity portion. These results show that the image quality is not affected by the bending of the cannula.

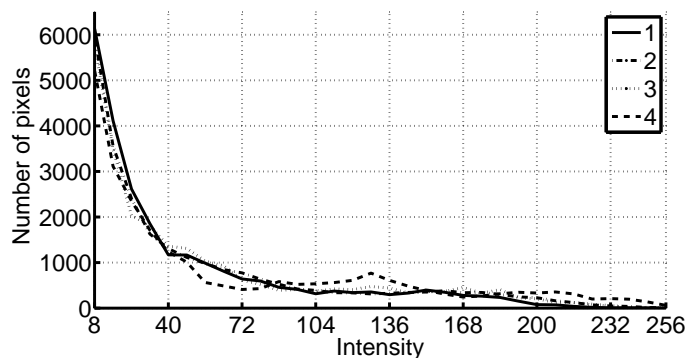


Figure 4.20: Histogram of chicken breast OCT images

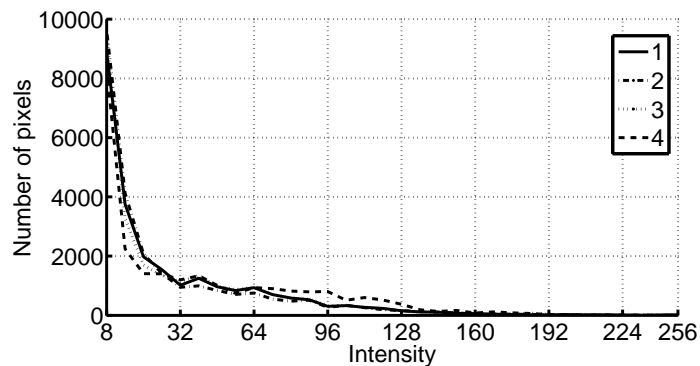


Figure 4.21: Histogram of porcine tissue OCT images

In our initial experiments, we were not able to see the cannula inside the tissue, and we do not have any information about the angle at which the OCT probe contacts the inner wall. In the second part of the experiments, we aimed to quantify the angle at which this contact takes place. The Micron Tracker camera system was used to track the markers on the cannula. OpenCV implementation of

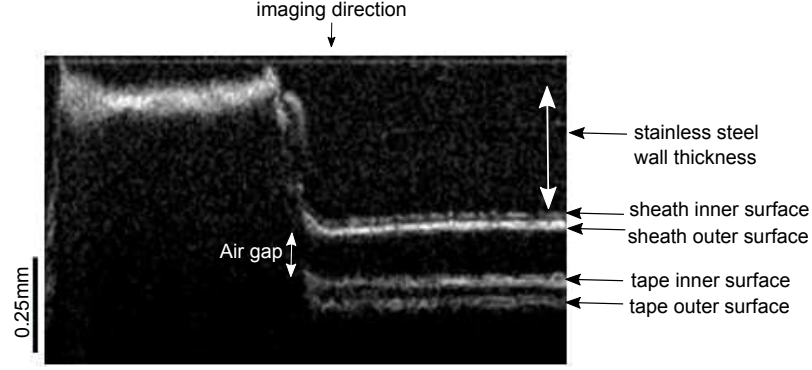


Figure 4.22: The inner wall of the cannula, sheath and tape

the pyramidal Lucas-Kanade optical flow algorithm was used to track the markers on the cannula. The bending angle was recorded during OCT imaging. A tape was wrapped around the imaging window. Since the tape was only wrapped around the imaging window, the markers were clearly detected. This setup enabled us to measure the bending angle at which the scanning range of the OCT probe would start to decrease. The inner wall of the cannula, sheath and tape can be clearly seen in the OCT image (see Figure 4.22). OCT images at various angles are shown in Figure 4.23.

As the bending angle increased, the OCT probe got closer to the inner wall and the decrease in distance between the OCT probe and imaging window at larger angles limits the field of view. The OCT probe contacts the inner wall at  $8.334^\circ$ . The PZT actuator also causes lateral vibration which becomes more apparent when we look at the cannula's inner wall in Figure 4.22. Note that the bending angle of the OCT probe itself is only limited by the nitinol tubing that is used to protect the probe from the environment. The maximum bending angle that can be achieved with the OCT-integrated cannula, can be improved by incorporating a mechanism inside

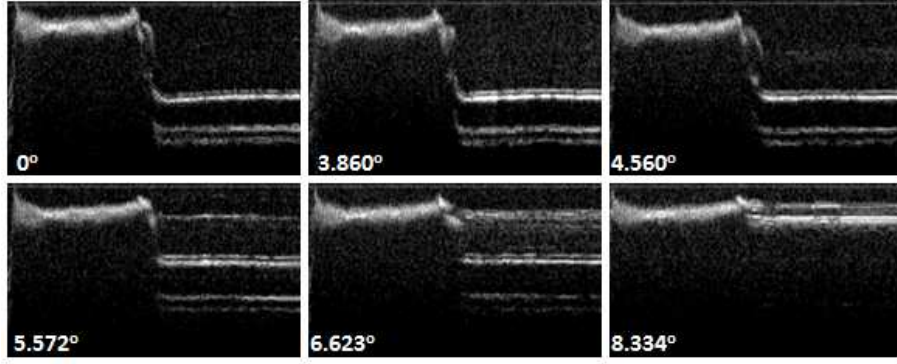


Figure 4.23: OCT images at various angles

the cannula that would hold the OCT probe in place during bending to prevent it from contacting the inner wall. These experiments show that the discretely actuated cannula is a promising guidance tool for OCT.

#### 4.2.7 Discussions on Prototype I and II

There are some limitations of the Prototypes I and II. Since the straight segments are electrically conductive, only one SMA actuator can be used at each joint. Once the SMA actuation is complete, the joint does not go back to the straight configuration. The amount of the recovery depends on the tissue relaxation. A maximum number of three segments can be used in this design due to conductive segments. We connect negative (ground) connections in the middle link and the positive connections on the distal link and the proximal link. The prototypes presented in the subsequent sections overcome these limitations.

### 4.3 Prototype III: Antagonistic SMA Actuators

To overcome the limitation of unidirectional bending, the straight segments should be non-metallic or the SMA actuators should be electrically insulated. One way to isolate the SMA actuators is to coat the metallic tubes with a non-conductive paint. Once the straight segments are electrically insulated, multiple SMA actuators can be placed at each joint thereby enabling joint motion along multiple directions.

#### 4.3.1 Design of Prototype III

Straight segments made of copper with 1.651 mm ID and 3.175 mm OD were painted with high temperature enamel coating (Rust-Oleum, 260°C) for electrical insulation. The length of each section from the base to the tip is 3.81 cm, 3.81 cm and 2.54 cm, respectively. There are four slots along the length of each straight segment and up to four SMA wires can be placed at each joint. The SMA actuator is a 0.53 mm diameter drawn Nitinol (Memry, Inc.) wire that is annealed in a customized shape having an arc-shaped portion and straight portions for attachment. This shape enables us to secure the SMA wire using the straight annealed part and prevent undesirable stress inside the slots, which can degrade the performance at each joint. The effective bending portion of the wire has 1.37 cm radius of curvature (same as in Section 2.4.3.) and its length is determined by the distance between the two consecutive links. In this prototype, the bending angle ranges between  $\pm 21^\circ$ . There is 5 mm clearance between two consecutive links to prevent overconstraining the SMA actuators.

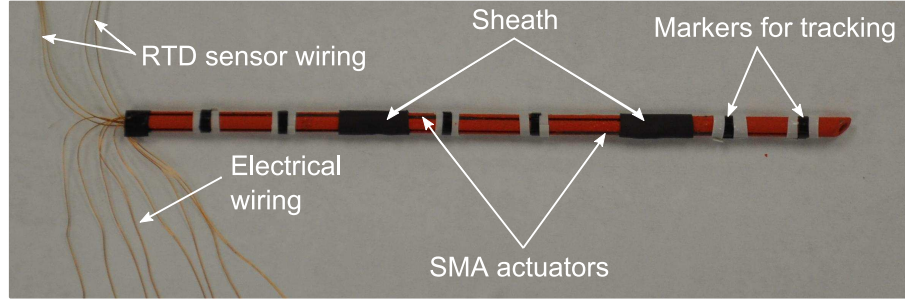


Figure 4.24: At each joint there are two SMA actuators and 1 DOF. The markers were attached on the outer surface for tracking the pose of the cannula.

Initially, both SMA wires were deformed into straight wires for the assembly of the cannula. SMA wires were embedded inside the slots on the outer surface of the links and secured inside the slots via use of a epoxy (Loctite 1324007 Epoxy). The joints were also covered with non-conductive rubber sheath for heat isolation. For electrical connection, enamel coated wires were used and attached on the SMA wire using silver filled conductive epoxy. Mini RTD sensors were used as temperature sensors. RTD sensors were attached to the SMA actuators using a heat shrink tube. The cannula is shown in Figure 4.24. The schematic in Figure 4.25 demonstrates the components of the cannula. The hollow inner core design of the cannula enables the introduction of both diagnostic and therapeutic tools. The cannula was not optimized for a specific application. However, the dimensions of the cannula are scalable and can be adjusted depending on the medical application. Fig. 4.26 demonstrates the antagonistic SMA actuation at each joint. When the actuated SMA wire deforms into an arc shape, the unactuated SMA wire is also naturally deformed.

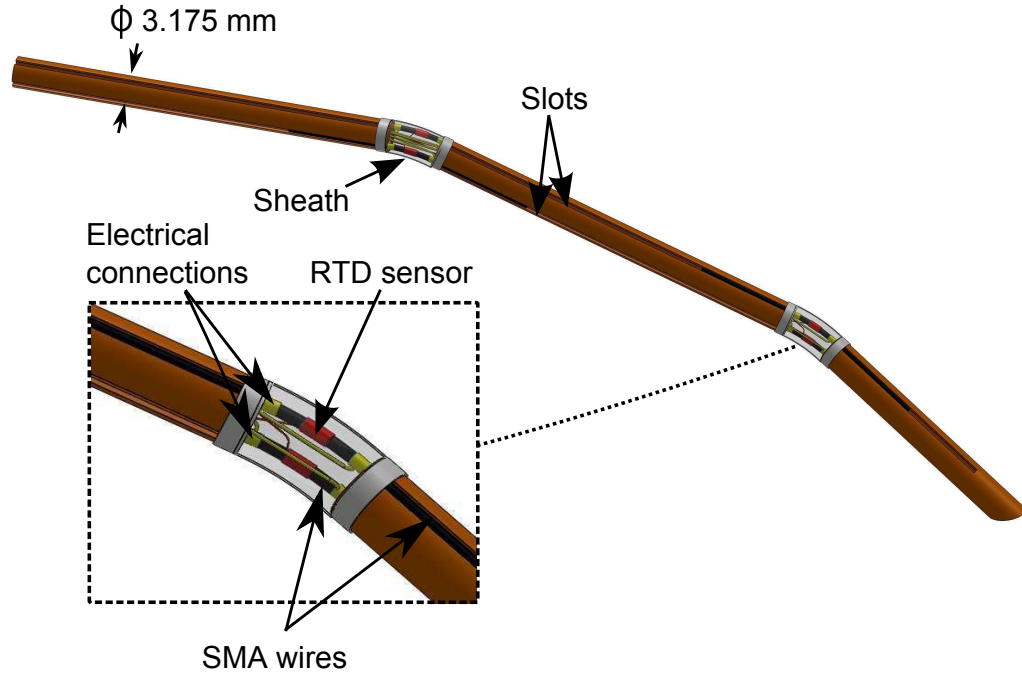


Figure 4.25: Schematic of the discretely actuated steerable cannula

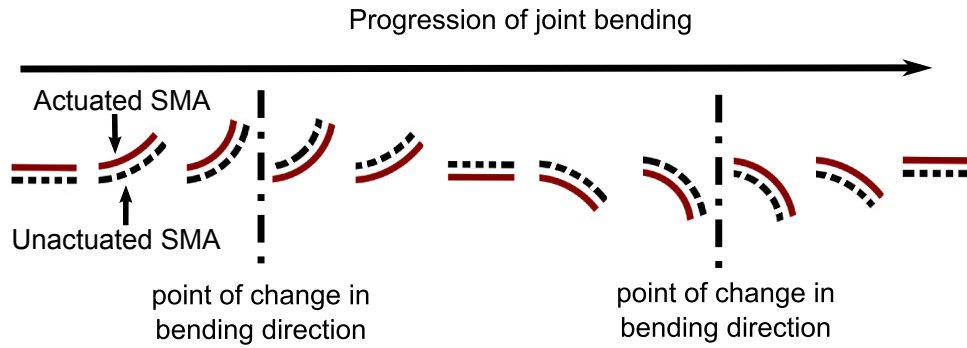


Figure 4.26: Progression of back and forth joint motion - Solid line corresponds to the actuated SMA actuator and dashed line corresponds to the unactuated SMA actuator.

### 4.3.2 Strain-Temperature Relationship

The procedure described in Section 4.2.4 was applied to the prototype III to obtain strain-temperature relationship of the cannula. The joint angle was started

from  $-21^\circ$  and at this position the heated SMA wire has maximum strain. Upon actuation it recovers the strain and reaches maximum joint limit in the positive direction. Figure 4.27 shows the change in strain with temperature.

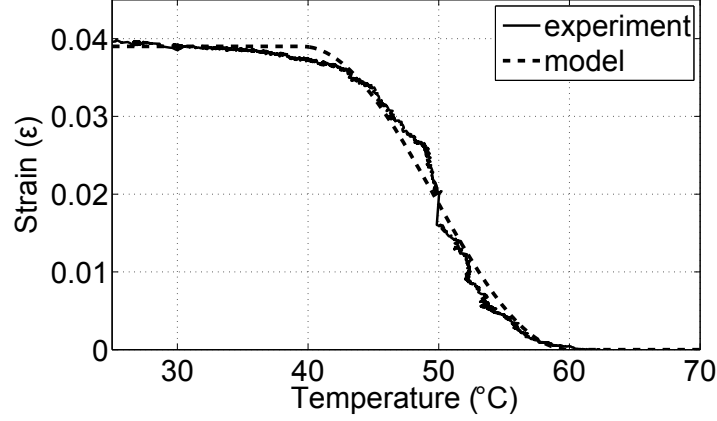


Figure 4.27: Temperature vs. strain relationship for the prototype III

The transformation temperatures  $A_s$  and  $A_f$  of the annealed drawn Nitinol were determined as  $29.5^\circ\text{C}$  and  $58.5^\circ\text{C}$ , respectively. After the assembly, the SMA actuator starts to bend at a higher temperature compared to the bare SMA wire because of the joint constraint and the soft sheath enveloping the joint. The transition temperatures  $A_s$  and  $A_f$  were determined to be  $31.5^\circ\text{C}$  and  $64.5^\circ\text{C}$ . Similar to the results in strain-temperature relationship of prototype II, the shift in transformation temperatures  $A_s$  and  $A_f$  are not the same. The overall external stress generated by the antagonistic SMA wire and the sheath increases as the temperature and the bending angle increase. These effects will be explored to model the external stress acting on the SMA actuators accurately.

### 4.3.3 Discussions on Prototype III

Antagonistic actuators of prototype III are a major improvement over the previous prototypes. Due to the antagonistic configuration of the SMA actuators, the unactuated SMA actuator is naturally deformed by the actuated SMA actuator. To reverse the bending direction, the unactuated SMA actuator (that was deformed naturally by the actuated SMA actuator) can be actuated. Up to four SMA actuators can be placed at each joint. By placing the SMA actuators at parallel planes on consecutive joints 2-D motion can be achieved, whereas placing the SMA actuators at orthogonal planes on consecutive joints enables motion in 3-D. There are two areas that need improvement. The first one is the attachment of the RTD sensor. The RTD sensor is attached to the SMA actuator using heat shrink tubing. The heat shrink tubing envelopes the SMA and the RTD sensor. Its length is much shorter than the length of the effective bending section of the SMA. The RTD sensor sometimes comes off during actuation. Gluing the RTD sensor is not recommended since it would make the sensor dysfunctional. The second area that needs improvement is the coating of the straight segments. Spray-painting the straight segments is messy and covering the entire surface uniformly is difficult.

## 4.4 Prototype IV: Nonmetallic Segments

Using non-metallic segments present challenges due to the limited size of the commercially available tubes and the limited resolution of the rapid prototyping machines (that are available in our university) in producing temperature resistant



tubes for the scale we are interested in. Therefore, polycarbonate rods were drilled at their center to make tubes. Lengths up to 2.5 cm were achieved without any deviation of the center-line. Fig. 4.28 shows the discretely actuated steerable cannula that has three straight segments and two joints.

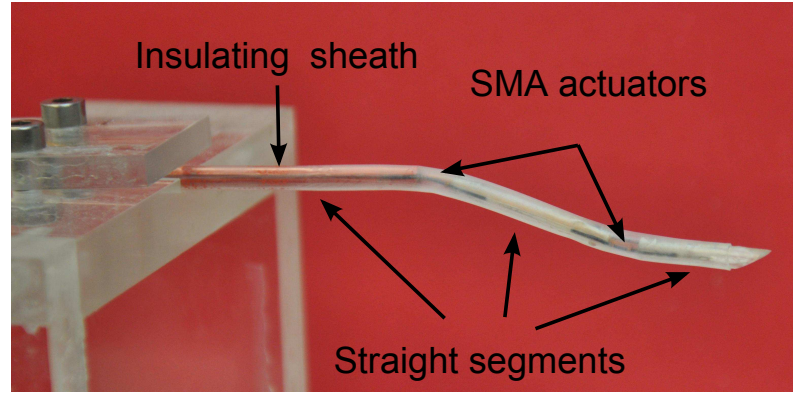


Figure 4.28: Discretely actuated steerable cannula has a pair of antagonistic SMA actuators at each joint.

The straight segments have 1.651 mm inner diameter and 3.175 mm outer diameter. The length of each section from the base to the tip is 3.8 cm, 2.5 cm and 2.1 cm, respectively. The proximal link needs to be longer than the other segments to increase the total cannula length. Hence, it is made of metal and coated with high temperature enamel coating. The remaining straight segments are made of polycarbonate. All SMA actuators lie in a plane and the motion of the cannula occurs in a plane. The cannula was covered with non-conductive sheath for heat isolation and electrical insulation of the SMA actuators.

#### 4.4.1 Pulse-width Modulation-Based Motion Control

The controller described in Section 3.2 was used to control the joint motion of the cannula. In Section 4.2.2, the PWM-based controller with image feedback was used to actuate the joints to a fixed joint angle. Executing a trajectory plan for a needle-based procedure requires controlling joint trajectories. Here, we demonstrate that the joint trajectories can be controlled with the PWM-based PI controller with image feedback. Fig. 4.29 shows the setup used for the experiments.

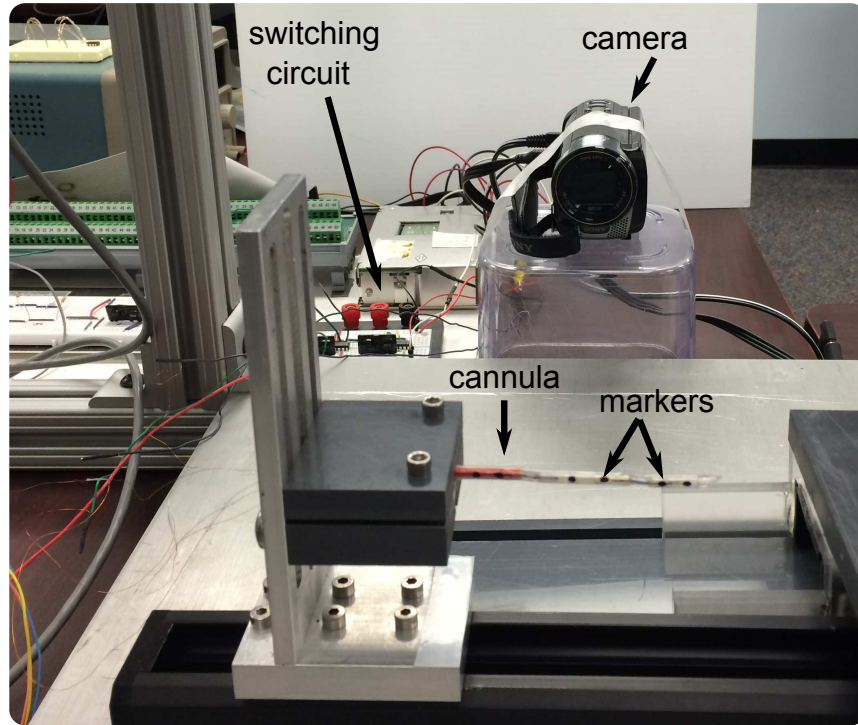


Figure 4.29: Experimental setup used for the tracking experiments.

The SMA actuators have one-way-shape-memory effect. Hence, they can only bend in one direction. When the desired joint trajectory is monotonically increasing or decreasing, one SMA actuator is sufficient to execute the trajectory. To demon-

strate this, two 8<sup>th</sup> degree polynomial trajectories were chosen. The trajectory was sampled at 2 seconds intervals and the desired angle value was given as an input to the PWM-based position controller for the second joint. The PWM heating period,  $P$ , was chosen as 100ms. The gains were chosen as  $K_p = 9$ ,  $K_i = 0.4$ . Fig. 4.30 shows multiple data sets for the two trajectories.

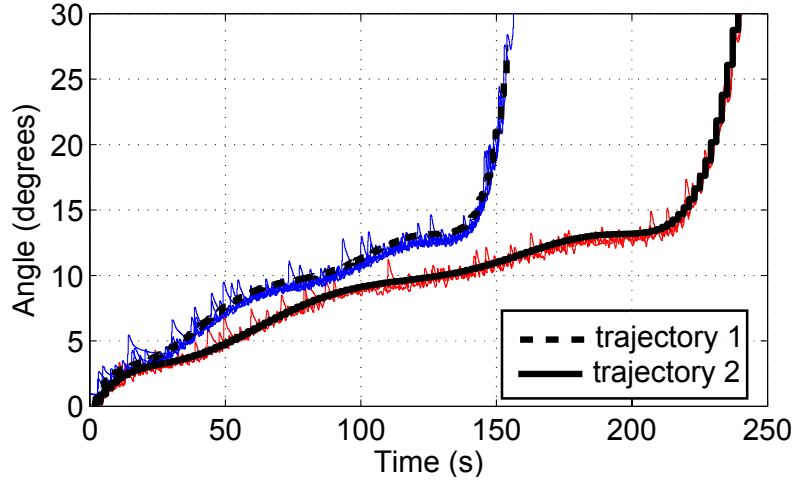


Figure 4.30: Tracking of the joint trajectories using the PWM-based controller. There are 6 datasets for trajectory 1 and 3 datasets for trajectory 2. The average root-mean-square error (RMSE) for trajectory 1 is  $0.6414^\circ$  and RMSE for trajectory 2 is  $0.5816^\circ$ .

The results show that the controller successfully tracks the desired trajectories. However, there is chattering. The PWM signal has high energy density. Even a short period of heating pulse results in a substantial change in the angle. When the current is shut off, it is expected that the angle remains the same as the SMA actuator cools down from the austenite phase. However, the angle decreases slightly when the actuation stops. This behavior is observed during cooling and is known as slack [62].

The antagonistic SMA actuator also acts as a resistance and also contributes to this reverse motion. To improve the performance, both SMA actuators were controlled simultaneously. Fig. 4.31 shows a 8<sup>th</sup> degree polynomial trajectory and the change in angle of the joint. Since both SMA actuators were controlled to compensate for the error, the controller showed better performance compared to single SMA actuation. The controller was also tested on two sinusoidal trajectories as shown in Fig. 4.32. The results demonstrate that PWM-based PI position controller shows good performance in tracking joint trajectories.

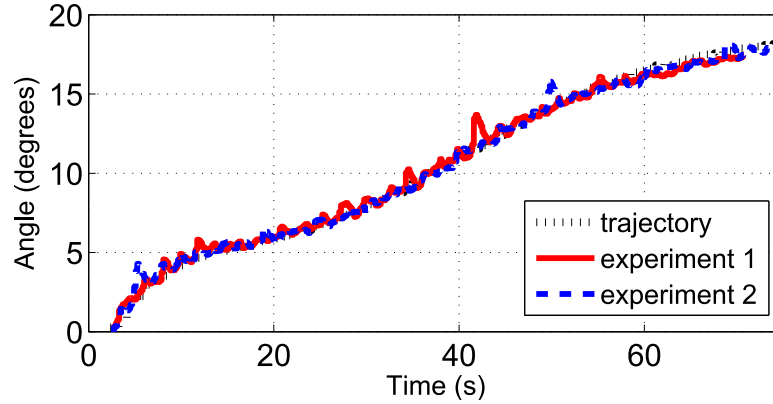


Figure 4.31: Tracking of the joint angle trajectories using PWM-based controller using both SMA actuators. The chattering decreases since both of the SMA actuators compensate for the error. The RMSE for experiment 1 is  $0.4094^\circ$  and RMSE for experiment 2 is  $0.3749^\circ$ .

## 4.5 Prototype V: A Compact Design

An alternative to making slots along the length is to make holes on the cross-section of the straight segments to secure the SMA actuators. Figure 4.33 shows a

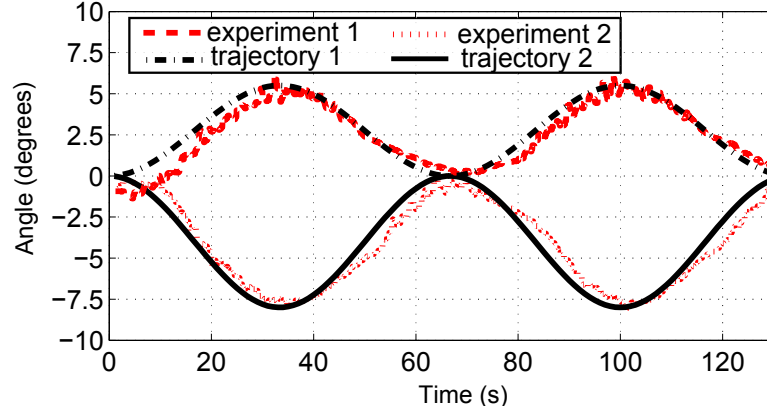


Figure 4.32: Tracking sinusoidal trajectories (Trajectory 1=  $-2.75 \cos(0.03 \pi t) + 2.75$ , Trajectory 2=  $4 \cos(0.03 \pi t) - 4$ ). The RMSE for trajectory 1 is  $0.6753^\circ$  and RMSE for trajectory 2 is  $0.7696^\circ$ .

prototype made of machinable ceramic (Macor<sup>®</sup>). Machinable ceramic is electrically non-conductive and it is easy to machine. Machinable ceramic was originally in a rod form. First, the inner diameter of the straight segments were drilled. SMA actuators were placed inside the holes that were drilled on each side of the inner core. RTD sensors were placed inside the slots that were machined next to the SMA actuators. Since the length of the holes are the same in each straight segment, SMA actuators are also perfectly aligned. For electrical connection, enamel coated wires were used and attached on the SMA wire using silver filled conductive epoxy. This design is more compact compared to the previous prototypes. However, the ceramic segments suffer from surface integrity after drilling and they are not very durable.

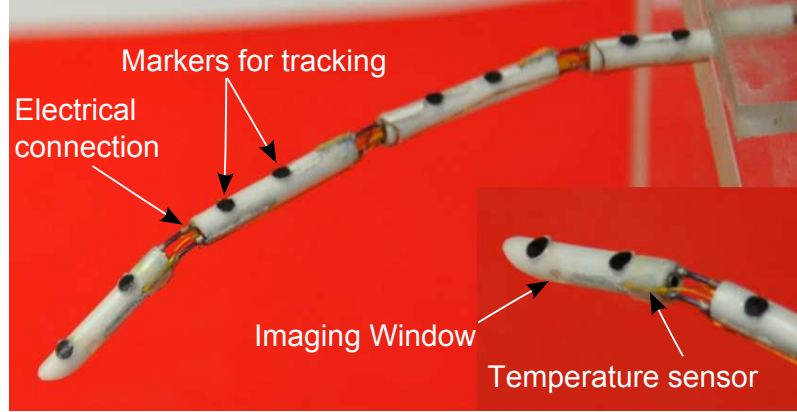


Figure 4.33: Discretely actuated steerable cannula made of machinable ceramic

## 4.6 Summary and Discussions

Five different prototypes have been developed each one building upon another. Prototype I has 2-DOF and one SMA actuator at each joint. An imaging window was added to prototype II to demonstrate the use of the cannula for OCT imaging. Prototype I and II are made of metallic segments which limit the maximum number of joints and the number of SMA actuators that can be used. Prototype III is covered with a non-metallic coating, hence it does not suffer from the limitations of the previous prototypes. Prototype IV is made of polycarbonate segments. It is electrically insulated and does not require any non-conductive coating. Prototype V is made of machinable ceramic and has a more compact design.

The experimental evaluations of this chapter demonstrate that the PWM-based temperature feedback and PWM-based image feedback can be effectively used to control the bending angle at each joint. The controller does not involve any complex hardware or computationally expensive control algorithms. It only uses a single

constant current source and is a powerful approach for controlling the curvature of an arc-shaped SMA actuator. Multiple joints can be actuated simultaneously using the time sharing principle and by actively switching between the SMA actuators. Experiments inside gelatin show that the SMA actuators can generate substantial force to move inside a medium where substantial force is required to move the medium. SMA actuators can be placed such that bending in different directions can be achieved. It is important to note that upon thermal actuation, bending occurs locally at the SMA location (the connection between two consecutive links) which is advantageous for local steering, thereby enabling a small radius of curvature. The hollow inner core of the cannula enables the delivery of other diagnostic and therapeutic tools to the appropriate location. It was demonstrated that the cannula can be used along with an OCT probe to perform microscale imaging.

The strain-temperature relationship of the prototypes show that the transformation temperatures of the SMA actuator in the heating cycle increase due to external stress caused by sheath enveloping the joint, the antagonistic SMA actuator, and the constraints that are used to fix the SMA actuator. The stress acting on the SMA actuators need to be modeled accurately to control the strain of the SMA actuator using temperature feedback.

Fig. 4.34 shows the heat transfer between the actuated and the unactuated SMA actuator at a joint for three prototypes made of different materials. One of the SMA actuator was heated slowly and the temperature was maintained until it stabilized. Hence, the quasistatic condition was satisfied. Since the wall thickness of the straight segments (tubes) is small, there is heat transfer from the

actuated SMA wire to the unactuated one. The heat transfer is minimum for the polycarbonate material. The selection of the material for the straight segments is important for minimizing the heat transfer between the antagonistic SMA actuators.

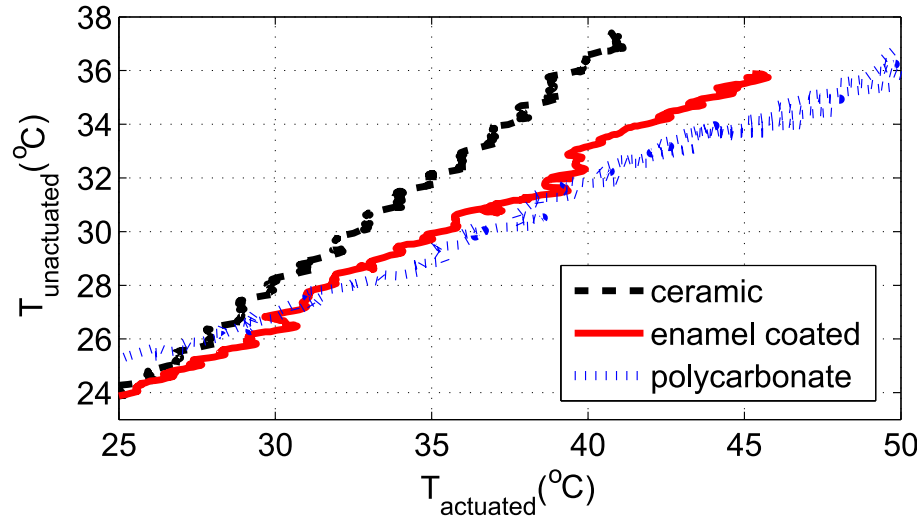


Figure 4.34: Heat transfer between antagonistic SMA actuators for different materials



## Chapter 5: MOTION PLANNING OF DISCRETELY ACTUATED STEERABLE CANNULA

For conventional rigid needles, straight-line trajectories are used to reach a target. The discretely actuated steerable cannula enables trajectories that are not limited to straight trajectories. For a multi-degree-of-freedom cannula, finding a path that satisfies certain constraints and respects the kinematic constraints of the cannula is not trivial. This chapter describes the motion planning for the discretely actuated steerable cannula. In section 5.1, a trajectory planning algorithm that finds the minimum path between two desired set positions is presented. The phase transformation of SMA is a heat driven process, hence it is slow. A trajectory execution scheme is presented that only requires the controlling the position without the need to control the velocity. When multiple constraints need to be satisfied, configuration control is a powerful approach that enables multiple criteria and finds the trajectory that optimizes all the criteria. The configuration control and its implementation are presented in Section 5.2.

## 5.1 Trajectory Planning Using Geodesics

There have been various approaches to the trajectory planning of flexible needles and cannulas in the past decade. Motion planning techniques requiring the minimization of a suitable cost function have been widely used. Additional constraints may be imposed on trajectory planning such as obstacle avoidance and minimum path. Duindam *et al.* discretized the control space of the flexible needles and formulated the optimization problem using a cost function that minimizes the control effort and path length [92]. Park *et al.* applied a numeric diffusion-based method for trajectory planning of flexible needles in an obstacle-free 3D environment [93]. Glozman and Shoham used fluoroscopic images of the tissue before needle insertion to find the location of the obstacle, needle tip, and the target, and through these three points they passed a spline trajectory to find the insertion trajectory [94]. Xu *et al.* used rapidly exploring random trees to find the feasible paths in a configuration space [95]. For flexible needles, finite element modeling has also been used for planning paths around obstacles in deformable tissue [96]. Lyons *et al.* planned trajectories for the active cannula for lung biopsy procedures by using a cost function that depends on the tubular environment geometry [97]. These methods cannot be directly applied to the discretely actuated steerable cannula since these devices are structurally different. The cannula is made of discrete segments and the position of a link is affected by the preceding links that are located closer to the base of the cannula. For the discretely actuated steerable cannula, it is also difficult to control the strain rate (hence the joint velocity) of the SMA actuator. Thus, we followed a

kinematic approach for trajectory planning and execution of the cannula trajectory. Here, we present our approach to generate a minimum path between the desired and final configurations in an obstacle-free environment. Using the notation in [98], the twist coordinate for a revolute joint is defined as:

$$\xi = \begin{bmatrix} -\omega \times q_i \\ \omega_i \end{bmatrix} \quad (5.1)$$

where  $\omega_i \in R^3$  is a unit vector in the direction of the twist axis and  $q_i \in R^3$  is any point on the axis. For a prismatic joint, the twist coordinate is given by:

$$\xi = \begin{bmatrix} v_i \\ 0 \end{bmatrix} \quad (5.2)$$

where  $v_i \in R^3$  is a unit vector pointing in the direction of translation. For the cannula in Figure 5.1:

$$\begin{aligned} q_1 &= [0, 0, 0] , q_2 = [0, 0, l_1] , q_3 = [0, l_1, l_1 + l_2] \\ v_1 &= [0, 0, 1] , \omega_2 = [1, 0, 0] , \omega_3 = [\cos(\beta), \sin(\beta), 0] \end{aligned} \quad (5.3)$$

The forward kinematics map,  $\mathbf{g}_{st}$ , gives the end-effector configuration as a function

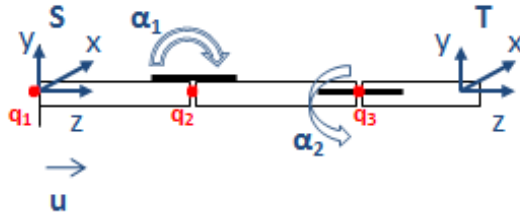


Figure 5.1: The schematic used for the forward kinematics map

of the joint variables and it is defined as:

$$\mathbf{g}_{st} = e^{\hat{\xi}_1 u} e^{\hat{\xi}_2 \alpha_1} e^{\hat{\xi}_3 \alpha_2} g_{st}(0) \quad (5.4)$$

where  $\mathbf{g}_{st}(0)$  is the initial configuration given as:

$$\mathbf{g}_{st}(0) = \begin{bmatrix} \mathbf{I} & \begin{bmatrix} 0 \\ 0 \\ l_1 + l_2 + l_3 \end{bmatrix} \\ 0 & 1 \end{bmatrix} \quad (5.5)$$

The equations were derived for the general case where the SMA at the second joint can be placed at an arbitrary angle  $\beta$  with respect to the first joint. For the prototype described in Section 4.2,  $\beta$  is  $90^\circ$ ;  $l_1, l_2$  and  $l_3$  are 6.05, 4.05 and 3.05 cm respectively.

$\mathbf{g}_{st}$  can be represented as a homogeneous transformation matrix and is given by:

$$\mathbf{g}_{st} = \begin{bmatrix} \mathbf{R} & \mathbf{p} \\ 0 & 1 \end{bmatrix} \quad (5.6)$$

where  $\mathbf{R} \in \text{SO}(3)$  is the orientation of frame T, relative to frame S and  $\mathbf{p} \in R^3$  is the position vector of the origin of frame T from the origin of frame S. The 3D position of the tip,  $\mathbf{p}(\mathbf{q})$ , is given by:

$$\mathbf{p}(\mathbf{q}) = \begin{bmatrix} l_2 s_\beta s_{\alpha_2} \\ -l_2 s_{\alpha_1} - l_3 (s_{\alpha_1} c_{\alpha_2} + c_\beta s_{\alpha_2} c_{\alpha_1}) \\ l_1 + u + l_2 c_{\alpha_1} + l_3 (c_{\alpha_1} c_{\alpha_2} - c_\beta s_{\alpha_1} s_{\alpha_2}) \end{bmatrix} \quad (5.7)$$

where

$$\mathbf{q} = \begin{bmatrix} \alpha_1, & \alpha_2, & u \end{bmatrix}$$

The infinitesimal arc length,  $d\gamma$ , can be written as:

$$d\gamma^2 = \sum g_{ij} dq^i dq^j \quad (5.8)$$

where  $g_{ij}$  are the terms of the symmetric metric tensor, G. Metric tensor is used to define and compute distances on a manifold. The individual terms of the metric tensor, G, are given by:

$$\begin{aligned}
g_{11} &= (l_2 s_{\alpha_1} + l_3 (s_{\alpha_1} c_{\alpha_2} + c_{\beta} s_{\alpha_2} c_{\alpha_1}))^2 \\
&\quad + (l_2 c_{\alpha_1} + l_3 (c_{\alpha_1} c_{\alpha_2} - c_{\beta} s_{\alpha_1} s_{\alpha_2}))^2 \\
g_{12} &= l_3 ((s_{\alpha_2} c_{\alpha_1} + c_{\beta} s_{\alpha_1} c_{\alpha_2})(l_2 s_{\alpha_1} + l_3 (s_{\alpha_1} c_{\alpha_2} + c_{\beta} s_{\alpha_2} c_{\alpha_1})) \\
&\quad - (s_{\alpha_1} s_{\alpha_2} - c_{\beta} c_{\alpha_1} c_{\alpha_2})(l_2 c_{\alpha_1} + l_3 (c_{\alpha_1} c_{\alpha_2} - c_{\beta} s_{\alpha_1} s_{\alpha_2}))) \\
g_{13} &= -l_2 s_{\alpha_1} - l_3 (s_{\alpha_1} c_{\alpha_2} + c_{\beta} s_{\alpha_2} c_{\alpha_1}) \\
g_{22} &= l_3^2 (s_{\beta}^2 c_{\alpha_2}^2 + (s_{\alpha_2} c_{\alpha_1} + c_{\beta} s_{\alpha_1} c_{\alpha_2})^2 + (s_{\alpha_1} s_{\alpha_2} - c_{\beta} c_{\alpha_1} c_{\alpha_2})^2) \\
g_{23} &= -l_3 (s_{\alpha_2} c_{\alpha_1} + c_{\beta} s_{\alpha_1} c_{\alpha_2}) \\
g_{33} &= 1
\end{aligned}$$

In this case, we are interested in finding curves of zero acceleration, namely geodesics on the manifold. The geodesic equation can be written as [99]:

$$\ddot{q}_k + \sum_{i,j} \Gamma_{ij}^k \dot{q}_i \dot{q}_j = 0 \quad (5.9)$$

where  $\Gamma_{ij}^k$  is the *Christoffel symbol* defined in terms of the elements of the metric tensor as:

$$\Gamma_{ij}^k = \frac{1}{2} \sum_l \left[ \frac{\partial g_{il}}{\partial q_j} - \frac{\partial g_{ij}}{\partial q_l} + \frac{\partial g_{lj}}{\partial q_i} \right] g^{lk} \quad (5.10)$$

where  $g^{lk}$  is the entries of the inverse of G. Equation (5.9) produces three second-order differential equations which can be converted into six first-order differential equations. The trajectory for the minimum distance between the desired initial and final configurations can be computed numerically by solving a two-point boundary

value problem. The trajectory is parametrized by  $\eta$ , where  $\eta$  ranges between 0 (initial configuration) and 1 (final configuration). The *bvp4c* function in MATLAB was used to solve the problem. If the boundary conditions are selected as:

$$u_i = 0, \alpha_{1i} = 0^\circ, \alpha_{2i} = 0^\circ \quad (5.11)$$

$$u_f = 0, \alpha_{1f} = 30^\circ, \alpha_{2f} = 20^\circ$$

the resulting motion is shown in Figure 5.2 where the joint angles  $\alpha_1$  and  $\alpha_2$  change linearly with respect to the parameter  $\eta$  from 0-20° and 0-30°, respectively. To

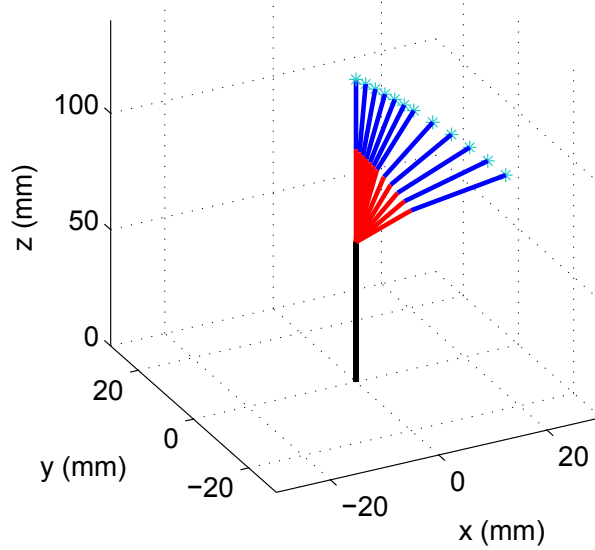


Figure 5.2: Motion in 3D

execute the trajectory-planning scheme, we divide the trajectory into nine intervals by selecting nine data points along the trajectory. We aim to control the position and achieve the desired bending angle at these nine locations along the trajectory. Table 5.1 shows the data points and the desired bending angles.

$\eta$	$\alpha_1$	$\alpha_2$
0.202	6°	4°
0.303	9.5°	6.5°
0.424	13°	8°
0.505	14.8°	9.8°
0.606	18°	11.8°
0.707	20.8°	14°
0.818	24°	16°
0.899	27°	18°
1	30°	20°

Table 5.1: Data points selected along the trajectory and corresponding desired bending angles

$$\eta = \frac{t - t_i}{t_f - t_i}(\eta_f - \eta_i) + \eta_i \quad (5.12)$$

Initially, the angles corresponding to the first data point were entered as the desired bending angles. Once both of the joints reached the desired angles, the angles corresponding to the next data point were entered as the new desired angles. When the markers were along the line that corresponds to bending angles  $\alpha_1 = 0^\circ$  and  $\alpha_2 = 0^\circ$ , we observed that there are variations in the bending angle readings. This is due to the sensitivity of the stereo camera to lighting and the limitations of the tracking algorithm. This makes it difficult to control bending the angles that are close to zero, angles less than  $2^\circ$  in particular. Therefore, a longer interval was

selected for the first interval. Figure 5.3 shows the change of bending angles with time and  $\alpha_{off}$  represents the interval when the new desired inputs were entered. For each interval, the reparametrization between the parameter  $\eta$  and time is given by Equation (5.12), where the subscripts  $i$  and  $f$  represent the starting point of the interval when the desired angles were entered and the final point when both links reached the desired angles of the interval, respectively. The data points showing the desired angles for the intervals and the results of the simulation and experiment are shown in Figure 5.4. The 3D position of the tip of the cannula can be calculated

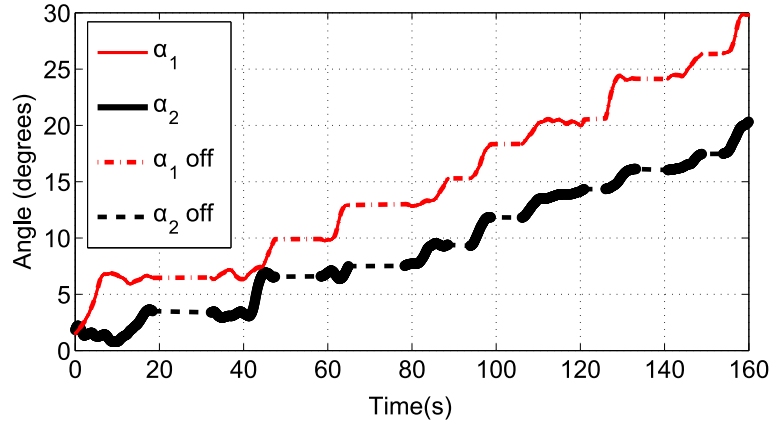


Figure 5.3: The change of joint angles with time

from the forward kinematics map and is given in Figure 5.5. The errors along the trajectory are given in Figure 5.6 and the global error between the final configuration and the target location is 0.29 mm. The maximum error occurs in the first interval due to the fact that this interval is longer than the other intervals and therefore the resolution is smaller for this interval (see Figure 5.6).

The method presented in this section is an effective way to find the optimal trajectory having the minimum distance between two configurations. However, it



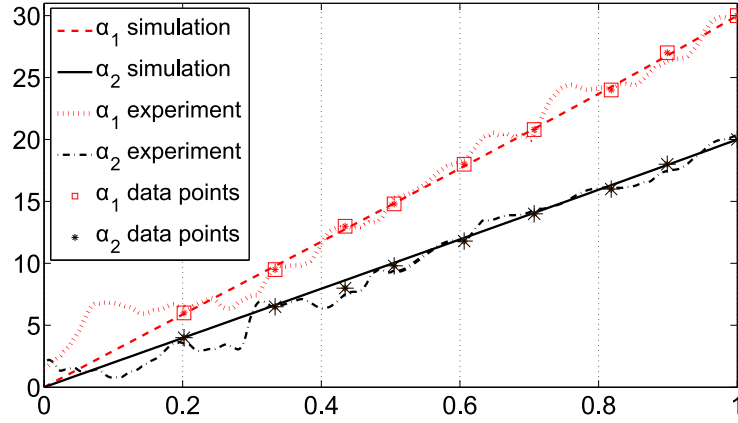


Figure 5.4: The change of joint angles with  $\eta$

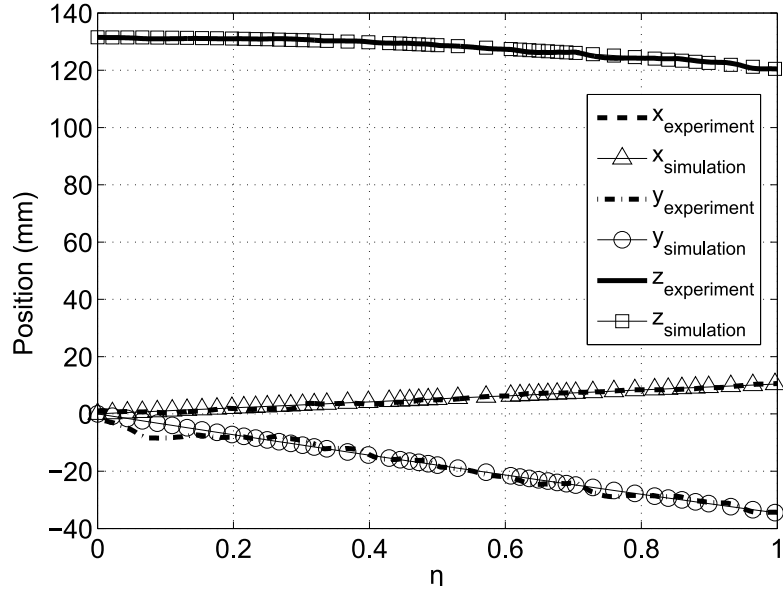


Figure 5.5: The change of 3D position with time

does not guarantee that the generated trajectory can be executed. For instance, the trajectory may exceed the joint limits of the SMA actuator. It is important to steer the cannula to a desired location without exceeding the maximum recoverable strain of the SMA actuators while avoiding anatomical structures defined by the physician in the medical image. Hence, it might be necessary to generate sub-optimal trajec-

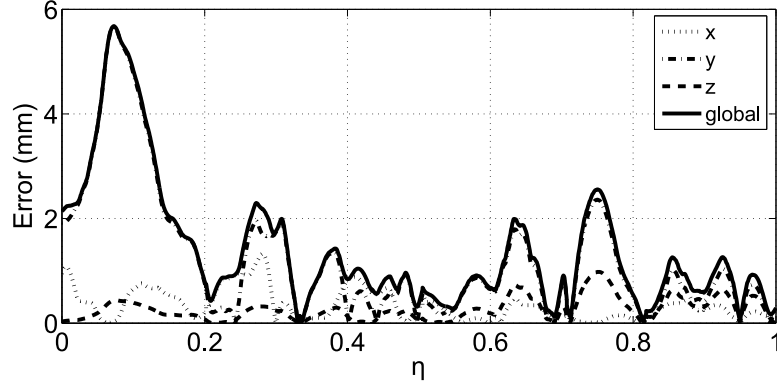


Figure 5.6: Errors along the trajectory

tories for achieving these additional tasks. Configuration control method presented in the following section is advantageous when multiple criteria needs to be satisfied in addition to the minimum distance.

## 5.2 Configuration Control

For the task of reaching a desired position in a 2D plane without any restriction on the tip orientation, a cannula with more than one joint becomes redundant. In general, redundant mechanisms can have infinite number of configurations to achieve a desired workspace specification. The redundant DOF can be utilized to optimize secondary performance criteria without affecting the primary task [100–103]. Configuration control approach developed by Seraji and Colbaugh [104, 105] is an efficient method for redundant robots to achieve the main task of desired end-effector motion while satisfying additional tasks. The proposed controller achieves task space tracking while utilizing the redundancy to impose kinematic and dynamic constraints to avoid joint limits, singularity and obstacles while maintaining posture

control. Using the configuration control approach, the extra degrees-of-freedom of the cannula can be exploited to achieve additional tasks. We intend to utilize the redundancy of the cannula to avoid obstacles and find trajectories without exceeding the maximum achievable curvature of the SMA wire. Finding the maximum bending angle of each joint is not trivial since the maximum recoverable strain of the SMA actuator depends on multiple factors and requires investigation of the constitutive equation of the SMA material. Hence, we explore the variables affecting the joint limit of the SMA actuators and incorporate these variables into the configuration control approach to plan trajectories for the cannula.

A short background on configuration control is briefly discussed here for the sake of completeness. A redundant manipulator has more DOF than the dimension of the workspace. In other words, the dimension of the joint space  $n$  is larger than the dimension of the workspace  $m$ . The cannula is assumed to be inserted from a single point with a fixed orientation and the final orientation of the tip is not important. Therefore, the discretely actuated steerable cannula has 3-DOF: 1-DOF at each joint and 1-DOF along the insertion direction. As a result, the cannula has an additional DOF in a 2D workspace. For a  $n$ -DOF manipulator with  $r$  redundant DOF ( $r = n - m$ ) the optimum joint rates,  $\dot{q}$ , that penalize high joint rates and minimize the error for the main and additional tasks are given by [104]:

$$\dot{q} = (J_m^T W_m J_m + J_a^T W_a J_a + W_s)^{-1} (J_m^T W_m \dot{x} + J_a^T W_a \dot{z}) \quad (5.13)$$

where  $x$  is the main task of reaching the desired position and  $z$  is the additional task.  $J_m(m \times n)$  and  $J_a(r \times n)$  are the Jacobian matrix associated with the main

task and the additional task, respectively.  $W_m(m \times m)$ ,  $W_s(n \times n)$ ,  $W_a(k \times k)$  are positive definite diagonal weighting factors of the main task, singularity avoidance and the additional task. The additional task has no restriction on its dimension. If  $k > r$  the algorithm searches for the best solution that minimizes all the additional tasks depending on their weighting factors. To find the required joint positions to complete the task, we need to integrate the joint rates. First, we assume a path connecting the initial and the final positions with a motion period  $T$ . The simplest assumption is a line segment divided into  $N$  intervals and a planned velocity given by [106]:

$$\dot{x}_k = \gamma \frac{x^d - x_k}{(N + 1 - k)\Delta t}, \Delta t = \frac{T}{N} \quad (5.14)$$

where  $x^d$  is the desired position of the end effector and  $\gamma$  is the deceleration factor greater than 1. Then,  $q$  can be obtained by numerically integrating Equation 5.13.

We consider a 2-DOF planar discretely actuated cannula with 3.81 cm, 3.81 cm and 2.54 cm length sections from the base to the tip. We use a simplified model of the cannula as a serial manipulator in prismatic-revolute-revolute configuration. The joint variables,  $q$ , for the 3-DOF cannula are the insertion distance  $u$  and the bending angle for each joint,  $\alpha_i$  ( $i=1,2$ ).  $\alpha_i$  is defined to be positive in the counter clockwise direction. We will first look into the implementation of the obstacle and singularity avoidance and present the limitations of the configuration control approach by giving examples where these limitations arise.

### 5.2.1 Singularity Avoidance and Obstacle Avoidance

The anatomical structures that needs to be avoided in motion planning can be in various shapes. As an initial approach, we assume convex polygon obstacles. It is assumed that the location of the obstacles are known and continuously updated. The additional task of obstacle avoidance is activated when the minimum distance between a link and the nearest obstacle,  $d_i$ , is smaller than a critical distance,  $r_o$ . The additional task of obstacle avoidance is defined as:

$$z_i = r_o - d_i \quad (5.15)$$

and  $d_i$  is defined as:

$$d_i = \hat{e}_i^T (x_{c_i} - x_o) \quad (5.16)$$

where  $x_o = [x_o^1, x_o^2]^T$  are the coordinates of the closest point on the obstacle to link  $i$ ,  $x_{c_i} = [x_{c_i}^1, x_{c_i}^2]^T$  are the coordinates of the critical point on link  $i$  which has the closest distance to the obstacle and  $\hat{e}_i$  represents the unit vector pointing from  $x_o$  to  $x_{c_i}$  (see Figure 5.7).

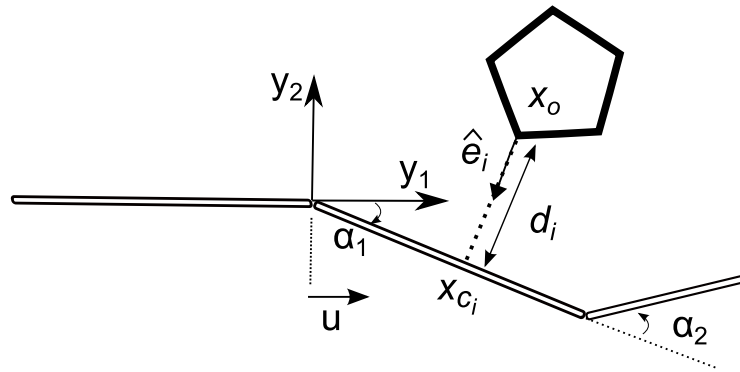


Figure 5.7: The variables used in geometric relations

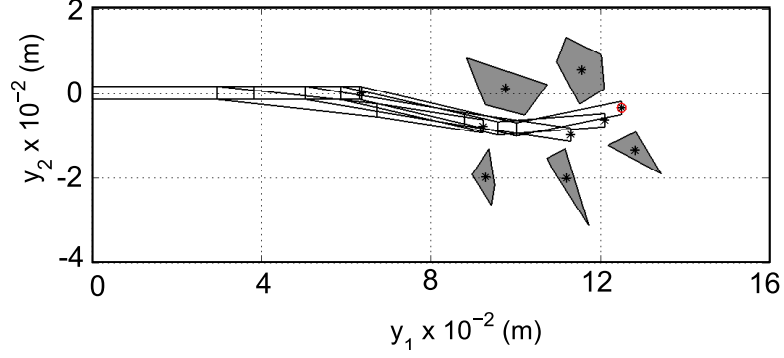


Figure 5.8: Example to illustrate the physical joint limit of the SMA actuator. The obstacles and the final position are inside the workspace of the cannula. However, the maximum joint angle required for trajectory is  $25.0726^\circ$  which is  $4.0726^\circ$  above the physical limit of the SMA actuator.

When  $(d_i < r_o)$  obstacle avoidance task becomes active. The Jacobian for the additional task of obstacle avoidance is given as [107]:

$$J_{a_i} = -\tilde{e}_i^T \frac{\partial x_{c_i}}{\partial q} \quad (5.17)$$

The configuration control is an optimization based approach and if there is a local minima, the motion planning algorithm may fail. Another consideration is the joint limit of the SMA actuator. Even though the obstacles and the target point are inside the workspace of the cannula, the joint limits required for obstacle avoidance may exceed the physical joint limit of the SMA actuator. If there is a local minima, intermediate points can be defined between the initial position and the target position to divide the motion planning problem into sub-problems. Voronoi diagram can be used to define these intermediate points between the initial and the final position. The algorithm was implemented in MATLAB and Figure

5.8 shows an example where the joint limit is exceeded for the SMA actuation in simulation, hence is not physically realizable. We set the parameters  $r_o = 0.07$ ,  $\gamma = 4$  and the diagonal terms of the weighting factors were set to  $W_{mii} = [3, 3]$ ,  $W_{sii} = [0.1, 0.1, 0.1]$ ,  $W_{aui} = [0, 25, 25]$ . The desired position is set to  $[12.5000, -0.3600]$  and the final position achieved by the planner while avoiding obstacles is  $[12.5000, -0.3590]$ . Using Voronoi diagram can prevent the planner from getting stuck at a local minima or hitting an obstacle if the target is right behind the obstacle. On the other hand, avoiding the joint limit is not trivial. The joint limit is not only limited by the physical limits of the actuator (radius of curvature), but there are multiple factors affecting the maximum achievable bending angle. These factors are explored in the following sub-section.

### 5.2.2 Joint Limit Avoidance

The maximum bending angle of each joint is limited by the minimum radius of curvature of the annealed SMA wire. It also depends on the initial strain of the SMA actuators and the stress acting on the SMA actuators (hence the tissue stiffness). The antagonistic SMA actuators at each joint experience different strain levels during trajectory execution. The strain due to bending,  $\epsilon_b$ , can be calculated from the bending angle (arc angle) using the relationship [47]:

$$\epsilon_b = \frac{\alpha d}{2\ell} \quad (5.18)$$

where  $\ell$  and  $d$  are the length and the diameter of the SMA actuator. Note that  $\epsilon_b$  can take negative values and a negative value means the bending takes place in

the opposite direction. The original shape of the SMA wires is an arc with 1.37 cm radius of curvature and this configuration corresponds to zero strain. After the assembly of the cannula, both SMA wires are straight and the strain in both wires is 0.0195 (1.95%). The relationship between the strain of the SMA wire and the bending angle can be found as:

$$\epsilon_{ccw} = 0.0195 - \epsilon_b \quad (5.19)$$

$$\epsilon_{cw} = 0.0195 + \epsilon_b$$

where  $\epsilon_{ccw}$  is the strain of SMA actuator that can bend in positive (counter-clockwise) direction and  $\epsilon_{cw}$  is the strain of the SMA actuator can bend in negative (clockwise) direction. Let us consider the planning problem in Figure 5.9. The desired position and the intermediate point are [10.5000, 1.2000] and [8.6890, 2.1130], respectively. The final position achieved by the planner is [10.4910, 1.2000]. If we look at the change in  $\alpha_2$  for this trajectory, initially the SMA wire that can bend in positive direction is actuated. As it transforms into an arc shape, the bending angle of joint 2 increases up to 0.3352 radians (see Figure 5.10). Hence, the actuated SMA wire recovers 0.0179 strain ( $\epsilon_b = 0.0179, \epsilon_{ccw} = 0.0016$ ) until T=100 whereas the antagonistic SMA wire naturally deforms and its strain increases to 0.0374. After T=100, the bending direction is reversed. For the same bending angle, both SMA wires experience different strain values. Therefore, the strain in the actuated SMA wire should be considered while finding the joint limit.

The material properties and the physical properties of the SMA actuator are given in Table 5.2.  $A_s$  and  $A_f$  values capture the overall effect of the antagonistic



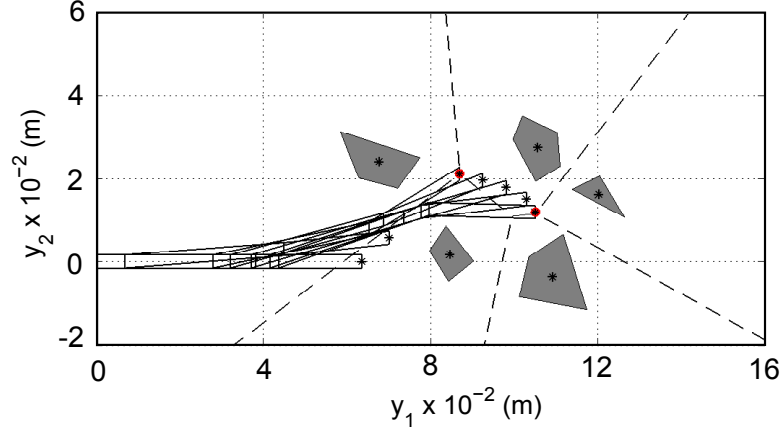


Figure 5.9: Motion planning problem used for analyzing the joint limit

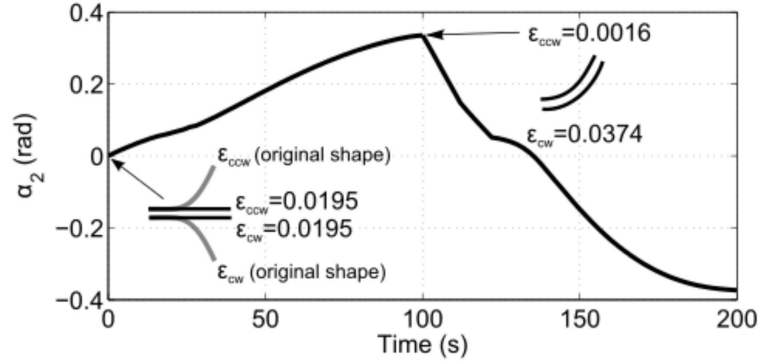


Figure 5.10: Change in  $\alpha_2$  with time for the trajectory shown in Figure 5.9

SMA wire and the sheath on the joints.

If we assume the soft-tissue is linear elastic and model it as a torsional spring with stiffness  $K$  attached at each joint, the external stress acting at each joint during bending can be expressed as:

$$\sigma = \frac{M(d/2)}{I} = \frac{K(\Delta\alpha)(d/2)}{I} = \frac{K(\epsilon_0 - \epsilon)\ell}{I} \quad (5.20)$$

where  $M$  is the bending moment,  $I$  is the area moment of inertia and  $\epsilon_o > \epsilon$  since the strain is recovered during actuation. Substituting Equation (5.20) into

Table 5.2: Material and physical properties of the sma actuator

$E_A$	104.31 GPa	$E_M$	48.69 GPa
$C_a$	30 MPa/°C	$A_s$	31.5°C
$A_f$	64.5°C	$d$	0.5334 mm
$\ell$	5 mm	$r$	1.37 cm

Equation (2.4) results in a nonlinear equation which can be expressed in terms of the stress as:

$$E(\lambda) \left( \frac{\sigma I}{K \ell} \right) + \epsilon_L E(\lambda) (\lambda - \lambda_o) + (\sigma - \sigma_o) = 0 \quad (5.21)$$

From Equation (5.21), the change in external stress,  $\sigma$ , can be found as a function of temperature  $T$ , and these values can be used to find the corresponding strain in the SMA wire using:

$$\epsilon = \frac{\sigma - \sigma_o}{E(\lambda)} + \epsilon_o + \epsilon_L (\lambda - \lambda_o) \quad (5.22)$$

We limit the the maximum temperature of the SMA wire that can be used in motion planning to  $A_f$ . Figure 5.11 shows the change in strain with temperature up to  $A_f$  for different  $K$  values and for different initial strain values. By inspecting Figure 5.11, it can be seen that the maximum recoverable strain (hence the maximum joint angle) depends on the stiffness  $K$  and the initial strain in the SMA wire before actuation. For example if  $K = 4$  N mm/rad,  $\epsilon_o = 0.039$  and the parameters in Table 5.2, at  $T = A_f$  the strain of the SMA wire is  $\epsilon = 0.0042$ . This value corresponds to a maximum bending angle  $\alpha = 0.2868$  rad (16.43°). Given the obstacle and the target locations, it is difficult to know the maximum joint angle that will be required in

trajectory in advance. We make a conservative selection of the joint limit since the maximum joint angle that will be required is not known *a priori* and we assume that the maximum bending angle will be required when a joint starts to bend in one direction. When there is a change in the bending direction, Equation 5.21 and Equation 5.22 are solved to find the new joint limit using the values for the initial strain of the SMA wire that is being actuated and the stiffness  $K$ .

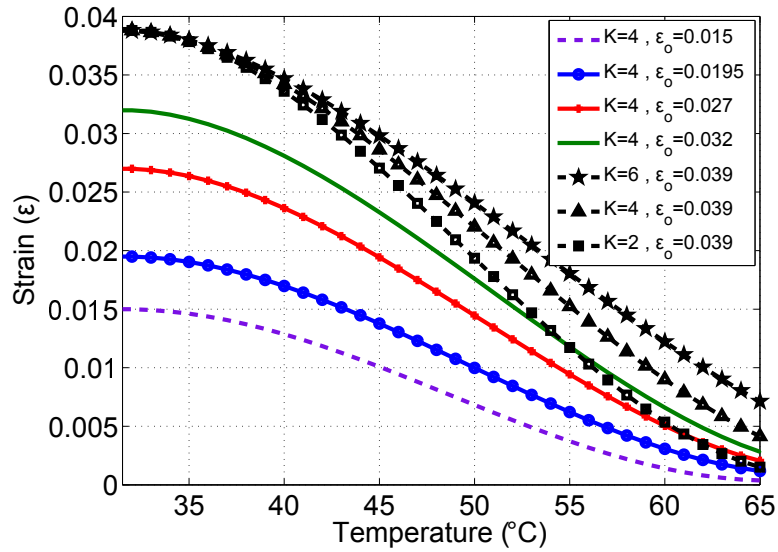


Figure 5.11: The maximum recoverable strain of the SMA actuator depends on the initial strain  $\epsilon_o$  and the stiffness  $K$ .

We can now take this joint limit into account and define the additional task of joint limit avoidance. Additional task for joint limit can be defined as a one-to-one function of the joint variables ( $z = q$ ) and the corresponding Jacobian is given as  $J_j = I_{3 \times 3}$ . Upon reaching the joint limits, the joint rates must disappear. Therefore, the desired joint rates are selected to be zero ( $\dot{z}^d = 0$ ) when the additional task is active. The diagonal entities of weight matrix for the additional task of joint limit

are defined as [104]:

$$W_{jii} = \begin{cases} W_o & q_i < q_i^{min} \\ \frac{W_o}{2} \left[ 1 + \cos\left(\pi\left(\frac{q_i - q_i^{min}}{\tau_i}\right)\right) \right] & q_i^{min} \leq q_i \leq q_i^{min} + \tau_i \\ 0 & q_i^{min} + \tau_i < q_i < q_i^{max} - \tau_i \\ \frac{W_o}{2} \left[ 1 + \cos\left(\pi\left(\frac{q_i^{max} - q_i}{\tau_i}\right)\right) \right] & q_i^{max} - \tau_i \leq q_i \leq q_i^{max} \\ W_o & q_i > q_i^{max} \end{cases} \quad (5.23)$$

$\tau$  defines the buffer region where the weight of the joint limit increases from zero to a maximum value,  $W_o$ . We set the parameters  $\tau = 0.0698$  ( $4^\circ$ ) and the diagonal entities of the weight factor for the additional task of joint limit avoidance as  $W_{jii} = [0, 10, 6]$ . We again consider the trajectory planning problem in Figure 5.9 and assume a stiffness value  $K=10$  N mm/rad. Figure 5.12 show the change in joint variables and the minimum and maximum joint angles for each joint. If we look at the change in joint limits of  $\alpha_2$  with time, initially the joint is straight and the absolute value of the minimum and maximum joint angles are the same since the bending direction is not known. After  $T=100$  s the joint angle starts to decrease and the bending direction is reversed. Here, the joint limit for the SMA wire that can bend in the negative direction should be considered. The joint limit for the positive bending direction remains unchanged until the joint starts to bend in the positive direction again. To give some idea on the stress levels involved for  $K=10$ , let us consider the interval when the bending angle  $\alpha_2$  starts to decrease. The initial joint angle is 0.2551 radians and the maximum joint angle that can be achieved at  $A_f$  is  $-0.1818$  radians. If we ignore the tissue relaxation, initially the stress acting on

the actuated SMA wire is zero. The stress acting on the SMA wire increases from 0 to 293.1 MPa while it recovers the strain from  $\alpha_2=0.2551$  radians to  $\alpha_2=-0.1818$ . Figure 5.13 shows the change in joint variables with time for the cases with and without the additional task of joint limit avoidance. The final position achieved by the planner is  $[10.4990, 1.2920]$  compared to the desired position of  $[10.5000, 1.2000]$ .

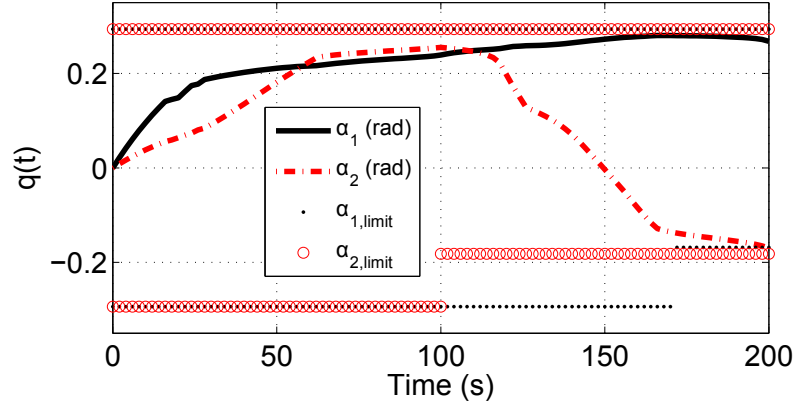


Figure 5.12: Change in joint limits with time

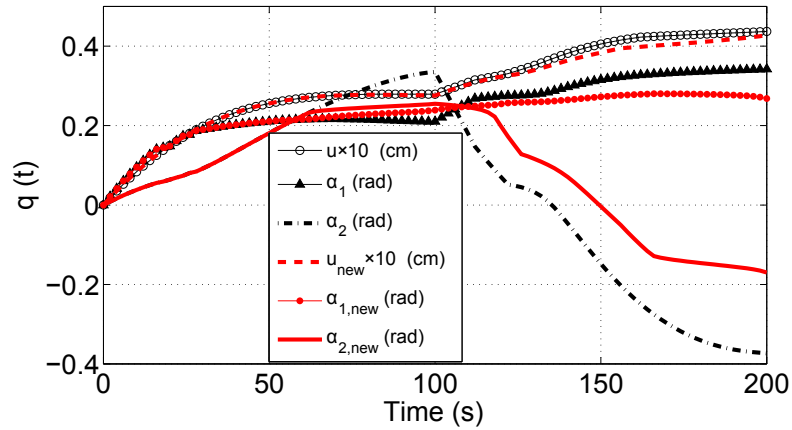


Figure 5.13: Change in joint variables with and without the additional task of joint limit avoidance. The case with joint limit avoidance has the joint variables with subscript *new*.

Table 5.3: Parameters used for motion planning with moving obstacles

	Trajectory A	Trajectory B
Desired Position	[10.5000, 1.2000]	[13.0000, 0.5000]
Final Position	[10.4970, 1.2100]	[13.0000, 0.5000]
$k_1$	[0.02, -0.02]	[0.01, 0.01]
$k_2$	[-0.02, 0.02]	[0.01, -0.02]
$k_3$	[-0.02, 0.00]	[0.01, -0.02]
$k_4$	[-0.02, -0.02]	[0.01, 0.01]
$k_5$	[-0.02, 0.00]	[0.00, -0.01]

### 5.2.3 Moving Obstacles

When the cannula moves inside the soft-tissue, the anatomical structures rarely remain stationary. Presence of other surgical tools that manipulate the tissue can also cause changes in the positions of anatomical structures. Therefore, we test the performance of the planner in the presence of moving obstacles. Figure 5.14 and Figure 5.16 show two motion planning problems with moving obstacles. We set the velocity for the  $i^{\text{th}}$  obstacle as:

$$v_i = k_i(e^{-t/50}) \times 10^{-2}(m/s) \quad (5.24)$$

The coefficients  $k_i$  and the desired position for each problem (Trajectory A and Trajectory B) are given in Table 5.3. With the addition of obstacle avoidance and joint limit avoidance tasks, the final positions achieved by the planner are given in Table 5.3. The change in joint variables with time for the trajectories are given in

Figure 5.15 and Figure 5.17. The algorithm successfully finds a trajectory in the presence of moving obstacles while avoiding obstacles and remaining within joint limits.

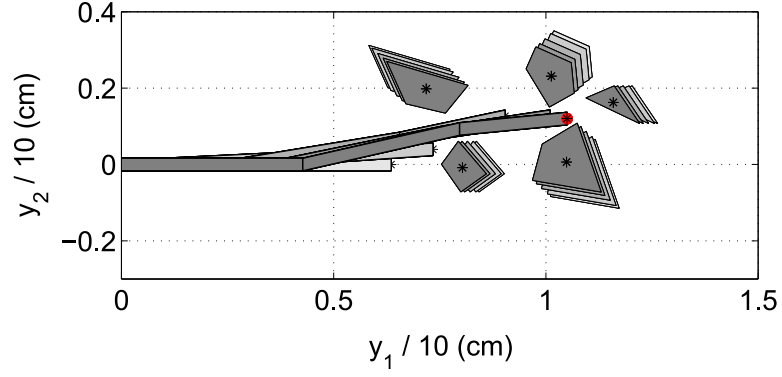


Figure 5.14: Movement of the obstacles and the motion of the cannula in trajectory A. The cannula and the obstacles are shown in a darker color as the time progresses.

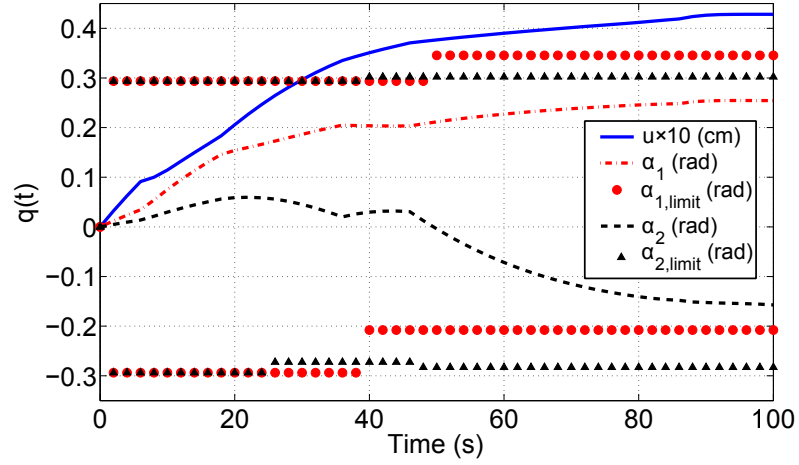


Figure 5.15: Change of joint variables with time for trajectory A

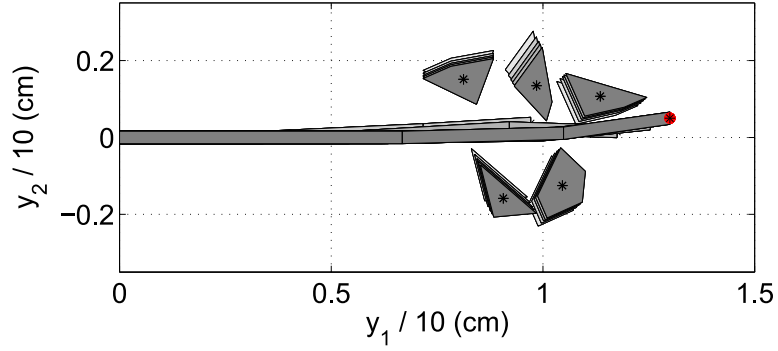


Figure 5.16: Movement of the obstacles and the motion of the cannula in trajectory B. The cannula and the obstacles are shown in a darker color as the time progresses.

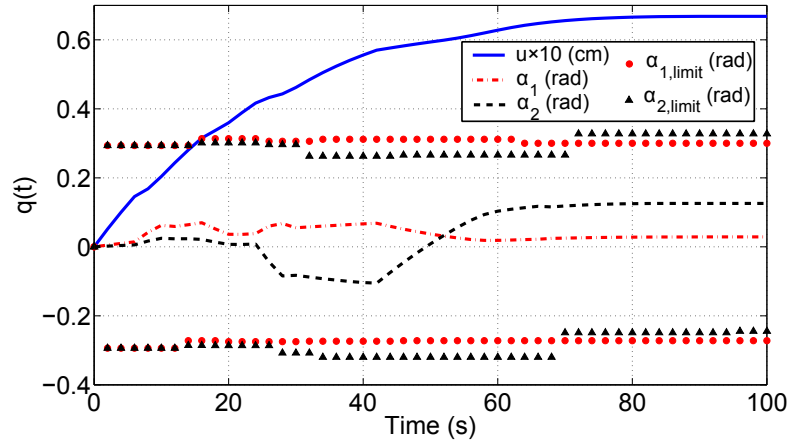


Figure 5.17: Change of joint variables with time for trajectory B

### 5.3 Summary and Discussions

This chapter described two different approaches to generate trajectories for the discretely actuated steerable cannula. In Section 5.1, the trajectory planning was formulated on the configuration manifold. Geodesics on the manifold give the shortest distance between two configurations. The notation used in Section 5.1 provides a coordinate-free representation of the cannula. The algorithm finds the



optimal path. However, it does not guarantee that the generated trajectories can be executed. When multiple criteria such as obstacle avoidance, singularity avoidance and joint limit avoidance need to be satisfied, formulating the problem using the approach in Section 5.1 is challenging.

Configuration control presents an effective yet easily formulated approach to plan sub-optimal trajectories that can satisfy multiple criteria for a robot having redundancy. If the desired position of the cannula is in a 2D plane without any restriction on the tip orientation, a cannula with more than one joint becomes redundant. The cannula was modeled as a PRR mechanism for simplification. This is a valid assumption. For instance, consider Prototype III with  $L_1=3.81$  cm,  $L_2=3.81$  cm,  $L_3=2.54$  cm and  $\ell=5$  mm (arc). We can ignore the arc and model the cannula as a PRR mechanism with segment lengths  $L'_1 = L_1 + \ell/2$ ,  $L'_2 = L_2 + \ell$  and  $L'_3 = L_3 + \ell/2$ . Figure 5.18 shows different cannula configurations for both cases.

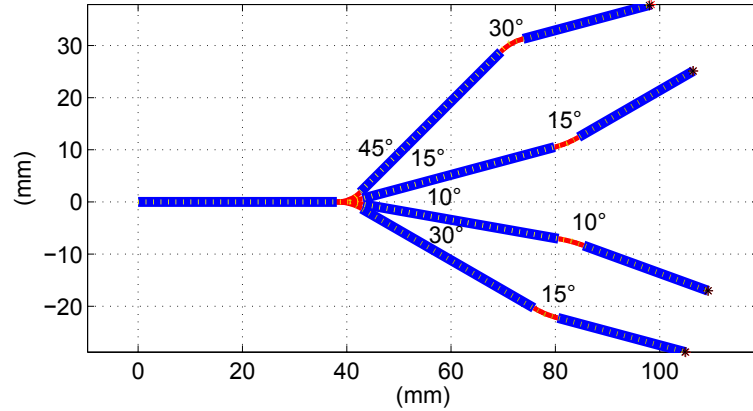


Figure 5.18: PRR kinematics is a valid simplification that can capture the arc-shaped SMA. Dashed lines represent PRR kinematics.

Singularity avoidance, obstacle avoidance and joint limit avoidance tasks were

incorporated into trajectory planning using the configuration control approach. The joint limit of the cannula was modeled by considering the maximum recoverable strain of the SMA actuator using the constitutive model of the SMA. The simulations demonstrate that the maximum recoverable strain (hence the maximum joint angle) depends on the tissue stiffness and the initial strain of the SMA wire that is actuated. We assumed the tissue acts like a linear torsional spring at each joint. More elaborate tissue models are necessary to accurately represent the external stress acting at each joint.

It is important to note that to use the configuration control approach presented in this section, the dimension of the joint space of the cannula should be larger than the dimension of the workspace. Since it is an optimization based approach, the trajectory generated by the planner depends on the weighting factors of each task and the number of tasks to be satisfied. By controlling the weighting factors, task prioritization can be achieved.

## Chapter 6: ULTRASOUND-BASED TRACKING OF DISCRETELY ACTUATED STEERABLE CANNULA

Image-guided interventions have become the standard of care for needle-based procedures. Tracking the needle in real-time through imaging facilitates guiding them inside the soft-tissue and enables automating the needle insertion procedure. The success of the image-guided procedures depends on the ability to precisely locate and track the needle. To actively steer the discretely actuated steerable cannula, we need to develop image processing algorithms that extract information about the needle tip and joint angles. This section presents an in-plane tracking algorithm based on optical flow that obtains the shape of a planar cannula and an out-of-plane detection method that locates the tip of the cannula.

### 6.1 Related Work on Ultrasound Imaging

Ultrasound imaging is inexpensive, portable and free of ionizing radiation. Real-time images can be obtained intraoperatively which makes it attractive for instrument guidance in interventional procedures. In clinics, the localization of the needle is done by an experienced physician. When ultrasound is intended to be used as a feedback to automate the needle insertion procedure, the ultrasound image

needs to be analyzed to obtain quantitative information about the needle shape and configuration.

Image analysis is commonly applied to ultrasound images to reduce noise and obtain useful information about the needle position. Extraction of lines, edges and curves is a key step in image analysis. The Radon transform is a well-known tool for detecting parametrized shapes in an image [108]. Radon transform was previously used to determine parametrized shapes of a curved needle [109]. Hough transform is a special case of the Radon transform and is commonly used to determine line parameters such as slope and intersection points [110]. Hough transform has been used to find the needle long-axis which is usually the brightest line in an ultrasound image [111, 112]. Although needle is usually the dominant line in the ultrasound image, there might be gaps or other line artifacts that belong to other structures. To reduce the noise and detect the tip of the needle, thresholding or morphological operations such as erosion and dilation are applied to the region of interest [113, 114]. There are ways to improve needle visibility and detection. Coating the needles with an echogenic coating such as Echo-Coat<sup>®</sup> (Angiotech Inc.) improves needle visibility. EchoBlock<sup>®</sup> and EchoSti<sup>®</sup> (Havel's Inc.) are commercially available needles that have enhanced visibility compared to generic needles. Wrapping passive markers around the needle tip is another way of enhancing the needle shape in the ultrasound images [112]. However, this approach increases the outer diameter and results in non-uniform cross-section.

For needle tracking, 3D ultrasound imaging is advantageous since it enables 3D visualization of the surgical site. Novotny et al. tracked passive markers that

were wrapped on a needle using 3D ultrasound to obtain needle position [112]. The markers were detected at different positions after imaging for 5 seconds. Adebar and Okamura attached a piezoelectric actuator to the needle shaft outside the tissue to create vibrations that can be detected in the ultrasound images using 3D Doppler ultrasound [115]. An active contour-based detection method was also used to detect a curved instrument and the results were demonstrated in 3D ultrasound images [116]. Previous work on 3D ultrasound primarily focused on detection of the instruments in pre-acquired images [115,116]. The implementation of the algorithms is computationally intensive, requires a GPU processor [109,117], and only a neighborhood of the region of interest is updated to decrease the computation time [112].

2D ultrasound is the current standard that is used in clinics. The images are obtained in slices as opposed to voxels in 3D ultrasound. Hence, it has high acquisition rate and is advantageous for real-time active tracking. When the long axis of the needle is perpendicular to the plane of the ultrasound beam, imaging occurs out-of-plane (Figure 6.1(a)). In out-of-plane tracking, the detected shape is the cross-section of the needle. This approach is mostly used to locate the needle tip [113,114]. This approach is troublesome for active tracking since the geometry of the needle is cylindrical, and each cross-section gives a circle. The ultrasound transducer is usually placed at an angle with respect to the needle insertion direction to visualize the needle tip [118,119] (Figure 6.1(c)). In this case, the detected cross-section can be the needle shaft and the needle tip can be at a greater depth. When the needle long axis and the needle tip lie in the same plane with the ultrasound

beam, the imaging takes place in-plane (Figure 6.1(b)). The in-plane tracking makes guidance easier since the entire needle can be seen. In-plane tracking requires finding geometry specific features of the needle. For a rigid needle, the feature to be detected can be a line whereas detection of local or global curvature may be required for a curved needle.

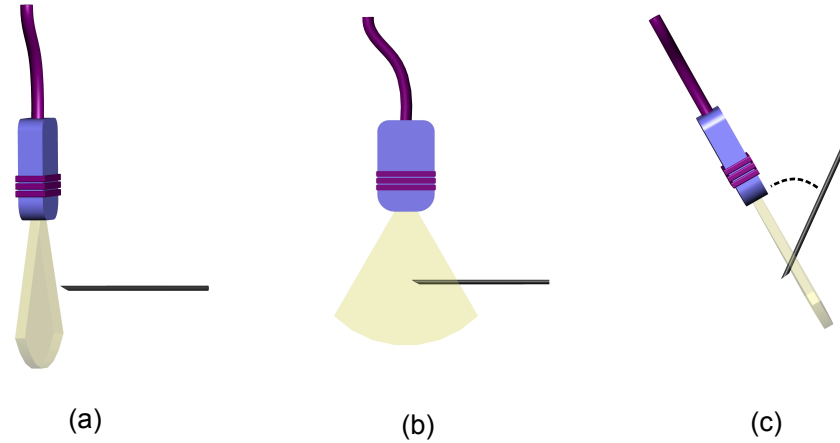


Figure 6.1: Needle and ultrasound transducer configurations: (a) out-of-plane tracking, (b) in-plane tracking, (c) out-of-plane tracking with an angle.

There are a several important considerations in ultrasound-based in-plane and out-of-plane tracking that are often overlooked. In the out-of-plane tracking, the detected shape is the cross-section of the needle. The shaft of the needle can easily be mistaken for the needle tip. The ultrasound beam is commonly assumed to be infinitely thin which adds up to the tracking errors. In reality, the ultrasound beam has a finite width. Hence, the spatial accuracy of needle-tip detection is limited by the ultrasound beam width. The resolution of the ultrasound also needs to be quantified to accurately assess the accuracy of tracking. The spatial accuracy of the

in-plane tracking depends not only on the accuracy of the needle detection algorithm but also on the resolution of the ultrasound transducer. These issues need to be addressed and quantified for accurate in-plane and out-of-plane tracking.

In ultrasound imaging, artifacts of the needle result in missing boundaries. Even when the boundaries are clearly resolved, extracting the boundaries of the needle is not sufficient for tracking. Independent of which algorithm is used, there still has to be a post-processing step to extract quantitative information on the configuration of the needle. For instance, Hough line transform may work well in situations where there is only a single bright line. Despite the missing boundaries, the line parameters can be obtained when a portion of the line is detected. However, it would fail for the cases where there are multiple links. Since the goal is to find the slope between the links, one cannot specify a desired slope to eliminate the other lines. Hence, for real-time guidance of the needle, the performance of the tracking method used does not only depend on detecting the needle boundaries, but also depends on effectively getting quantitative information that describes the needle configuration. In this work, needle detection and quantitative information are obtained simultaneously.

The in-plane tracking gives information about the configuration of the cannula and can be used as feedback to control the motion of the cannula. Out-of-plane tip detection is achieved by rotating the ultrasound transducer until ultrasound beam is perpendicular to the needle long axis and then scanning the cannula tip to detect the exact location of the cannula tip. This way any out-of-plane motion can be easily detected. The out-of-plane tracking method proposed here does not suffer

from the infinitely thin ultrasound beam-width assumption and guarantees that the detected shape is the needle tip.

## 6.2 Experimental Setup

The experimental setup used for ultrasound guidance is shown in Figure 6.2. The main frame is composed of modular T-slotted extrusions (Model 1515 Lite, 80/20 Inc.). Two linear rail systems (Haydon Motion Solutions) are mounted orthogonally to the top frame. The rails consist of a stepper motor (size 17 double stack with 0.015875 mm per step resolution), a wedge style anti-backlash nut, an optical encoder (US Digital E5S, 500 counts per revolution) and 305 mm of total travel. Rail 2 is mounted across the width of rail 1. These two rails are used to position the ultrasound transducer in a plane. The sliding element of the rails that move along the long axis of the rails have axial stability. However, it moves slightly when a loading is applied along its width. To eliminate any horizontal movement that might occur during operation, rail 2 was also constrained using a guide rail that is attached on the frame. When rail 2 slides along the long axis of rail 1, it also slides along the guide rail that provides additional support. The cannula is fixed between two plates. The plates are attached to a vertical support and the vertical support is attached to the sliding element of rail 3. The height of the plates can be adjusted using screws. The vertical position of the ultrasound probe can also be adjusted prior to the experiments to make sure the ultrasound probe is in contact with the tissue sample. The arrows shown with dashed lines show the adjustment direction



for the cannula fixture and the ultrasound fixture. There is a DC motor (Model 247858, Maxon Precision Motors, Inc.) attached to the sliding element of rail 2 and its rotation axis is centered along the center of the ultrasound probe. Hence, the ultrasound probe has two translational and one rotational degrees-of-freedom.

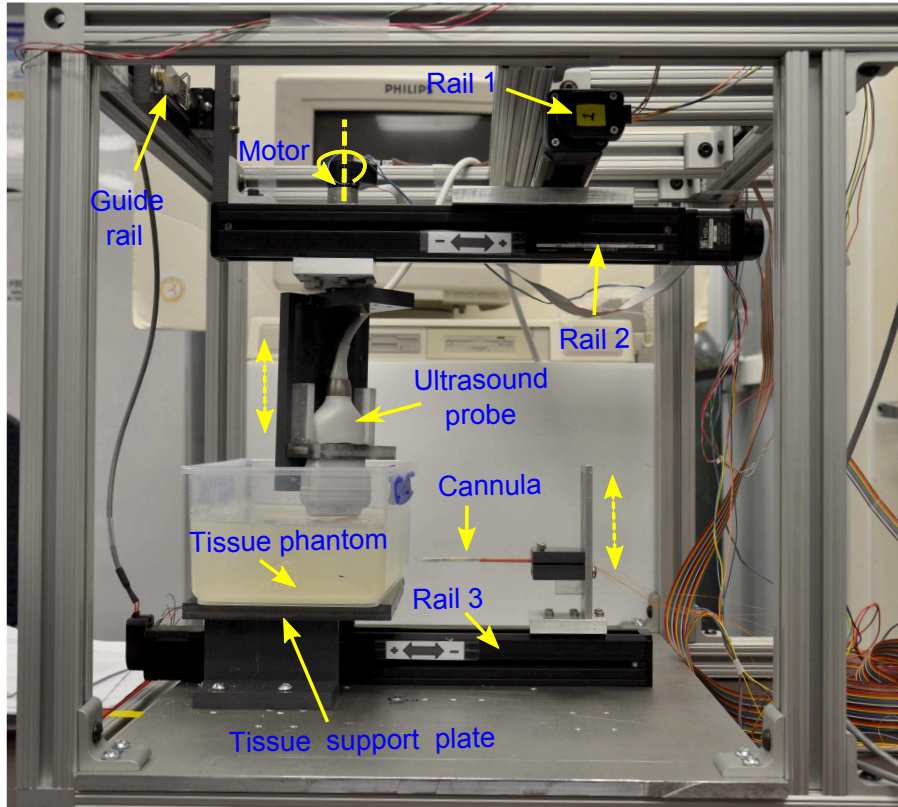


Figure 6.2: Linear rail system used for the ultrasound experiments.

Figure 6.3 depicts the control scheme of the system. There are two PCs that communicate through serial port. One of the PCs control the rails and the cannula using Sensoray 626 DAQ. The DAQ sends control signals to the solid state relays (SSRs) that control the current flow to the respective SMA actuators. The rails are controlled via a TTL-compatible micro stepping chopper drive (DCM 8028, Haydon Motion Solutions). The TTL-signals are generated using Arduino UNO board at

500Hz and this frequency corresponds to 3.9 mm/s travel speed. The DC motor is controlled using a proportional- integral (PI) controller. A constant 2.5V is supplied until the motor angle is within  $10^\circ$  of the desired angle. Once the error is less than  $10^\circ$  the PI controller takes over. Another PC is used to process the ultrasound images. The ultrasound system is a Philips Sonos 5500 ultrasound console with a 3-11 MHz linear array transducer (Model 11-3L). The ultrasound images are acquired in real-time at 15 fps using a Matrox Morphis (Matrox Inc.) frame grabber. Matrox Imaging Library (MIL) library is used to grab and process the images in real-time.

### 6.3 Lucas-Kanade Optical Flow For In-plane Tracking

Optical flow is a fast and robust tracking algorithm that can be used to track features or points in an image stream. Optical flow algorithm has been previously used for temperature estimation in ultrasound images [120], estimation of muscle thickness during contraction [121], and myocardial strain analysis [122] to name a few. While the optical flow algorithm has been applied in other applications, to the best of our knowledge, this is the first time the optical flow algorithm has been applied to ultrasound images to track the features of a needle.

The Lucas-Kanade optical flow algorithm is briefly described here for completeness, and to shed light on the underlying assumptions which make it hard to apply the algorithm to the ultrasound images directly. By comparing two consecutive images in an image stream, an intensity map can be obtained that describes the change in intensity per pixel. Let the increase in brightness in the first image

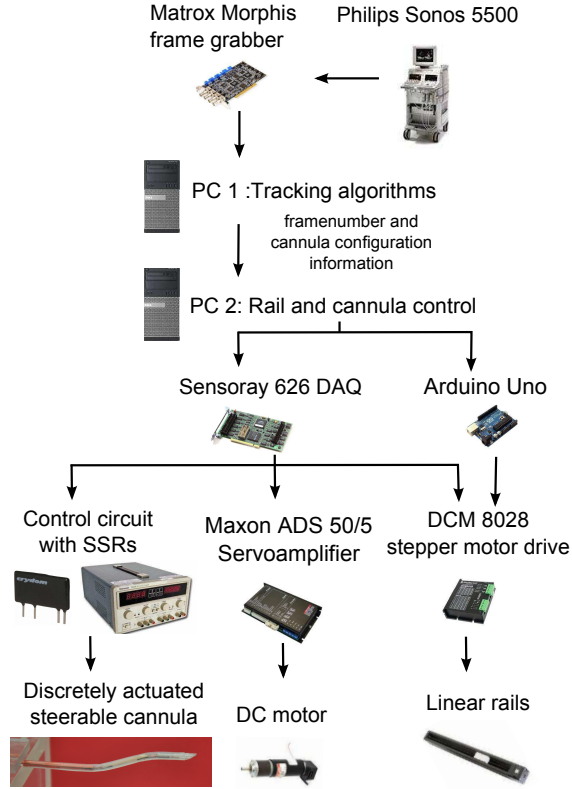


Figure 6.3: Schematic of the control system: The image acquisition rate is fixed at 15 Hz, and hence the hardware control is done with another PC at 60 Hz. The serial port communication takes 15 ms. Therefore, the hardware control is currently limited to 60 Hz.

at a pixel location  $(x, y)$  along the  $x$  direction be  $I_x$  and  $y$  direction be  $I_y$ . After a movement by  $u$  pixels in the  $x$  direction and  $v$  pixels in the  $y$  direction, the total increase in brightness is equal to the local difference in intensity  $I_t$  between the two frames. Hence, the optical flow equation is given as [86]:

$$I_x \cdot u + I_y \cdot v = -I_t \quad (6.1)$$

where  $u$  and  $v$  are the unknown optical flow of the pixel in  $x$  and  $y$  direction, respectively. In the more general form, the optical flow equation for the  $i^{th}$  pixel is

given as:

$$\nabla I(p_i)^T \cdot \begin{bmatrix} u & v \end{bmatrix} + I_t(p_i) = 0 \quad (6.2)$$

The first term is the spatial gradient and the second term is the temporal gradient. Since one pixel does not provide enough information for corresponding to another pixel in the next frame, the equations are formulated in a  $k \times k$  sized window around the pixel assuming they all move by  $[u, v]^T$ . A set of  $k^2$  equations can be obtained and represented in the matrix form as [86]:

$$\begin{bmatrix} I_x(p_1) & I_y(p_1) \\ I_x(p_2) & I_y(p_2) \\ \vdots & \vdots \\ I_x(p_{k^2}) & I_y(p_{k^2}) \end{bmatrix} \begin{bmatrix} u \\ v \end{bmatrix} = \begin{bmatrix} I_t(p_1) \\ I_t(p_2) \\ \vdots \\ I_t(p_{k^2}) \end{bmatrix} \quad (6.3)$$

The system of equations is overdetermined and is of the form:

$$Ad = b \quad (6.4)$$

The solution to Equation 6.4 is formulated as a least-squares minimization of the equation by minimizing  $\|Ad - b\|^2$ . The solution  $d = [u, v]^T$  is found by solving:

$$(A^T A) d = A^T b \quad (6.5)$$

$A^T A$  is indeed the Hessian matrix and has the second-order derivatives of the image intensities. Eigenvalue analysis of the Hessian matrix contain information about local image structure and reveals edges and corners that can be tracked between images [123]. Hence, the detected features are the edges and corners in the  $k \times k$  sized window. Since the algorithm searches only small spatial neighborhood of the pixel

of interest, large motions can cause the points to move outside of the local neighborhood and the tracked points can be lost. To overcome this problem, pyramidal Lucas-Kanade algorithm has been developed which starts analyzing the motion flow from the lowest detail to finer detail [124]. The pyramidal implementation of the Lucas-Kanade method is a fast and reliable optical flow estimator that can accommodate large motions. We use the OpenCV implementation of the algorithm [85]. The mathematical formulation of the optical flow algorithm in pyramids (top to down) is beyond the scope of this work and it is described elsewhere [124].

There are two main assumptions of the Lucas-Kanade optical flow algorithm. Firstly, optical flow algorithm is sensitive to brightness variation and it expects brightness smoothness. The objects or features in the image should exhibit intensity levels that change smoothly. The second assumption is the spatial coherence. It is assumed that neighboring points in a region belong to the same surface and move in a similar fashion. These assumptions make it difficult to apply the optical flow algorithm to ultrasound images directly. In ultrasound images the brightness of a region can change both in time and space. The optical flow algorithm was tested on the ultrasound videos of the cannula. Initially, the desired features to be tracked (corner, edge) are selected by clicking on the image with the mouse. To get the cannula configuration, we track a corner (cannula tip) and an edge (a point on the distal link) on the top surface. The coordinates of the two points are enough to determine the tip location and orientation. Figure 6.4 demonstrates two cases where the algorithm fails to track the desired points in an image stream.

To eliminate these problems, smooth brightness should be achieved on the

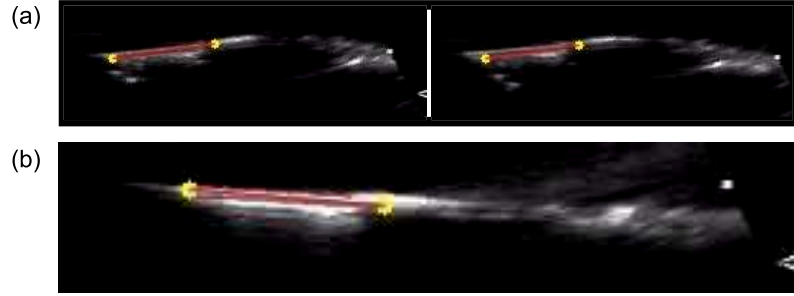


Figure 6.4: The markers are the tracked features (points). A line was plotted to connect the two points to show the orientation of the cannula tip. (a) Two points were selected (shown on left). The point at the tip shifted across the needle cross-section due to pixels having similar brightness as the cannula was further inserted into the tissue phantom (shown on right). This introduces an error in the angle calculation. This means the pixels that are further down the cross-section had similar brightness with the ones that were originally selected on the top surface. (b) This figure shows another example where the algorithm fails in the beginning when a point on the distal link was selected. When a point on the top surface was clicked with the mouse, the algorithm detected a feature (a brighter edge) that is lower down the cross-section.

surface from which the points are selected and the brightness variation of the tracked points in time should be minimized. Edge detection algorithms are useful to find the boundaries of the cannula. However, the boundaries of the cannula are not always clearly resolved since the artifacts result in missing boundaries. Pre-processing of the images is necessary to reduce noise, brightness variation, and missing boundaries. Using a fixed threshold value is risky since in ultrasound images the brightness not only varies in space but also in time as the needle is steered inside the soft tissue

or the organ. Even when the threshold value is varied between images, there might be anatomical structures having same brightness as the needle and thresholding can destroy some portions of the needle as well. Hence, we avoid using thresholding and only morphological operations are used for pre-processing the images.

### 6.3.1 Implementation of In-plane Tracking Algorithm

The image is first pre-processed using downsampling followed by upsampling operation to reduce the amount of noise and detail. Erosion, dilation and blurring operations are also applied recursively to smooth the image and reduce brightness variation. The surface of the cannula facing the transducer has higher brightness in ultrasound images. Sobel operator is applied to the pre-processed image to detect the top surface of the cannula. The edges occur when the gradient is greatest and the Sobel operator finds the edges in the image. The Sobel Operator is a discrete differentiation operator and it computes an approximate image gradient in the  $x$  and  $y$  directions by convolving the image with a pair of  $3 \times 3$  kernels. The kernels of the Sobel operator,  $S_x$  and  $S_y$ , are defined as:

$$S_x = \begin{bmatrix} -1 & 0 & 1 \\ -2 & 0 & 2 \\ -1 & 0 & 1 \end{bmatrix}, S_y = \begin{bmatrix} -1 & -2 & -1 \\ 0 & 0 & 0 \\ 1 & 2 & 1 \end{bmatrix} \quad (6.6)$$

After the top surface of the cannula is detected, a linear blend operator is applied using Equation 6.7 to combine the output of the Sobel operator with the original image.

$$I = \gamma I + (1 - \gamma) I_{sobel} \quad (6.7)$$

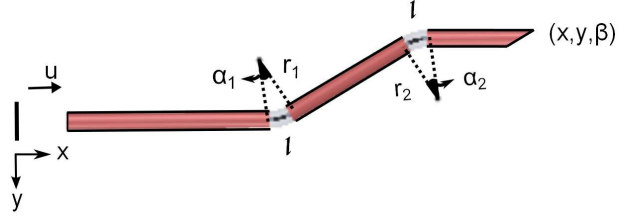


Figure 6.5: Schematic of a 2-DOF planar cannula.

where  $I$  is the original image,  $I_{sobel}$  is the image that is obtained by convolving the pre-processed image with the Sobel operators, and  $\gamma$  is the weight of blending that ranges between 0-1. The blend operator overlays both images, thus enhancing the brightness of the top surface of the cannula on the original image. The resulting image is used as an input to the optical flow algorithm.

The tracking algorithm starts when the cannula is inserted sufficiently into the medium. Once the cannula is inside the imaging region, the tip of the cannula and one point on the top surface of the distal link are selected. A line is fitted between the two points and the tip orientation is obtained. This configuration is registered as the initial configuration. The motion of the two points are continuously tracked using the pyramidal Lucas-Kanade optical flow algorithm. The optical flow algorithm gives the pixel location of the cannula tip position and orientation. The pixel information is then converted into physical dimensions and the joint variables are solved using inverse kinematics. Finally, the shape of the cannula is drawn on the image in real-time using the kinematic equations.

The kinematics of the cannula is straightforward. The schematic used for deriving the forward kinematics of the cannula is shown in Figure 6.5. There are 3



degrees-of-freedom (DOF) : 1-DOF at each joint and 1 insertion DOF. Hence, the joint variables,  $q$ , are  $[u, \alpha_1, \alpha_2]$ . The configuration of the cannula in a plane can be described using Equation 6.8:

$$\begin{aligned} x &= L_1 + u + L_2 \cos \alpha_1 + L_3 \cos \beta + r_1 \sin \alpha_1 + r_2 (\sin \alpha_2 \cos \alpha_1 - \sin \alpha_1 (1 - \cos \alpha_2)) \\ y &= L_2 \sin \alpha_1 + L_3 \sin \beta + r_1 (1 - \cos \alpha_1) + r_2 (\sin \alpha_1 \sin \alpha_2 + \cos \alpha_1 (1 - \cos \alpha_2)) \\ \beta &= \alpha_1 + \alpha_2 \end{aligned} \tag{6.8}$$

where  $\alpha_1$  and  $\alpha_2$  are the joint angles;  $L_1$ ,  $L_2$ , and  $L_3$  are the lengths of the straight segments from the base to the tip;  $(x, y)$  and  $\beta$  describe the position and orientation, respectively. The radius of curvature of the joints is given by  $r_1$  and  $r_2$ . The relation between the arc radius,  $r$ , and joint angle,  $\alpha$ , is  $r = \ell/\alpha$  where  $\ell$  is the length of the SMA actuator between consecutive links. The three equations representing the geometry of the cannula is solved using a 4<sup>th</sup> order Runge-Kutta solver.

## 6.4 Circular Hough Transform for Tip Detection

The Hough transform is commonly used to find the parametrized shapes in an image. It was originally used for the detection of straight lines [125] and has been previously applied for the detection of the needle long-axis in ultrasound images [118, 126]. It was also used to detect curved needles by connecting the straight segments that are found using Hough transform with a polynomial fit [127]. Hough transform can also be used to detect shapes other than lines such as circles and ellipses. Circular Hough transform is a particular example where Hough transform is employed to search a parameter space. A circle with radius  $r$  and its center at

$(a, b)$  is parametrized by the equation:

$$(x - a)^2 + (y - b)^2 = r^2 \quad (6.9)$$

Hough transform usually employs an edge detector to detect the edges of the circle. An arbitrary edge point  $(x_i, y_i)$  transforms into a circular cone in the  $(a, b, r)$  parameter space [125]. Circular Hough transform was previously used for automated localization of retinal optic disk on images captured by a fundus camera [128], measurements of arterial diameter in ultrasound images during the cardiac cycle [129], and segmentation of the left ventricular myocardium in ultrasound images [130]. We use circular Hough transform to detect the needle tip when the tracking is out-of-plane. Since the diameter of the needle is known, the search reduces to two parameters. The algorithm also uses the edge gradient information which determines the direction of the circle with respect to the edge point [131].

## 6.5 Experiments and Results

### 6.5.1 Obtaining Ultrasound Console Specific Parameters

There are two important parameters that need to be determined to assess the accuracy of out-of-plane detection of the needle tip and in-plane detection of the needle shape. The spatial accuracy of out-of-plane detection is limited by the ultrasound beam width whereas the resolution of the ultrasound transducer determines the performance of in-plane tracking. To quantify the ultrasound beam-width, an object with distinct features (Figure 6.6(a)) was scanned by sliding the transducer

over it. Images were obtained at 0.127 mm intervals. Initially, the transducer is away from the object. When the transducer is moved along the direction shown in Figure 6.6(a), the scanned object starts to appear. When the object is aligned with the center of the imaging window, it has maximum visibility. The visibility decreases once the object passes beyond the center of the imaging window. Figure 6.6(b) shows the ultrasound images of the object at various locations. The rectangle block has 2.477 cm length and in the ultrasound images it is visible for 2.794 cm. That means the scanning width of the transducer is 0.317 cm ( $2.794 - 2.477$ ). Even though the physical width of the probe is 1 cm, the effective imaging width is 0.317 cm. If an object with length  $L$  is scanned by sliding the transducer over the object, the object will appear for  $L + 0.317$  cm. If the transducer is used to track the tip of the cannula by placing the ultrasound probe orthogonal to the insertion direction, the tip is visible when the tip of the cannula is inside the 0.317 cm window. This means that the tracking accuracy of the tip is within 0.317 cm when the transducer is used to locate the tip of the cannula. This observation is important yet commonly neglected while assessing the accuracy of tracking the needle tip [113,114].

To determine the image quality and spatial resolution of the transducer, the object was scanned along its width. The dimensions of the cross-section is given in Figure 6.6(c). Figure 6.6(d) shows the dimensions of the object measured using the cursor in the ultrasound console. The maximum error in dimensions was measured as 0.023 cm. Hence, the spatial accuracy of in-plane tracking can be assumed to be limited by this number.

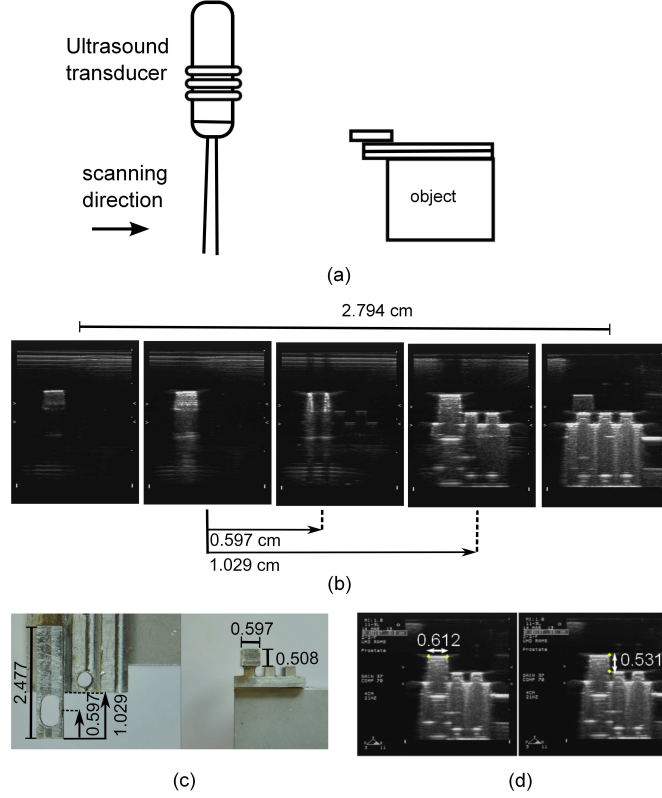


Figure 6.6: Ultrasound beam width and spatial resolution experiments: (a) The schematic of the experimental procedure, (b) the ultrasound images of the object from left to right: the object starts to appear - the object has maximum visibility - after 0.597 cm (center hole)- after 1.029 cm - object starts to disappear, (c) the dimensions of the object, and (d) the dimensions of the object that were measured using the ultrasound console

### 6.5.2 In-plane Tracking of the Cannula

Videos of cannula insertion experiments were recorded to test and optimize the parameters of the tracking algorithm. The transducer was stationary and the cannula was inserted into the gelatin. The cannula was aligned with the ultra-

sound beam in-plane. Full description of the in-plane tracking procedure is given in Algorithm 1. The value of  $\gamma$  was chosen as 0.65.

---

**Algorithm 1** In-plane tracking algorithm

---

```

1:  $I \leftarrow$  grab frame
2: call mouse handler
3: kinematic_initialization  $\leftarrow$  off
4: start_tracking  $\leftarrow$  off
5:  $I_{track,prev} \leftarrow I$   $\triangleright$  Initial image for optical flow
6: repeat
7:    $I \leftarrow$  grab frame
8:   if ROI is selected then
9:     smoothing( $I, 5$ )  $\triangleright$  kernel =  $5 \times 5$ 
10:    for  $k \leftarrow 1, 5$  do
11:      downscale( $I, 0.5$ )  $\triangleright$  to 1/2 of image size
12:      upscale( $I, 1$ )  $\triangleright$  to image size
13:      dilation( $I, 7$ )  $\triangleright$  kernel =  $7 \times 7$ 
14:      erosion( $I, 7$ )  $\triangleright$  kernel =  $7 \times 7$ 
15:      smoothing( $I, 3$ )  $\triangleright$  kernel =  $3 \times 3$ 
16:    end for
17:     $I_{sobel} \leftarrow$  sobel edge detection( $I$ )
18:     $I_{sobel} \leftarrow \lambda I_{sobel}$   $\triangleright$  increase brightness
19:     $I_{track} \leftarrow \text{blend}(\gamma I + (1 - \gamma) I_{sobel})$ 
20:    if 2 points are selected then
21:      kinematic_initialization = on
22:    end if
23:    if kinematic_initialization = on then
24:       $[X, Y] \leftarrow$  get point positions
25:       $(x_0, y_0, \beta_0) \leftarrow (X, Y)$   $\triangleright$  pixel to global
26:       $(u_0, \alpha_{1,0}, \alpha_{2,0}) \leftarrow$ 
inverse_kinematics( $x_0, y_0, \beta_0$ )  $\triangleright$  initial position
27:      kinematic_initialization = off
28:      start_tracking = on
29:    end if
30:    if start_tracking = on then
31:       $[\Delta X, \Delta Y] \leftarrow$  optical_flow( $I_{track}, I_{track,prev}$ )
32:       $(x, y, \beta) \leftarrow (\Delta X, \Delta Y)$   $\triangleright$  update coordinates
33:       $(u, \alpha_1, \alpha_2) \leftarrow$  inverse_kinematics( $x, y, \beta$ )
34:      draw_cannula( $I_{track}, u, \alpha_1, \alpha_2$ )
35:       $I_{track,prev} \leftarrow I_{track}$ 
36:    end if
37:  end if
38: until user stops the process

```

---

Figure 6.7: Pseudocode of the in-plane tracking algorithm

Figure 6.8 shows the original ultrasound image, the pre-processed image and the output of the blend operator which is given as an input to the tracking algorithm. Figure 6.9 shows the results from a tracking experiment in-plane. The cannula trajectory was displayed on the screen and the change of joint variables were recorded in real-time. The cannula kinematics was overlayed on the image

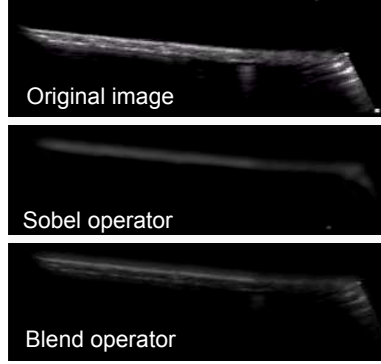


Figure 6.8: The top surface of the cannula was clearly resolved after applying the Sobel operator to the pre-processed images.

with  $\gamma=0.3$  to demonstrate that the cannula shape is accurately detected. Since the blend coefficient  $\gamma$  was chosen as 0.3, the image has a tinge of gray.

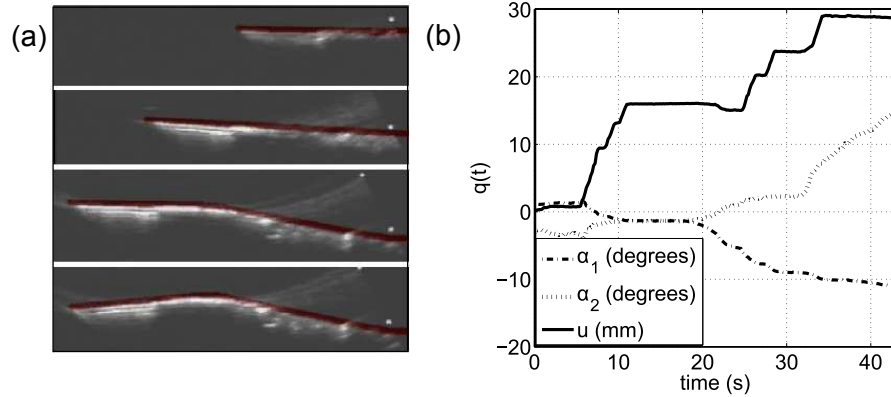


Figure 6.9: Using the optical flow algorithm with brightness enhancement, the cannula can be tracked in real-time: (a) Cannula shape was overlaid on the ultrasound images from the experiment, and (b) the change in joint variables in time

The algorithm was also verified in an *ex-vivo* experiment. Figure 6.10 shows *ex-vivo* bovine kidney images. The cannula is the brightest structure in the image. We can use the in-plane tracking algorithm to track the cannula features. Figure 6.11

shows various steps of the image processing. Figure 6.12 shows the results of a cannula insertion experiment into a bovine kidney. The soft-tissue has more intensity variations compared to the tissue phantom made of gelatin, yet the output of the Sobel edge detector clearly resolves the top surface of the cannula.

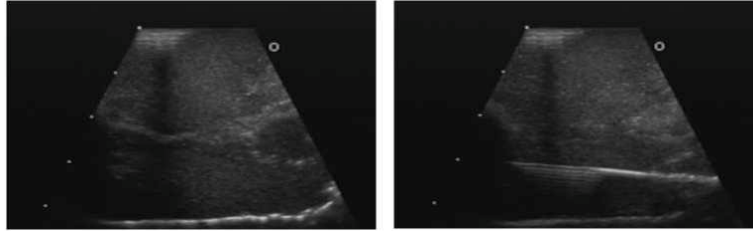


Figure 6.10: *Ex-vivo* bovine kidney image with (right) and without (left) the cannula. Soft-tissue has more intensity variation compared to the tissue phantom made of gelatin, yet the cannula is still the brightest line in the image.

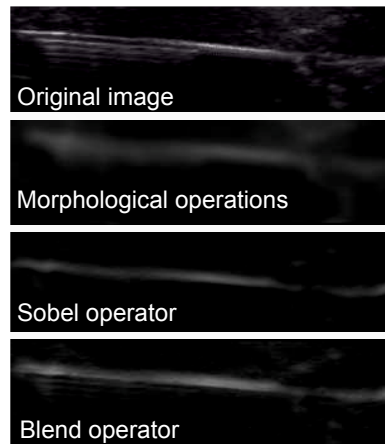


Figure 6.11: Morphological operations remove the amount of noise and detail. Sobel operator detects the top surface of the cannula. The output of the Sobel operator is overlayed on the original image and used as an input to the in-plane tracking algorithm.

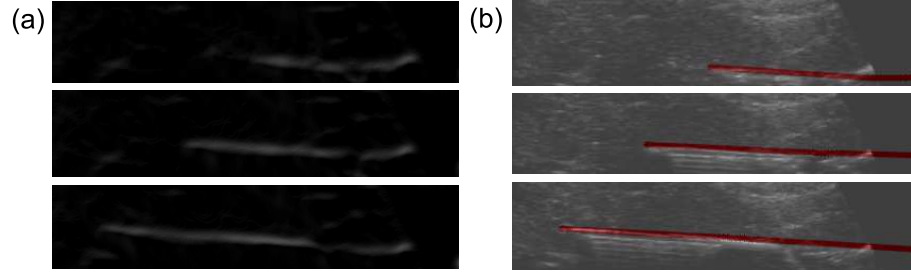


Figure 6.12: *Ex-vivo* bovine kidney experiment: (a) The Sobel operator was applied to the pre-processed images. (b) The shape of the cannula was successfully detected and drawn on the ultrasound images.

The pre-processing step was tested on two commercial needles shown in Figure 6.13(a) inside *ex-vivo* bovine tissue. One of the needles is a 18 gauge needle used for prostate brachytherapy (Mick Radio Nuclear Instruments, Inc.) and the other one is a 12 gauge high field MRI coaxial biopsy needle (Invivo, Corp.). Figure 6.13(b) and 6.13(c) show the original ultrasound images of the prostate brachytherapy and the biopsy needle, and the images after processing.

The intensity map of the original ultrasound images and the processed images for the prostate brachytherapy needle, the coaxial biopsy needle, and the discretely actuated steerable cannula are shown with a color map in Figure 6.14. The brightest pixels are on the top surface of the needles and the processing step extracts the top surfaces of the needles. When the ultrasound images are blended with the processed images, the brightness of the top surface of the needles are enhanced while the brightness of the other regions are reduced.



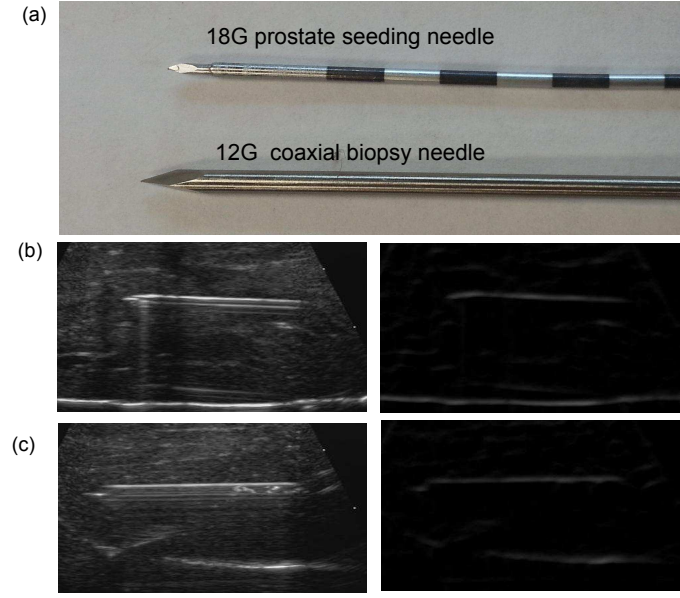


Figure 6.13: (a) Needles that were used in *ex-vivo* bovine experiments, (b) ultrasound image (left) and the processed image (right) of the prostate brachytherapy, and (c) ultrasound image (left) and the processed image (right) of the coaxial biopsy needle.

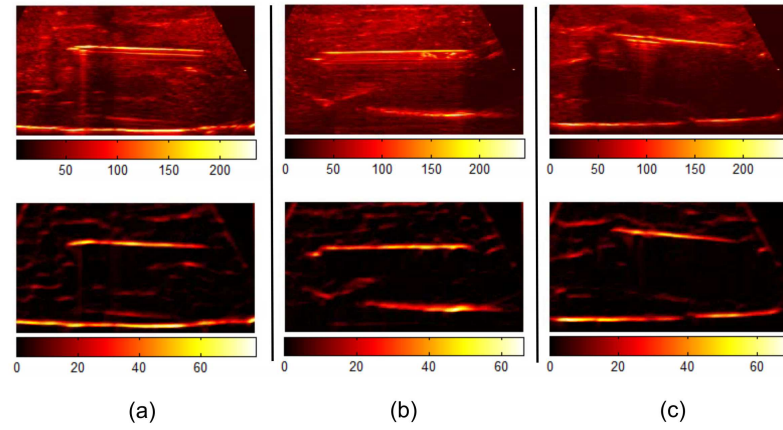


Figure 6.14: Color map of the ultrasound image (top) and the processed image (bottom) for the (a) prostate brachytherapy needle, (b) coaxial biopsy needle, and (c) discretely actuated steerable cannula

### 6.5.3 Out-of-plane Detection of the Cannula Tip

In out-of-plane tracking, the ultrasound transducer is perpendicular to the direction of the needle insertion. Hence, the ultrasound images show cross-sections of the needle-long axis. To demonstrate the tip detection using circular Hough transform, the transducer was positioned away from the cannula tip such that the cannula tip is not visible (Figure 6.15).

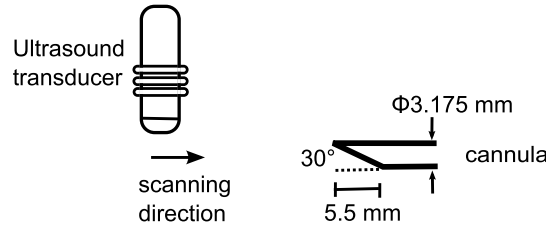


Figure 6.15: To demonstrate tip detection using circular Hough transform, the ultrasound transducer was slid over the cannula and the images were recorded with 0.127 cm intervals.

The transducer was moved towards the cannula tip with 0.127 mm increments. Downscaling, upscaling, dilation, erosion operations followed by blurring were applied recursively to obtain a clear image that is free of any noise. The result is a bright spot at the center of the cannula axis. Figure 6.16 show the original ultrasound images and the images after the pre-processing step. A range of pixel values can be specified to detect circles with a desired diameter. The circle radius was specified as 8-10 pixel which corresponds to 3.074-3.842 mm diameter. The number of recorded frames from the time the tip starts to appear to the frame that the circle is detected is 39. This corresponds to 4.953 mm displacement of the transducer.

The length of the bevel-tip is 5.5 mm and the algorithm shows great performance in accurate detection of the tip. By tip, we imply the end of the bevel where the cross-section forms a circle.

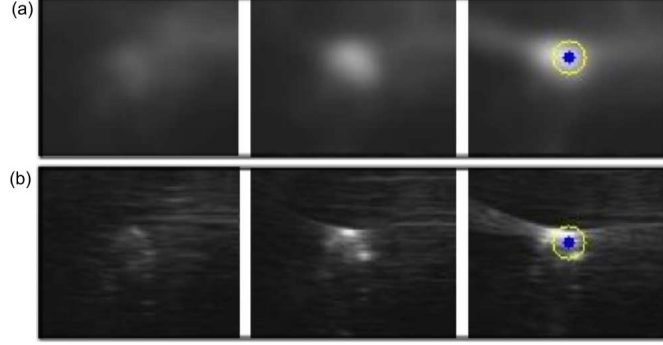


Figure 6.16: The images show (a) the pre-processed images prior to the application of circular Hough transform, and (b) the original ultrasound images. From left-to-right: the cannula starts to appear - a bright region is observed which corresponds to the upper part of the cross-section (bevel-tip)- the cannula cross-section is detected.

In our approach, the main tracking takes place in a plane. The cannula is initially aligned with the ultrasound beam in-plane. In the experimental setup, the relative configuration of the rails and the cannula are known. In a clinical scenario, the registration of the ultrasound probe with the cannula axis can be achieved using a camera system such as Micron Tracker (Claron Technologies Inc.) and the needle plane can be detected by jiggling the needle to differentiate its motion from that of the tissues or organs [132]. The 3D location of the cannula tip can be obtained by rotating the ultrasound transducer by  $90^\circ$  around its axis and sliding the transducer over the cannula to obtain the location of the tip using circular Hough transform. This way any off-plane movement of the cannula due to tissue interaction can be

quantified. Full description of the out-of-plane tip detection procedure is given in Algorithm 2 in Figure 6.17.

---

**Algorithm 2** Out-of-plane tip detection algorithm

---

```

1: repeat
2:    $I \leftarrow$  grab frame
3:   Run: Algorithm 1: In-plane tracking algorithm
4:   if out-of-plane detection is activated then
5:     smoothing( $I, 5$ ) ▷ kernel=  $5 \times 5$ 
6:     for  $k \leftarrow 1, 5$  do
7:       downscale( $I, 0.5$ ) ▷ to 1/2 of image size
8:       upscale ( $I, 1$ ) ▷ to image size
9:       dilation( $I, 7$ ) ▷ kernel=  $7 \times 7$ 
10:      erosion( $I, 7$ ) ▷ kernel=  $7 \times 7$ 
11:      smoothing ( $I, 3$ ) ▷ kernel=  $3 \times 3$ 
12:    end for
13:     $I \leftarrow \lambda I$  ▷ increase brightness
14:     $I \leftarrow$  circular_Hough_transform( $I$ )
15:    if a circle is detected then
16:      draw_circle ( $I$ )
17:      exit
18:    end if
19:  end if
20: until user stops the process

```

---

Figure 6.17: Pseudocode of the out-of-plane tracking algorithm

To demonstrate accurate localization of the cannula tip using combined in-plane and out-of-plane tracking, an experiment was carried out. The frame grabber grabs the image frames at 15 fps. The in-plane tracking algorithm including drawing the cannula configuration and serial port communication with the other PC runs at 8 fps. The out-of-plane tracking algorithm runs at 4 fps. The cannula was inserted at 0.508 cm intervals and was actively tracked in plane by the algorithm that is described in Section 6.3.1. Whenever the cannula tip reached the center of the ultrasound image, ultrasound transducer was also advanced in the direction of cannula insertion by 0.635 cm to guarantee that the cannula tip does not cross

the center of the ultrasound transducer rotation axis. The transducer tracked the cannula tip until 22 seconds. The user requested out-of-plane tip location. The motor rotated  $90^\circ$  and the transducer started moving against the cannula insertion detection and the circular Hough transform was activated. Since the vertical position of the tip in the plane is known prior to the rotation of the transducer, the out-of-plane detection algorithm searches for a circle near the neighborhood of the previous location. When the cannula tip was detected, the program stopped. Figure 6.18 shows the change in cannula insertion distance, the displacement (rail 2) and the rotation of the ultrasound transducer. Figure 6.19 shows the ultrasound images at the locations marked as A, B, C and D in Figure 6.18.

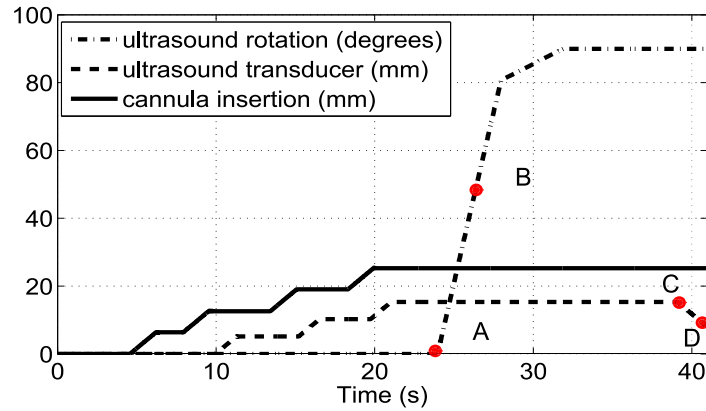


Figure 6.18: Change in ultrasound transducer rotation and position, and the cannula displacement with time

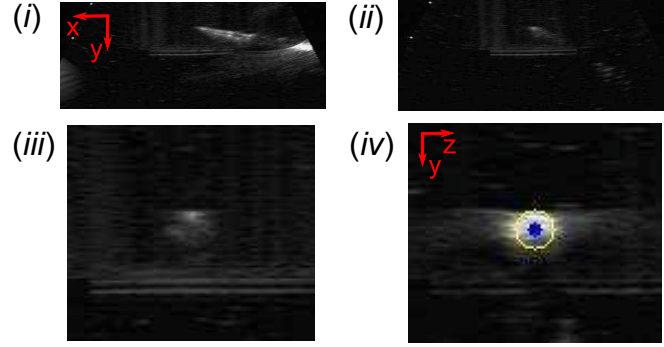


Figure 6.19: Ultrasound images: (a) before the ultrasound transducer rotates (initially the tracking is in-plane), (b) when ultrasound transducer is rotated, (c) 90° rotation is achieved and the cannula tip is observed ahead of the ultrasound transducer, and (d) the transducer moves towards the cannula and the circular cross-section is detected. The location of the tip is  $[x, y, z] = [56.05, 40.30, 58.75]$  mm in the imaging plane.

## 6.6 Summary and Discussions

There are two main results of this section. Firstly, using the pre-processing method described here, the top surface of the needles can be highlighted and smooth brightness can be achieved on the needle top surface. The blend operator not only increases the brightness of the top layer that is detected using the Sobel operator but also reduces the brightness of the other regions since the original image intensities are multiplied by a coefficient that is smaller than 1. The pre-processing step makes it possible to use optical flow algorithm to track the features of the needle in ultrasound images. The effectiveness of the algorithm in extracting the top surface

was successfully demonstrated in tissue phantom and in ex-vivo bovine tissue. The in-plane tracking method can potentially be extended to generic rigid and curved needles. If the needle has a fixed curvature the location of two or more tracked points can be used to calculate the curvature. For needles with an arbitrary shape, multiple points can be selected such that a spline can be fit to the top surface of the needle. Our approach enables tracking the features of the needle. When combined with the geometric model of the needle, the needle configuration can be tracked in real-time.

Secondly, since the cross-section of the needle is a circle, circular Hough transform can be used to localize the needle-tip when the ultrasound beam is perpendicular to the tip of the needle. This algorithm takes advantage of the shape of the bevel tip and does not suffer from finite ultrasound-beam width assumption. The approach presented here guarantees that the detected circle is the needle tip.

Using the methods presented in this chapter, quantitative information about the needle configuration is obtained in real-time, which is crucial for generating control inputs for the needle and automating the needle insertion. The results show the effectiveness of the algorithms and they form the foundations of our future work on combining the in-plane and out-of-plane tracking algorithms for 3D steering of the cannula using ultrasound guidance.

## Chapter 7: CONCLUSIONS AND FUTURE WORK

### 7.1 Conclusions

This work was motivated by the targeting challenges in needle based-procedures. The errors in targeting due to needle and soft tissue interaction forces lead to sampling errors and poor treatment outcomes. A multi degree-of-freedom steerable cannula was developed which can generate steering forces inside the soft-tissue. The cannula has SMA actuators along its length that enable making active trajectory corrections and going around delicate structures. A customized SMA actuator gives some control on the design parameters of the actuator, but it also introduces new challenges. First, annealing the SMA wire changes its phase transformation temperatures. These phase transformation temperatures and the behavior of the actuator under stress at different heat inputs (temperatures) need to be determined to fully characterize the material. Secondly, a new SMA characterization procedure and an experimental setup have to be developed to characterize the SMA actuator. Though characterization and modeling of SMA wires and springs in the straight configuration have been extensively studied, doing similar characterization studies for arbitrarily shaped SMA wires is challenging. Another challenge is to control the strain rate of the SMA actuator in trajectory planning. Since the bending of



each joint is achieved by heating the SMA wire, this process is slow and most of the constitutive models used in modeling the SMA were developed for quasistatic loading. Exploring temperature feedback using the constitutive model has been an important part of the SMA characterization process. We gained information on how the annealing parameters effect the mechanical properties such as the transformation temperatures or the Young's modulus of the SMA actuator (which is a also a measure of the maximum force that can be generated by the actuator). Additionally, for motion planning it is important to investigate the effect of the stiffness of the soft-tissue on the maximum recoverable strain of the SMA (the maximum joint angle). Constitutive model provides a way of incorporating the recoverable strain into the motion planning. In this work, the aforementioned challenges which are crucial for developing an SMA actuated steerable cannula were explored.

Based on the research work done and experimental results obtained in this dissertation, the main conclusions are as follows:

- A new type of hollow needle (cannula) was developed that enables active trajectory corrections and trajectories that are not limited to straight-line trajectories. The cannula can be made of metallic segments or plastic segments. Antagonist SMA actuators can be placed at each joint and bidirectional joint motion can be achieved.
- Temperature feedback is an effective approach to control the strain of the SMA actuator using the constitutive model of the SMA.
- The constitutive model of the SMA effectively represents the phase transfor-

mation of an SMA wire that transforms into an arc. Using the experimental characterization procedure presented in Section 2.4, the parameters of the SMA that are used in the constitutive model can be obtained.

- The PWM-based NPID controller can effectively track continuous temperature trajectories. The controller also limits the strain rate which satisfies the quasistatic assumptions of the constitutive model.
- A motion planning algorithm was developed using tools from differential geometry to find the minimum distance between two set positions for the case when there are no obstacles. The trajectory execution scheme presented in Section 5.1 does not require the control of the the strain rate.
- Using configuration control approach, this redundancy of the cannula can be employed to achieve additional tasks such as obstacle avoidance and joint limit avoidance in addition to reaching a desired location. The joint limit of the SMA actuator was modeled using the constitutive model and it was incorporated into the motion planning algorithm. The configuration control generates trajectories that reach the target while avoiding obstacles and without exceeding the joint limit of the actuator.
- A setup was developed to automate the cannula insertion using ultrasound guidance. In this setup, the ultrasound transducer has 3-DOF and the cannula has 1 insertion DOF. The setup can be used for in-plane tracking, out-of-plane tracking or a combination of both tracking methods.(The main frames were

previously developed by Kevin Lister for *in-vivo* animal experiments [133].)

- The accuracy of the ultrasound tracking algorithms are limited by the spatial resolution of the transducer and ultrasound beam-width. These parameters can be quantified by scanning an object with distinct features as described in Section 6.5.1.
- A brightness enhancement technique was developed that alleviates the intensity variation in ultrasound images. Using the pre-processing method described in Section 6.3, the top surface of the needles can be highlighted and smooth brightness can be achieved which makes it possible to use optical flow to track edges and corners in ultrasound images.
- The cross-section of the cannula is a circle. Thus, circular Hough transform can be used to localize the needle-tip when the ultrasound beam is perpendicular to the tip of the needle. The approach presented in Section 6.5.3 guarantees that the detected circle is the cannula tip.
- Through collaboration with the Biophotonics Group at the Fischell Department of Bioengineering, a side-scanning OCT probe was introduced through the hollow inner core of the cannula and *in-situ* microscale imaging was performed through the imaging window. The results demonstrate the potential use of the cannula as a delivery tool for diagnostic applications.

## 7.2 Future Work

The future directions for research can be listed as follows:

*Cannula design:* The cannula is intended to be a disposable tool. The cannula design can be improved by using segments made of high-temperature plastics that can be quickly manufactured with a 3D printer. This would also make it easier to create slots for temperature sensors, electrical connections and wiring. It would be useful to choose a specific medical application and tailor the design and controllers to achieve a specific task.

*External Stress and Temperature-feedback Controller:* Modeling enhancements that account for heat transfer and the external stress acting on the cannula are necessary. Strain-temperature relationship of the cannula needs be tested under different loadings and initial conditions. To model the external stress acting on the cannula two approaches can be explored. A soft-tissue model can be incorporated into the constitutive model and the deformation strain of the tissue can be mapped into the strain of the SMA actuator. Through experiments the accuracy of the tissue model can be evaluated. Another way is to attach a force sensor at the tip. This force can then be mapped to the stress acting on the SMA actuator using the Jacobian. The wall thickness of the straight tubes are small. Hence, heat transfer becomes a problem when the temperature of the SMA actuator starts increasing. This problem can be alleviated by proper selection of the material as discussed in Section 4.6. Incorporating a cooling strategy would substantially improve the performance of the controller.

*Ultrasound-based Tracking of the Cannula:* In the tracking algorithm, the relative position of the ultrasound transducer and the cannula base were known since the transducer moves in the Cartesian plane. The algorithm starts with the assumption that the cannula is in the imaging plane. In a clinical scenario, registration and positioning of the ultrasound transducer should be achieved such that the ultrasound beam is aligned with the cannula plane.

*Animal Experiments:* The dissertation summarized the tools that were developed for a steerable cannula system. Once the above mentioned advancements are developed, the cannula can be steered using a combined temperature-feedback image-feedback approach with ultrasound guidance. Further *ex-vivo* and *in-vivo* experiments in animal tissues are necessary to assess the performance of the controllers and planners in soft-tissue.

## Bibliography

- [1] American Cancer Society. Cancer facts & figures, 2014.
- [2] Subir Nag, Jay P Ciezki, Robert Cormack, Stephen Doggett, Keith DeWyn-gaert, Gregory K Edmundson, Richard G Stock, Nelson N Stone, Yan Yu, and Michael J Zelefsky. Intraoperative planning and evaluation of permanent prostate brachytherapy: Report of the american brachytherapy society. *International Journal of Radiation Oncology Biology Physics*, 51(5):1422 – 1430, 2001.
- [3] R. Taschereau, J. ouliot, J. Roy, and D. Tremblay. Seed misplacement and stabilizing needles in transperineal permanent prostate implants. *Radiotherapy and Oncology*, 55(1):59 – 63, 2000.
- [4] H. Xu, P. Lasso, A. and Guion, A. Krieger, A. Kaushal, A.K. Singh, P.A. Pinto, J. Coleman, III Grubb, R.L., J. Lattouf, C. Menard, L.L. Whitcomb, and G. Fichtinger. Accuracy analysis in mri-guided robotic prostate biopsy. *International Journal of Computer Assisted Radiology and Surgery*, pages 1–8, 2013.
- [5] H. Sommerkamp, M. Rupprecht, and M. Wannenmacher. Seed loss in interstitial radiotherapy of prostatic carcinoma with i-125. *International Journal of Radiation Oncology Biology Physics*, 14(2):389 – 392, 1988.
- [6] G. S. Merrick, W. M. Butler, A. T. Dorsey, J.H. Lief, and M.L. Benson. Seed fixity in the prostate/periprostatic region following brachytherapy. *International Journal of Radiation Oncology Biology Physics*, 46(1):215 – 220, 2000.
- [7] E.E Deurloo, K.G. Gilhuijs, L.J. Schultze Kool, and S.H. Muller. Displacement of breast tissue and needle deviations during stereotactic procedures. *American Journal of Roentgenology*, 36(6):347–53, 2001.
- [8] Gueninm M.A. Clip placement during sonographically guided large-core breast biopsy for mammographic-sonographic correlation. *American Journal of Roentgenology*, 175(4):1053–1055, 2000.

- [9] L. Margolin, F.R. and Kaufman, S.R. Denny, R.P. Jacobs, and J.D. Schrumpf. Metallic marker placement after stereotactic core biopsy of breast calcifications: Comparison of two clips and deployment techniques. *American Journal of Roentgenology*, 181(6):1685–1690, 2003.
- [10] D.E. Dupuy, R.J. R. J. Zagoria, W. Akerley, W. W. Mayo-Smith, P.V. Kavanagh, and H. Safran. Percutaneous radiofrequency ablation of malignancies in the lung. *American Journal of Roentgenology*, 174(1):57–59, 2000.
- [11] R.J. Bleicher, D.P. Allegra, D.T. Nora, T.F. Wood, L.J. Foshag, and A.J. Bilchik. Radiofrequency ablation in 447 complex unresectable liver tumors: Lessons learned. *Annals of Surgical Oncology*, 10(1):52–58, 2003.
- [12] D.A. Gervais, F.J. McGovern, R.S. Arellano, W.S. McDougal, and P.R. Mueller. Renal cell carcinoma: clinical experience and technical success with radio-frequency ablation of 42 tumors. *Annals of Surgical Oncology*, 226(2):417–24, 2003.
- [13] S.A. Curley. Radiofrequency ablation of malignant liver tumors. *The Oncologist*, 6(1):14–23, 2001.
- [14] C.J. Diederich, W.H. Nau, and P.R. Stauffer. Ultrasound applicators for interstitial thermal coagulation. *IEEE Transactions on Ultrasonics, Ferroelectrics and Frequency Control*, 46(5):1218–1228, 1999.
- [15] E. C. Burdette, F. Banovac, C.J. Diederich, P. Cheng, E. Wilson, and K. R. Cleary. Conformal needle-based ultrasound ablation using em-tracked conebeam ct image guidance. In *SPIE Proceedings: Energy-based Treatment of Tissue and Assessment VI.*, volume 7931, pages 790107–790107–9, 2011.
- [16] E.M. Bector, R.J. 3rd Webster, H Mathieu, A.M. Okamura, and G. Fichtinger. Virtual remote center of motion control for needle placement robot. *The International Journal of Robotics Research*, 9(5):175–83, 2004.
- [17] N. Hata, J. Tokuda, S. Hurwitz, and S. Morikawa. Mri-compatible manipulator with remote-center-of-motion control. *Journal of Magnetic Resonance Imaging*, 27(5):1130–1138, 2008.
- [18] G. Fichtinger, J.P. Fiene, C.W. Kennedy, G. Kronreif, I. Iordachita, D.Y. Song, E. C. Burdette, and P. Kazanzides. Robotic assistance for ultrasound-guided prostate brachytherapy. *Medical Image Analysis*, 12(5):535 – 545, 2008.
- [19] B. Yang, U. Tan, A. McMillan, R. Gullapalli, and J.P. Desai. Towards the development of a master-slave surgical system for breast biopsy under continuous mri. In *13th International Symposium on Experimental Robotics, Quebec City, Canada*, June 2012.

- [20] S.P. DiMaio and S.E. Salcudean. Needle insertion modelling and simulation. In *IEEE International Conference on Robotics and Automation*, volume 2, pages 2098–2105, 2002.
- [21] S.P. DiMaio and S.E. Salcudean. Needle steering and model-based trajectory planning. In *Medical Image Computing and Computer-Assisted Intervention - MICCAI 2003*, volume 2878, pages 33–40, 2003.
- [22] S. Misra, K.B. Reed, K.T. Ramesh, and A.M. Okamura. Observations of needle-tissue interactions. In *MConf Proc IEEE Eng Med Biol Soc.*, pages 262–5, 2009.
- [23] R.J. Roesthuis, Youri R J Van Veen, A. Jahya, and S. Misra. Mechanics of needle-tissue interaction. In *Intelligent Robots and Systems (IROS), 2011 IEEE/RSJ International Conference on*, pages 2557–2563, 2011.
- [24] N Chentanez, R. Alterovitz, D. Ritchie, L. Cho, K. K. Hauser, K. Goldberg, J. R. Shewchuk, and J. F. O’Brien. Interactive simulation of surgical needle insertion and steering. In *In Proceedings of ACM SIGGRAPH 2009*, page 88:110, 2009.
- [25] M Torabi, K. Hauser, R. Alterovitz, D. Vincent, and K. Goldberg. Guiding medical needles using single-point tissue manipulation. In *in Proceedings of the IEEE International Conference on Robotics and Automation*, pages 2705–2710, 2009.
- [26] V.G. Mallapragada, N. Sarkar, and T.K. Podder. Robot assisted real-time tumor manipulation for breast biopsy. In *IEEE International Conference on Robotics and Automation(ICRA)*, pages 2515–2520, 2008.
- [27] W.G. Kuhle. Biopsy needle with flared tip, us5938635 a, Aug 1996.
- [28] A.M. Okamura, C. Simone, and M.D. O’Leary. Force modeling for needle insertion into soft tissue. *IEEE Transactions on Biomedical Engineering*, 51(10):1707–1716, 2004.
- [29] R. J. Webster, N. J. Cowan, G. Chirikjian, and A. M. Okamura. Nonholonomic modeling of needle steering. In *in Proc. 9th International Symposium on Experimental Robotics*, pages 35–44, 2004.
- [30] R.J. Webster, J. Memisevic, and A.M. Okamura. Design considerations for robotic needle steering. In *Proceedings of the 2005 IEEE International Conference on Robotics and Automation*, pages 3588–3594, 2005.
- [31] J.A. Engh, G. Podnar, S. Y. Khoo, and C.N. Riviere. Flexible needle steering system for percutaneous access to deep zones of the brain. In *Proceedings of the IEEE 32nd Annual Northeast Bioengineering Conference*, pages 103–104, 2006.



- [32] A. Ebrahimi, S. Okazawa, R. Rohling, and S. Salcudean. Steerable needle, us20040133168 a1, Jul 2004.
- [33] J. McGuckin. Hollow curved superelastic medical needle and method, us20030032929 a1, Feb 2003.
- [34] W.R. Daum. Deflectable needle assembly, us6572593 b1, June 2003.
- [35] M.D. Heaven and R.C. Klapper. Steerable surgical devices, us5318528 a, June 1994.
- [36] R. J. Webster, A. M. Okamura, and N. J. Cowan. Toward active cannulas: Miniature snake-like surgical robots. In *2006 IEEE/RSJ International Conference on Intelligent Robots and Systems*, pages 2857 – 2863, October 2006.
- [37] P. Sears and P. Dupont. A steerable needle technology using curved concentric tubes. In *2006 IEEE/RSJ International Conference on Intelligent Robots and Systems*, pages 2850 – 2856, October 2006.
- [38] C. Bedell, J. Lock, A. Gosline, and P.E. Dupont. Design optimization of concentric tube robots based on task and anatomical constraints. In *IEEE International Conference on Robotics and Automation*, pages 398–403, 2011.
- [39] H. B. Gilbert, P.J. Swaney, J. Burgner, K.D. Weaver, P. T. Russell, and R. J. Webster. The ACUSITT Ultrasonic Ablator: The First Steerable Needle with an Integrated Interventional Tool. In *Hamlyn Symposium on Medical Robotics*, 2012.
- [40] Andrew H Gosline, Nikolay V Vasilyev, Evan J Butler, Chris Folk, Adam Cohen, Rich Chen, Nora Lang, Pedro J del Nido, and Pierre E Dupont. Percutaneous intracardiac beating-heart surgery using metal mems tissue approximation tools. *The International Journal of Robotics Research*, 31(9):1081–1093, 2012.
- [41] L. B. Kratchman, M. M. Rahman, J. R. Saunders, P. J. Swaney, and R. J. Webster III. Toward robotic needle steering in lung biopsy: A tendon-actuated approach. In *Proceedings of SPIE*, volume 7964, 2011.
- [42] C. Pfeiffer, K. DeLaurentis, and C. Mavroidis. Shape memory alloy actuated robot prostheses: initial experiments. In *1999 IEEE International Conference on Robotics and Automation*, volume 3, pages 2385 – 2391, 1999.
- [43] A. S. Veeramani, G. D. Buckner, S. B. Owen, R. C. Cook, and G. Bolotin. Modeling the dynamic behavior of a shape memory alloy actuated catheter. *Smart Materials and Structures*, 17(1):1 – 14, 2008.
- [44] Y. Haga and M. Esashi. Small diameter active catheter using shape memory alloy coils. *Trans. IEE of Japan*, 120(11):509 – 514, 2000.

- [45] J. Jayender and R. V. Patel. Master-slave control of an active catheter instrumented with shape memory alloy actuators. In *2007 IEEE/RSJ International Conference on Intelligent Robots and Systems*, pages 759 – 764, November 2007.
- [46] E. Ayvali, C.P. Liang, M. Ho, Y. Chen, and J. P. Desai. Towards a discretely actuated steerable cannula for diagnostic and therapeutic procedures. *The International Journal of Robotics Research*, 31(5):588–603, 2012.
- [47] Elif Ayvali and Jaydev P. Desai. Towards a discretely actuated steerable cannula. In *2012 IEEE International Conference on Robotics and Automation (ICRA)*, pages 1614 – 1619, May 2012.
- [48] L.C. Chang and T.A. Read. *Transactions of the American Institute of Mechanical Engineers*, 191:57, 1951.
- [49] W.J. Buehler, J.V. Gilfrich, and R.C. Wiley. Effect of low-temperature phase changes on the mechanical properties of alloys near composition NiTi. *Journal of Applied Physics*, 34(5):1475–1477, 1963.
- [50] E. Pieczyska, S. Gadaj, W.K. Nowacki, K. Hoshio, Y. Makino, and H. Tobushi. Characteristics of energy storage and dissipation in tini shape memory alloy. *Science and Technology of Advanced Materials*, 6(8):889–894, 2005.
- [51] J.A. Shaw, C.B. Churchill, and M.A. Iadicola. Tips and tricks for characterizing shape memory alloy wire: Part 1 differential scanning calorimetry and basic phenomena. *Experimental Techniques*, 32(5):55–62, 2008.
- [52] M. Ryosuke, M. Yoshiyasu, T. Hisaaki, F. Yuji, and Y. Fusahito. Influence of strain ratio on bending fatigue life and fatigue crack growth in tini shape-memory alloy thin wires. *Mater Trans*, 47:759765, 2006.
- [53] K. Tanaka. A thermomechanical sketch of shape memory effect: Onedimensional tensile behavior. *Res. Mechanica*, 18:251–263, 1986.
- [54] C. Liang and C. A. Rogers. One-dimensional thermo mechanical constitutive relations for shape memory material. *Journal of Intelligent Materials and Structures*, 1(2):207–234, 1990.
- [55] L. C. Brinson. One-dimensional constitutive behavior of shape memory alloys: Thermomechanical derivation with non-constant material functions and redefined martensite internal variable. *Journal of Intelligent Materials and Structures*, 4:229–242, 1993.
- [56] C. B. Churchill, J. A. Shaw, and M. A. Iadicola. Tips and tricks for characterizing shape memory alloy wire: part 2-fundamental isothermal response. *Experimental Techniques*, 33(1):51 – 62, 2009.

- [57] Dimitris C Lagoudas. *Shape Memory Alloys Modeling and Engineering Applications*. Springer, 2008.
- [58] T. Hisaaki and T. Kikuaki. Deformation of a shape memory alloy helical spring : Analysis based on stress-strain-temperature relation. *JSME international journal. Ser. 1, Solid mechanics, strength of materials*, 34(1):83 – 89, 1991.
- [59] Mingyen Ho and Jaydev P. Desai. Characterization of sma actuator for applications in robotic neurosurgery. In *Proceedings of the IEEE Engineering in Medicine and Biology Society (EMBC) Annual International Conference*, pages 6856–6859, 2009.
- [60] Ichiro Sakuma, Yosuke Nishimura, CheeKong Chui, Etsuko Kobayashi, Hiroshi Inada, Xian Chen, and Toshiaki Hisada. In vitro measurement of mechanical properties of liver tissue under compression and elongation using a new test piece holding method with surgical glue. In *Surgery Simulation and Soft Tissue Modeling*, volume 2673, pages 284–292. Springer Berlin Heidelberg, 2003.
- [61] J. Jayender, R.V.Patel, S. Nikumb, and M. Ostojic. Modeling and control of shape memory alloy actuators. *IEEE Transactions on Control Systems Technology*, 16(2):279 – 287, 2008.
- [62] Y. H. Teh and R. Featherstone. An architecture for fast and accurate control of shape memory alloy actuators. *The International Journal of Robotics Research*, 27(5):595–611, 2008.
- [63] Shu-Hung Liu, Tse-Shih Huang, and Jia-Yush Yen. Tracking control of shape-memory-alloy actuators based on self-sensing feedback and inverse hysteresis compensation. *Sensors*, 10(1):112–127, 2009.
- [64] G. Song, V. Chaudhry, and C. Batur. A neural network inverse model for a shape memory alloy wire actuator. *Journal of Intelligent Material Systems and Structures*, 14(6):371–377, 2003.
- [65] M. Sreekumar, M. Singaperumal, T. Nagarajan, M. Zoppi, and R. Molino. Recent advances in nonlinear control technologies for shape memory alloy actuators. *Journal of Zhejiang University - Science A*, 8, 2007.
- [66] M.H. Elahinia, E.T. Esfahani, and S. Wang. Control of sma systems: review of the state of the art. *Shape Memory Alloys: Manufacture, Properties and Applications*, pages 381–392, 2011.
- [67] C. A. Dickinson and J. T. Wen. Feedback control using shape memory alloy actuators. *Journal of Intelligent Material Systems and Structures*, 9(4):242 – 250, 1998.

- [68] N. Ma, G. Song., and H-J Lee. Position control of shape memory alloy actuators with internal electrical resistance feedback using neural networks. *Smart Materials and Structures*, 13(4):777–783, 2004.
- [69] S.M. Dutta and F.H. Ghorbel. Differential hysteresis modeling of a shape memory alloy wire actuator. *IEEE/ASME Transactions on Mechatronics*, 10(2):189 –197, 2005.
- [70] K. Ikuta, M. Tsukamoto, and S. Hirose. Shape memory alloy servo actuator system with electric resistance feedback and application for active endoscope. In *1988 IEEE International Conference on Robotics and Automation*, volume 1, pages 427 –43, April 1988.
- [71] N. Ma and G. Song. Control of shape memory alloy actuator using pulse width modulation. *Smart Materials and Structures*, 12:712–719, 2003.
- [72] A. D. Price, A. Jnifene, and H. E. Naguib. Design and control of a shape memory alloy based dexterous robot hand. *Smart Materials and Structures*, 16:1401 – 1414, 2007.
- [73] Mingyen Ho and J.P. Desai. Towards a MRI compatible meso-scale SMA actuated robot using PWM control. In *2010 3rd IEEE RAS and EMBS International Conference on Biomedical Robotics and Biomechatronics (BioRob)*, pages 361 – 366, September 2010.
- [74] E. Shameli, A. Alasty, and H. Salaarieh. Stability analysis and nonlinear control of a miniature shape memory alloy actuator for precise applications. *Mechatronics*, 15(4):471 – 486, 2005.
- [75] S.M.M. Rahman, K. K. Ahn, and H.P. H.Anh. A comparative study of position control of a sma actuated manipulator. In *Second International Conference on Communications and Electronics(ICCE 2008)*, pages 29 – 32, June 2008.
- [76] J J Amalraj, A Bhattacharyya, J J Amalraj, and M G Faulkner. Finite-element modeling of phase transformation in shape memory alloy wires with variable material properties. *Smart Materials and Structures*, 9(5):622, 2000.
- [77] R. Velazquez and E. Pissaloux. A comparison of controllers for improving the time response of niti wires. In *AFRICON, 2009. AFRICON '09.*, pages 1 – 6, September 2009.
- [78] A.Pathak, D.Brei, and J. Luntz. Transformation strain based method for characterization of convective heat transfer from shape memory alloy wires. *Smart Materials and Structures*, 19(3):035005, 2010.
- [79] H. Prahlad and I.Chopra. Development of a strain-rate dependent model for uniaxial loading of sma wires. *Journal of Intelligent Material Systems and Structures*, 14(7):429–442, 2003.

- [80] A Bhattacharyya, L Sweeney, and M G Faulkner. Experimental characterization of free convection during thermal phase transformations in shape memory alloy wires. *Smart Materials and Structures*, 11(3):411, 2002.
- [81] P Senthilkumar, G N Dayananda, M Umapathy, and V Shankar. Experimental evaluation of a shape memory alloy wire actuator with a modulated adaptive controller for position control. *Smart Materials and Structures*, 21(1):015015, 2012.
- [82] D. Grant and V. Hayward. Variable structure control of shape memory alloy actuators. *Control Systems, IEEE*, 17(3):80 – 88, June 1997.
- [83] M.H. Elahinia. Nonlinear Control of a Shape Memory Alloy Actuated Manipulator. Master’s thesis, Villanova University, USA, 2001.
- [84] B.D. Lucas and T. Kanade. An iterative image registration technique with an application to stereo vision. In *Proceedings of the international joint conference on Artificial intelligence*,, pages 674–679, 1981.
- [85] G. Bradski. The opencv library. *Dr. Dobb’s Journal of Software Tools*, 2000.
- [86] G. Bradski and A. Kaehler. *Learning OpenCV: Computer Vision with the OpenCV Library*. O’Reilly Media, 2008.
- [87] J. Fujimoto and W. Drexler. *Optical Coherence Tomography*. Springer, 2008.
- [88] P.L. Hsiung, D. R. Phatak, Y. Chen, A. D. Aguirre, J. G. Fujimoto, and J. L. Connolly. Benign and malignant lesions in the human breast depicted with ultrahigh resolution and three dimensional optical coherence tomography. *Radiology*, 244(3):865–874, 2007.
- [89] F. T. Nguyen, A. M. Zysk, E. J. Chaney, J. G. Kotynek, U. J. Oliphant, F. J. Bellafiore, K. M. Rowland, P. A. Johnson, and S. A. Boppart. Intraoperative evaluation of breast tumor margins with optical coherence tomography. *Cancer Research*, 69(22):87908796, 2009.
- [90] A.M. Zysk and S.A. Boppart. Computational methods for analysis of human breast tumor tissue in optical coherence tomography images. *J. Biomed. Opt.*, 11(5):054015–1054015–7, 2006.
- [91] M. Mujat, R. D., D. X. Hammer, C. Gittins, and N. Iftimia. Automated algorithm for breast tissue differentiation in optical coherence tomography. *J. Biomed. Opt.*, 14(3):034040–1034040–9, 2009.
- [92] V. Duindam, R. Alterovitz, S. Sastry, and K. Goldberg. Screw-based motion planning for bevel-tip flexible needles in 3D environments with obstacles. In *2008 IEEE International Conference on Robotics and Automation*, pages 2483–2488, May 2008.

- [93] W. Park, J. S. Kim, Y. Zhou, N. J. Cowan, A. M. Okamura, and G.S. Chirikjian. Diffusion-based motion planning for a nonholonomic flexible needle model. In *Proceedings of the 2005 IEEE International Conference on Robotics and Automation*, pages 4600–4605, April 2005.
- [94] D. Glozman and M. Shoham. Image-guided robotic flexible needle steering. *IEEE Trans. Robot.*, 23(3):459–467, 2007.
- [95] J. Xu, V. Duindam, R. Alterovitz, and K. Goldberg. Motion planning for steerable needles in 3D environments with obstacles using rapidly-exploring random trees and backchaining. In *2008 IEEE International Conference on Automation Science and Engineering*, pages 41–46, August 2008.
- [96] R. Alterovitz, K. Goldberg, and A. M. Okamura. Planning for steerable bevel-tip needle insertion through 2d soft tissue with obstacles. In *Proceedings of the 2005 IEEE International Conference on Robotics and Automation*, pages 1640–1645, April 2005.
- [97] L. A. Lyons, R. J. Webster, and R. Alterovitz. Planning active cannula configurations through tubular anatomy. In *2010 IEEE International Conference on Robotics and Automation*, pages 2082–2087, May 2010.
- [98] R. M. Murray, Z. Li, and S. S. Sastry. *A Mathematical Introduction to Robotic Manipulation*. CRC Press, 1994.
- [99] M. P. Do Carmo. *Riemannian geometry, Mathematics: Theory & Applications*. Birkhauser Boston, Inc., 1992.
- [100] O. Brock, O. Khatib, and S. Viji. Task-consistent obstacle avoidance and motion behavior for mobile manipulation. In *IEEE International Conference on Robotics and Automation (ICRA)*, volume 1, pages 388 – 393, 2002.
- [101] D.N. Nenchev, Y. Tsumaki, and M. Takahashi. Singularity-consistent kinematic redundancy resolution for the s-r-s manipulator. In *2004 IEEE/RSJ International Conference on Intelligent Robots and Systems (IROS )*, volume 4, pages 3607 – 3612 vol.4, sept.-2 oct. 2004.
- [102] I Iossifidis and G. Schoner. Dynamical systems approach for the autonomous avoidance of obstacles and joint-limits for an redundant robot arm. In *Intelligent Robots and Systems, 2006 IEEE/RSJ International Conference on*, pages 580 –585, oct. 2006.
- [103] Kwang-Kyu Lee and M. Buss. Obstacle avoidance for redundant robots using jacobian transpose method. In *IEEE/RSJ International Conference on Intelligent Robots and Systems (IROS)*, pages 3509 –3514, 29 2007-nov. 2 2007.
- [104] H. Seraji and R. Colbaugh. Improved configuration control for redundant robots. *Journal of Robotic Systems*, 7(6):897–928, 1990.



- [105] H. Seraji and R. Colbaugh. Singularity-robustness and task-prioritization in configuration control of redundant robots. In *Proceedings of the 29th IEEE Conference on Decision and Control, 1990.*, volume 6, pages 3089–3095, dec 1990.
- [106] Farbod Fahimi. *Autonomous Robots Modeling, Path Planning, and Control*. Springer, 2009.
- [107] R. Colbaugh, H. Seraji, and K. L. Glass. Obstacle avoidance for redundant robots using configuration control. *Journal of Robotic Systems*, 6(6):721–744, 1989.
- [108] C.L.L. Hendriks, M. van Ginkel, P.W. Verbeek, and L. J. van Vliet. The generalized radon transform: Sampling, accuracy and memory considerations. *Pattern Recognition*, 38(12):2494 – 2505, 2005.
- [109] H.R.S. Neshat and R.V. Patel. Real-time parametric curved needle segmentation in 3D ultrasound images. In *2nd IEEE RAS EMBS International Conference on Biomedical Robotics and Biomechatronics (BIOROB)*, pages 670–675, 2008.
- [110] Stanley R. Deans. Hough transform from the radon transform. *Pattern Analysis and Machine Intelligence, IEEE Transactions on*, PAMI-3(2):185–188, 1981.
- [111] J. Hong, T. Dohi, M. Hashizume, K. Konishi, and N. Hata. An ultrasound-driven needle-insertion robot for percutaneous cholecystostomy. *Physics in Medicine AND Biology*, 49(3):441, 2000.
- [112] P.M. Novotny, J. A. Stoll, N. V. Vasilyev, P. J. del Nido, P. E. Dupont, T. E. Zickler, and R. D. Howe. GPU based real-time instrument tracking with three-dimensional ultrasound. *Medical Image Analysis*, 11(5):458 – 464, 2007.
- [113] Z. Neubach and M. Shoham. Ultrasound-guided robot for flexible needle steering. *IEEE Transactions on Biomedical Engineering*, 57(4):799–805, 2010.
- [114] G.J. Vrooijink, M. Abayazid, and S. Misra. Real-time three-dimensional flexible needle tracking using two-dimensional ultrasound. In *Proceedings of the IEEE International Conference on Robotics and Automation (ICRA)*, pages 1676–1681, 2013.
- [115] T. K. Adebar and A.M. Okamura. 3D segmentation of curved needles using doppler ultrasound and vibration. In *Information Processing in Computer-Assisted Interventions*, volume 7915 of *Lecture Notes in Computer Science*, pages 61–70. 2013.
- [116] R. Hongliang and P.E. Dupont. Tubular enhanced geodesic active contours for continuum robot detection using 3D ultrasound. In *IEEE International Conference on Robotics and Automation (ICRA)*, pages 2907–2912, May 2012.

- [117] P. Chatelain, A. Krupa, and M. Marchal. Real-time needle detection and tracking using a visually servoed 3D ultrasound probe. In *IEEE International Conference on Robotics and Automation (ICRA)*, pages 1676–1681, May 2013.
- [118] Jae Sung Hong, Takeyoshi Dohi, Makoto Hasizume, Kozo Konishi, and Nobuhiko Hata. A motion adaptable needle placement instrument based on tumor specific ultrasonic image segmentation. In *Medical Image Computing and Computer-Assisted Intervention MICCAI 2002*, volume 2488 of *Lecture Notes in Computer Science*, pages 122–129. Springer Berlin Heidelberg, 2002.
- [119] R. H. Gottlieb, W. B. Robinette, D. J. Rubens, D. F. Hartley, P. J. Fultz, and M. R. Violante. Coating agent permits improved visualization of biopsy needles during sonography. *American Journal of Roentgenology*, 171(6):1301–1302, 1998.
- [120] B.M. Mehrabani, V. Tavakoli, M.D. Abolhassani, J. Alirezaie, and A. Ahmadian. An efficient temperature estimation using optical-flow in ultrasound b-mode digital images. In *30th Annual International Conference of the IEEE Engineering in Medicine and Biology Society (EMBS 2008)*, pages 86–89, Aug 2008.
- [121] L. Qiaoliang, N. Dong, Y. Wanguan, C. Siping, W. Tianfu, and C. Xin. Use of optical flow to estimate continuous changes in muscle thickness from ultrasound image sequences. *Ultrasound in Medicine and Biology*, 39(11):2194 – 2201, 2013.
- [122] Q. Duan, K. M. Parker, A. Lorsakul, E. D. Angelini, E. Hyodo, J. W. Homma, S. and Holmes, and A. F. Laine. Quantitative validation of optical flow based myocardial strain measures using sonomicrometry. *Proc IEEE Int Symp Biomed Imaging*, 2009:454–457, Jun 2009.
- [123] J. Shi and C. Tomasi. Good features to track. In *1994 IEEE Computer Society Conference on Computer Vision and Pattern Recognition*, pages 593–600, 1994.
- [124] Jean Yves Bouguet. Pyramidal implementation of the lucas kanade feature tracker. *Intel Corporation, Microprocessor Research Labs*, 2000.
- [125] Richard O. Duda and Peter E. Hart. Use of the hough transformation to detect lines and curves in pictures. *Communications of the ACM*, 15(1):11–15, 1972.
- [126] Mingyue Ding and Aaron Fenster. A real-time biopsy needle segmentation technique using hough transform. *Medical Physics*, 30(8):2222–2233, 2003.
- [127] M. Aboofazeli, P. Abolmaesumi, P. Mousavi, and G. Fichtinger. A new scheme for curved needle segmentation in three-dimensional ultrasound images. In *IEEE International Symposium on Biomedical Imaging: From Nano to Macro (ISBI)*, pages 1067–1070, 2009.



- [128] S. Sekhar, W. Al-Nuaimy, and A.K. Nandi. Automated localisation of retinal optic disk using hough transform. In *5th IEEE International Symposium on Biomedical Imaging: From Nano to Macro (ISBI 2008)*, pages 1577–1580, May 2008.
- [129] S. Golemati, J. Stoitsis, T. Balkizas, and K.S. Nikita. Comparison of b-mode, m-mode and hough transform methods for measurement of arterial diastolic and systolic diameters. In *27th Annual International Conference of the Engineering in Medicine and Biology Society (EMBS 2005)*, pages 1758–1761, Jan 2005.
- [130] J.E. McManigle, R.V. Stebbing, and J.A. Noble. Modified hough transform for left ventricle myocardium segmentation in 3-d echocardiogram images. In *9th IEEE International Symposium on Biomedical Imaging (ISBI 2012)*, pages 290–293, May 2012.
- [131] X. Chen, L. Lu, and Y. Gao. A new concentric circle detection method based on hough transform. In *International Conference on Computer Science Education (ICCSE)*, pages 753–758, 2012.
- [132] Bin Dong, Eric Savitsky, and Stanley Osher. A novel method for enhanced needle localization using ultrasound-guidance. In *Advances in Visual Computing*, volume 5875 of *Lecture Notes in Computer Science*, pages 914–923. Springer Berlin Heidelberg, 2009.
- [133] K. Lister, Z. Gao, and J.P. Desai. Development of in vivo constitutive models for liver: Application to surgical simulation. *Annals of Biomedical Engineering*, 39(3):1060–1073, 2011.